The energy balance of HID lamps

Janssen, J.F.J.

Award date:
2012

Eindhoven University of Technology
Department of Applied Physics
Elementary Processes in Gas Discharges

The energy balance of HID lamps

J.F.J. Janssen

April 11, 2012

Supervisors: ir. A.J. Rijke
prof.dr.ir. M.Haverlag
dr. ir. S. Nijdam
prof.dr.ir. G.M.W. Kroesen

Abstract

HID lamps are efficient lamps that produce light from a compact source. In this work the energy balance of HID lamps is studied both experimentally and theoretically. For the experiments an integrating sphere setup was used. The experimentally determined energy balance and spectra are compared with predictions of a simulation model. The four investigated lamps all contain mercury. Three lamps also contain one metal halide additive. The additives are sodium, indium and thallium iodide.

The integrating sphere setup has been calibrated for measurements ranging from 380 nm to 10 μm. Such a large calibrated range enables the construction of an almost complete energy balance. Being able to measure and analyze broadband spectra will help to improve lamps. The accuracy of the calibration of the visible and infrared is estimated to be 5 %.

A platinum ribbon was used as a calibration source for the infrared. The spectral power was calculated theoretically. The infrared measurements require a correction for thermal background radiation. Therefore temperature regulation systems were installed. A distinguishment between thermal radiation of the discharge vessel and plasma radiation has been made. The energy flow inside the discharge vessel was further investigated by applying Jack Koedam theory to estimate the conduction losses and the amount of radiation which is absorbed in the outer mantle of the plasma.

A one dimensional model for an infinitely long lamp was made which is capable of providing a good qualitative description of the energy balance and the spectra. For the model calculations LTE is assumed. The energy transported as radiation is calculated by a method called raytracing. In this method the evolution of the spectral radiance is followed along multiple paths through the discharge. The most important input parameters for the model are the broadening constants. These constants were determined by fitting the predicted spectrum with a measured spectrum from a reference lamp. Using these broadening constants quantitative predictions were made of the amount of visible radiation for the 250 W mercury calibration lamp operated at a wide range of input powers.

Contents

Chapter 1

General introduction

HID lamps are efficient light sources that are used in various indoor and outdoor applications. These lamps produce light from a compact source. This makes them ideal for example in street lighting, automotive lighting, retail lighting and lighting in projection systems. This research will focus on metal halide lamps which are part of the HID lamp family.

1.1 High intensity discharge lamps

By applying a potential a gas can break down electrically and reach a conductive state. When this happens a so-called discharge arc is formed. In such an arc electrons are accelerated by the potential. Collisions with the gas transfer energy from the electrons to the gas. The electrons orbiting a nucleus can be excited by collisions. Radiation is produced when these excited electrons decay to a state with a lower energy. Lamps that produce radiation via this mechanism are called discharge lamps.

The first discharge lamp was a carbon arc lamp built in 1850 [1] by Léon Foucault. Although this lamp emitted light from the discharge arc most of the light still originated from the hot anode as thermal radiation. In 1860 mercury was added to the discharge by J.T. Way [1]. By adding mercury the discharge became the primary source of radiation. Mercury was added to the discharge for its high vapor pressure at room temperature and the ability to make a substantial contribution to visible radiation. Around 1900 the first low pressure mercury lamps were built. At that time all lamps were incandescent lamps. Those lamps are resistively heated lamps that emit thermal radiation. Mercury lamps were superior to the incandescent lamps in terms of efficiency since incandescent lamps mostly emit in the infrared. Despite their higher efficiency these mercury lamps were no success due to their bad color rendering. In 1906 Guercke [1] already noticed that color rendering could be improved by adding some metals to the mercury discharge which can emit visible radiation. One of the problems of those lamps was the very short lifetime. The quartz glass was not resistant to the metal. Getting these solid metals into the discharge was another problem.

Improvements in other areas shifted the focus of research [1]: The discovery of sodium resistant glass in 1920 eventually resulted in the development of low and high pressure sodium lamps and the usage of fluorescent materials improved the color rendering and efficiency of mercury lamps. Decades later the interest in metal additives was given a boost when research turned to metal-halogen compounds. These compounds have a higher vapour pressure in comparison with the pure metals. In the centre of the discharge these compounds dissociate into their atomic constituents making the metal atoms available for excitation by electron collisions. The ability to form molecular compounds in the lower temperature region near the discharge wall also decreased the demands for the wall material since corrosion by the pure metals was reduced. In 1961 the first metal-halide lamp was patented [1]. Ever since, metal halide lamps have been used in various applications. Domestic applications however were no success in the early years. The main reasons

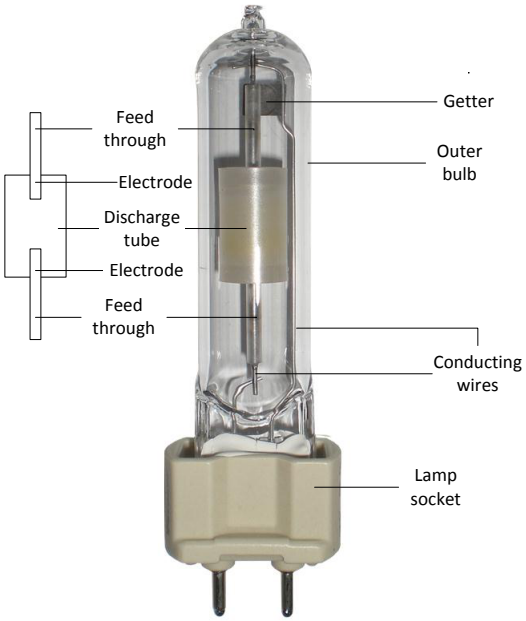

Figure 1.2.1: *The CDM lamp has a cylindrical discharge tube which contains all of the metal-halide additives and the buffer gas. This tube is mounted inside the outer bulb with a conducting metallic framework. The outer bulb contains a low pressure environment. A getter is present in the outer bulb to neutralize all contaminations that may be harmfull for the discharge tube.*

were the high costs and the lack of the ability to turn the lamp on again shortly after being turned off.

In the 80's and 90's research focussed on ceramic discharge tubes. In 1995 Philips launched its CDM (ceramic discharge metal-halide) lamp series. This series covers a wide range of lighting needs by using possible additives like sodium, thallium, dysprosium, holmium, thulium, calcium, cerium and indium halides. Other companies like General electric and Osram now also produce ceramic metal halide lamps. These lamps still contain mercury. The growing interest in sustainable engineering currently motivates the lighting industry to invest in research for mercury free metal halide lamps.

1.2 Metal halide lamp

In Figure 1.2.1 an image of a CDM lamp is shown. A few components have been named.

- The discharge tube contains the metal halide additives which are responsible for the production of light. The tube is made from PCA (polycrystalline aluminum) to be able to withstand the high temperatures.

- The electrode is generally made from tungsten. The feedthrough contains niobium and molybdenum. The coefficient of thermal expansion must match with the expansion coefficient of PCA. The potential between the electrodes is dependent on the gas pressure. The gasses that have a large contribution to the resistance of the plasma are called buffer gasses.

- The discharge tube is contained within the outer bulb in a low pressure atmosphere. These conditions are necessary to avoid corrosion of PCA. Some oxygen is still present within the bulb. The getter is a highly reactive material which neutralises the remaining oxygen.

1.3 Start up phase

In the lamp's initial condition mercury and the metal-halide additives are present on the wall in their liquid and solid forms. The gas phase in the discharge tube consists of a starter gas. Generally these are one or more noble gases like Xenon or Argon. Sometimes a small amount of a radioactive species is added to increase the number of free electrons in the gas. Antennas can also help ignite the lamp [10]. The lamp is operated by an electronic device called a driver. The driver attempts to ignite the lamp by applying high voltage pulses. These pulses accelerate the free electrons. The free electrons undergo elastic and inelastic collisions with the starter gas. These collisions produce more electrons and heat the gas. Eventually the gas will become conductive.

The heated starter gas transfers its energy to the wall via thermal conduction. In this phase part of the input power is used to evaporate mercury and the metal-halide additives. Mercury will be fully evaporated while the additives will be present in the gas phase in the discharge as well as in the liquid and solid phase on the wall. This pool of salts on the wall is located at the coldest spot of the discharge vessel, called the coldspot. Its temperature determines how much of the additives will be present in the discharge. The coldspot temperature therefore has a large impact on the radiation output of the lamp.

1.4 Steady state phase

The steady state of the lamp is reached after a few minutes of operation. The energy received by the heavy particles due to collisions with electrons is balanced with the conduction, convection and radiation losses.

The conduction losses are partly caused by transfer of energy by collisions. The remaining part is caused by transport of chemical energy, called reactive conductivity.

Convection transports energy and particles due to changing densities. In specific conditions the combination of convection with radial diffusion can cause an axial segregation of species. More details are given in section 1.5.

Radiation can be separated in line radiation and continuum radiation. Line radiation is emitted when intra atomic or intra molecular transitions occur. Intra atomic transitions are electronic transitions. Intra molecular transitions can be electronic, rotational and vibrational transitions. In molecules every electronic state contains multiple rotational states and every rotational state contains multiple vibrational states. The large number of rotational and vibrational states can be approximated with a continuous distribution of energy states. The spectrum of a molecule is therefore often observed as continuous radiation. 'Real' continous radiation is caused by multi particle interactions. For example bremsstrahlung. bremsstrahlung is caused by the deceleration of electrons. The energy of the electron decreases and the excess energy is radiated as bremsstrahlung.

1.5 Segregation

In specific conditions the combination of convection and radial diffusion results in an axial segregation of species. The metal halide additives are not distributed homogeneously inside the discharge tube. As a result the radiation output is not constant along the axis of the lamp. This is undesirable. Axial segregation is investigated by examining convection and radial diffusion.

Radial segregation is driven by the density gradients of the species. In the absence of convection in the outer part of the discharge the diffusive flux of atoms directed outward is balanced by the molecules diffusing inwards. The diffusion of atoms is faster than the diffusion of molecules. The flux can only be balanced if the molecular partial pressure is larger than the atomic pressure. In the central part of the discharge the ionic flux outward is larger than the

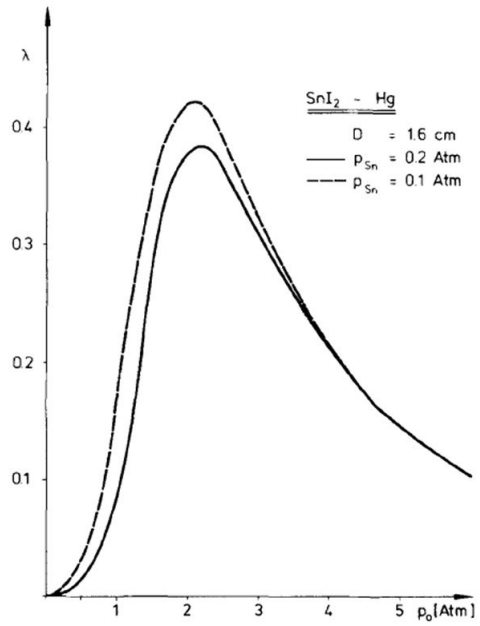

Figure 1.5.1: *Fischer curve for a lamp containing Sn, I and Hg taken from Fischer [23]. The segregation is minimized in the diffusion limit at very low pressures and in the convection limit at very high pressures.*

atomic inward flux due to ambipolar diffusion. As a consequence the atomic partial pressure is larger than the ionic partial pressure.

Axial segregation is driven by the convective flow. The species in the bottom of the lamp are heated on the axis of the discharge where the power input is high. Their temperature increases and therefore their density decreases. Due to the decreased density the species rise along the axis. Near the wall the opposite effect occurs. The species lose energy by conduction to the wall and will descent back to the bottom. When radial diffusion can not be neglected the radiating species reach the downward flow before they reach the top of the lamp. In these conditions the amount of radiating species in the top is much lower than in the bottom. These density gradients along the axis can create a non homogeneous luminous output.

A well mixed lamp has a small axial temperature gradient and produces light homogeneously. There are two regimes where such a mixed lamp exists. The first regime contains lamps with small convective flows. These flows are not strong enough to cause an axial temperature gradient. Those lamps are dominated by radial diffusion. The second regime contains lamps with strong convective flows which provide a good axial mixing. The intermediate regime is axially segregated.

Fischer [23] investigated the vertical segregation as a function of pressure. Fischer expressed the amount of segregation in a segregation parameter λ. By varying the pressure he could change the transport from a diffusion dominated to a convection dominated system as shown in figure 1.5.1. For low pressures Fischer approximated the reduced segregation parameter as a function of pressure p and lamp radius R by $\lambda \sim p^2R^3$. For high pressures the parameter is approximated by $\lambda \sim \left(p^2R^3\right)^{-1}$.

The ratio of the convective and diffusive fluxes can be expressed by the Peclet number. Beks [8] used $\frac{V_z}{L}$ and $\frac{D}{R^2}$ as a measure of the convective and diffusive rate respectively with V_z the axial bulk velocity on the axis halfway between the electrodes, L the inner length of the discharge tube, D the effective diffusion coefficient of an additive and R the inner radius of the discharge tube. He defined the Peclet number for HID lamps as

$$Pe = \frac{V_z R^2}{DL} \tag{1.1}$$

and concluded that axial segregation was strongest when the Peclet number was equal to one. Typical metal halide lamps are operated with conditions in the intermediate regime close to this segregation maximum.

1.6 Energy balance

The energy balance is a useful tool for lamp designers. It can be used to learn about the energy flows in the discharge. This knowlegde can then be applied for further increases in efficiency and color rendering. Current measurements generally only focus on the visible radiation. However, even for the efficient HID lamps more than half of the input power ends up as IR radiation. Therefore it is important to know where this radiation is lost and what processes are causing these losses. Only a few studies [2, 3, 4] exist where parts of the infrared have been measured. Not one of these studies contains spectrally resolved absolutely calibrated spectra above 2.5 µm measured with an integrating sphere. Measuring further into the infrared is getting increasingly more difficult due to the increasing influence of thermal radiation originating from the laboratory environment.

The input power of the lamp is distributed among the arc and the electrodes. The resistivity of the electrodes and the plasma determine how this power is distributed exactly. The power going into the plasma is partially converted to radiation. The remaining energy is lost non-radiatively. These losses are given by the heat flux to the wall. Thus the heat conductivity and the local temperature gradient near the wall determine this heat flux.

The ultraviolet discharge radiation mainly originates from the hot centre of the arc. In a commercial metal halide lamp the ultraviolet output is small due to reabsorption of this radiation and a low transmittance of the outer bulb. The visible and infrared radiation is emitted by atomic and molecular species. This radiation is emitted from the slightly cooler parts of the discharge arc as well. Part of the IR radiation is also caused by electron-ion and electron-atom bremsstrahlung which mainly originates from the centre of the arc.

The ceramic wall is heated due to absorption of parts of the UV, visible and IR discharge radiation. The wall is heated as well by the thermal radiation from the electrodes and the conductive heat flux from the plasma. The wall will mainly lose its energy as thermal radiation. The remaining energy is lost by conduction to the metallic structure holding the ceramic tube. Convection losses are neglected since the discharge tube is put in a low pressure environment. A schematic form of such an energy balance is given in Figure 1.6.1.

An energy balance can be determined with an integrating sphere. An integrating sphere is a sphere that can be used to quantify the spatially and angularly integrated spectral radiance. A radiative source can be mounted inside the sphere. The radiation of the source is reflected multiple times by the reflective surface of the sphere. A small hole is present in the sphere which allows some of the radiation to escape. The sphere can be calibrated by comparing the radiation from the sphere with the radiation from a reference source.

A calibrated setup can be used to determine the ultraviolet, visible and infrared contributions directly. By using time resolved measurements after switching off the lamp it is possible to distinguish between plasma discharge radiation and thermal radiation. The plasma radiation will disappear much faster than the slowly decaying thermal radiation. The thermal radiation can be determined by extrapolating the measured radiation back to the moment of switching off the lamp.

The non-radiative losses can be estimated according to Elenbaas [6] and Jack and Koedam [7]. They have shown that in general a linear relation exists between applied power and total radiated power. Lamps are measured at different powers. The radiated power can be plotted as a function of input power. With an extrapolation of this curve to zero discharge radiation an estimate can be made of the the conduction losses.

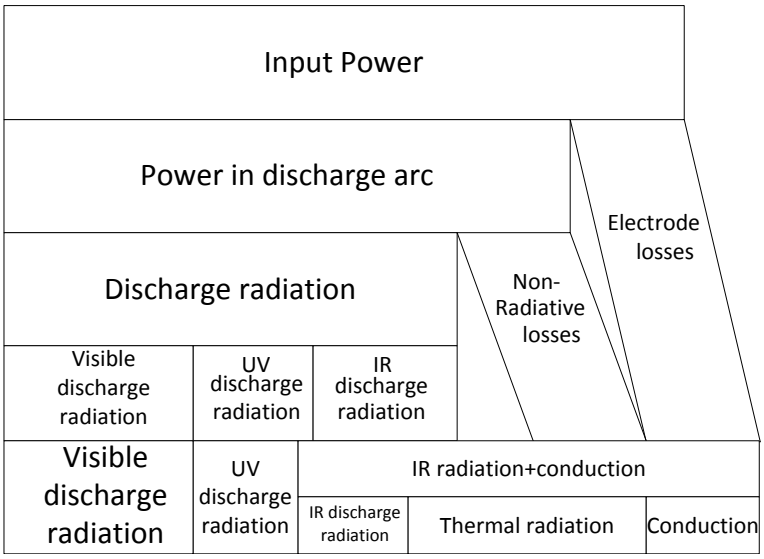

Figure 1.6.1: *Example of an energy balance. The input power is distributed among the electrodes and the discharge arc. The discharge loses its energy as radiation and by non-radiative processes like convection and conduction. The discharge radiation can be divided in visible, ultraviolet and infrared radiation. Part of this radiation is absorbed by the tube. The absorption of visible radiation is neglected here. The energy absorbed by the wall of the tube is lost as thermal radiation and as conduction to the metallic framework holding the tube.*

1.7 Project goals

Ceramic metal halide lamps (CMH) are the focus of this research. Commercial CMH lamps contain several metal-halide additives. Four lamps are discussed here which contain a simpler mixture of additives. The first lamp is the pure mercury lamp. Besides mercury the other lamps only contain one metal-halide additive. These additives are sodium iodide, thallium iodide and indium iodide. The goal of this project is to determine the complete energy balance of these lamps. Such an energy balance is used to aid in the development of better lamps.

A simulation model is made for these four lamps. This is a one-dimensional self-consistent model. The model accountd for ohmic heating, conduction and radiation losses. Raytracing according to Beks [8] and van der Heijden [9] accounts for the calculation of the radiative transport. The simulated energy balances are compared to the experimentally determined energy balances to verify the model's accuracy.

The experimental part of this work includes the calibration of an integrating sphere and the experimental determination of the energy balance of the previously mentioned four lamps. The far infrared is calibrated using a resistively heated platinum ribbon as a calibration source [5]. An analytical model is used to predict the spectral radiant flux of the strip based on literature data of the resistivity and the emissivity of platinum. Below a certain wavelength the platinum strip can not be used anymore as a calibration source since its thermal radiation rapidly decreases in the near infrared region. Below this wavelength a halogen lamp calibrated at Philips OCM calibration laboratories is used instead.

1.8 Thesis outline

In chapter 2 the theoretical concepts of the transport equations and the radiative energy transport are discussed. This chapter also clarifies the Jack-Koedam theory. In chapter 3 is shown how these equations are implemented in a one dimensional model. In chapter 4 the model is calibrated by

comparing the simulated spectra with lamps which can be considered one dimensional. The modeling results for the single salt lamps are shown as well. In chapter 5 the setup and the experimental procedures are discussed. Chapter 6 contains the experimental results. These are the calibrated spectra, powerscans and switch-off measurements. In chapter 7 a comparison is made between the results obtained in experiments and in the model. Chapter 8 contains the most important conclusions of this work.

Chapter 2

Theory

In this chapter the physics required for a basic understanding of a metal halide lamp is presented. The assumption of local thermodynamic equilibrium is discussed first. Then the transport equations and transport constants that are important for our lamp plasmas are discussed. Special attention is given to radiative transport due to its non-local nature. After that the Jack-Koedam theory is considered.

2.1 Local thermodynamic equilibrium

The assumption of local thermodynamic equilibrium (LTE) simplifies the description of a lamp system. In LTE all species have the same temperature. Additionally, the densities of the ground state and all excited states can be described with this temperature. The lamp can therefore be described by only a few parameters. These parameters are the input power, plasma temperature distribution, the radius of the discharge tube and the vapour pressures of the species present in the discharge.

Elenbaas [6] gives four statements which are required for a valid LTE assumption. Two of these statements are discussed in this section. Those statements describe the validity of the Boltzmann and Saha equations. These equations are assumed to be valid if processes restoring LTE are much faster than processes which result in non LTE distributions. The Boltzmann distribution can for example be used when electron impact excitation and deexcitation are much faster than spontaneous radiation. The statements are:

1. The number of excitations by electron impact is large compared with the number of spontaneous transitions

2. The difference between the gas temperature and the electron temperature is small

Elenbaas derived scaling expressions for every statement for a pure mercury discharge. These expressions are not valid for metal halide lamps in general. They are therefore used here as a first approximation. The validity of the first statement scales with the electron density which is rewritten by Elenbaas as

$$n_e \sim \frac{(P - P_{cond})^{\frac{2}{3}}}{p^{\frac{1}{6}} d^{\frac{4}{3}}}, \tag{2.1}$$

with P the input power per unit length, P_{cond} the conduction losses per unit length, p the pressure and d the diameter of the lamp. The input power minus the conduction losses per unit length $P - P_{cond}$ can also be expressed as P_{rad} which are the radiation losses per unit length. Since the number of electrons decays as a function of the radius statement 1 will always be unsatisfied from a certain radius. Elenbaas states that if almost all of the radiation originates before this point the radiation field can be considered to be in equilibrium with the gas.

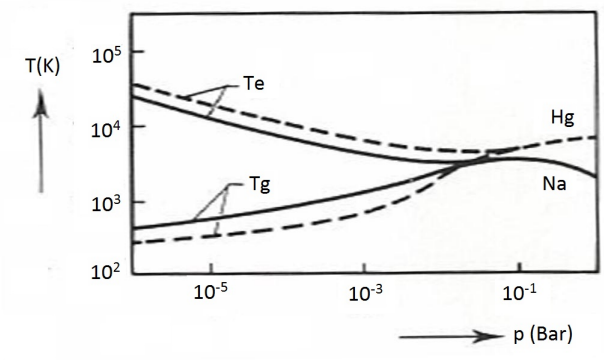

Figure 2.1.1: *Electron and gas temperatures in the centre of the discharge as a function of pressure for a mercury and a sodium lamp. At operating conditions above* 0.1 *bar the electron and gas temperatures are considered to be equal. This result was taken from de Groot and van Vliet [11].*

The electron temperature always exceeds the gas temperature since energy is transfered from the potential field to the electrons and then from the electrons to the gas by collisions. The scaling expression for the difference between electron and gas temperature is given by

$$(T_e - T_g) \sim \frac{1}{p^{\frac{5}{6}} d^{\frac{2}{3}} \left(P - P_{cond}\right)^{\frac{2}{3}}}. \tag{2.2}$$

A conclusion from these scaling expressions is that a high input power per unit length is favourable for all criteria. High pressures are favourable for statement 2 and sligthly unfavourable for statement 1. Small diameters are favourable for statement 1 and unfavourable for statement 2. Since metal halide lamps can be characterized by their high input power, high pressure and small diameter statement 1 can be considered to be valid in the centre of the discharge. Statement 2 will be investigated further.

De Groot and van Vliet [11] obtained the electron and gas temperatures in the centre of the discharge as a function of pressure for a mercury lamp and a sodium lamp. Their results are shown in Figure 2.1.1 and show that in the centre of the discharge the electron and gas temperatures for pressures above 0.1 bar are approximately equal. A typical metal halide lamp contains mercury pressures which are significantly above this limit. In the hot central core LTE can be assumed to be valid. However closer to the wall the electron and gas temperatures start to deviate significantly. A reasoning similar to Elenbaas can be applied here as well. If this significant deviation between electron and gas temperatures occurs at a radius where emission of radiation is negligible and almost no current passes through these outer parts the discharge can be considered to be in LTE.

2.2 Transport equations

The transport equations necessary to describe the local properties of a given species can be derived from a general equation called the Boltzmann transport equation. These properties are for example the local particle concentrations, velocity and temperature of a species in the plasma. The Boltzmann transport equation is discussed first. After that the transport equations for the species are derived. These species equations can be summed to describe the bulk behavior of the plasma. The bulk equations are then reduced to a one dimensional system of equations. By following such a procedure the number of equations is greatly reduced.

2.2.1 Boltzmann transport equation

The Boltzmann transport equation for species i is expressed in the particle density function $f_i(\vec{x},\vec{v})$. This function gives the number of particles of species i present in a volume d^3x at position $\vec{x}$ with velocities between $\vec{v}$ and $\vec{v}+d^3v$. The number of particles of species i at position $\vec{x}$ can thus be expressed as $f_i(\vec{x},\vec{v})\,d^3xd^3v$. This six dimensional space is called phase space. The Boltzmann equation for species i is given by

$$\frac{\partial f_i(\vec{x},\vec{v})}{\partial t} + v_i \cdot \nabla f_i(\vec{x},\vec{v}) + \frac{\vec{F_i}}{m_i} \cdot \nabla_v f_i(\vec{x},\vec{v}) = \left(\frac{\partial f_i(\vec{x},\vec{v})}{\partial t}\right)_{collisions}. \tag{2.3}$$

The first term in the Boltzmann transport equation describes the changes in density with respect to time. The second and third term describe how the density in phase space changes with respect to position and velocity respectively. The index v in the gradient in the third term means that the gradient is taken with respect to the velocity. This gradient is caused by an external volumetric force $\vec{F_i}$. The last term describes changes in phase space which are caused by the creation and destruction of particles of species i or by sudden changes in velocity which can for example be caused by collisions.

2.2.2 Species transport equations

The species transport equations can be derived from the Boltzmann equation by considering the first three moments. A moment can be derived from the Boltzmann transport equation by multiplying the particle density function with a weight function $g(v)$ and integrating over all velocities. The first moment can be generated with $g(v)=1$ and gives the particle density

$$n_i(\vec{x},t) = \int f_i(\vec{x},\vec{v})\,d\vec{v}. \tag{2.4}$$

The second moment is generated with $g(v)=\vec{v}$ and gives the particle flux

$$\Gamma_i(\vec{x},t) = n_i(\vec{x},t)\,\vec{u_i} = \int f_i(\vec{x},\vec{v})\,\vec{v}d\vec{v}, \tag{2.5}$$

where $\vec{u_i}$ is the average velocity of species i. The third moment is generated with $g(v) = \frac{1}{2}m_i(\vec{v_i}-\vec{u_i})^2$ and gives the internal energy of species i. This is proportional to the random motion of the particles

$$\frac{3}{2}k_B n_i(\vec{x},t)\,T_i(\vec{x},t) = \int f_i(\vec{x},\vec{v})\,(\vec{v_i}-\vec{u_i})^2\,d\vec{v}. \tag{2.6}$$

The species transport equations can be derived by applying the same procedure as outlined above to the Boltzmann transport equation. These equation are

- the species continuity equation

$$\frac{\partial n_i}{\partial t} + \nabla \cdot \Gamma_i = S_i, \tag{2.7}$$

  with S_i a source of species i. Particles can be created or destroyed by inelastic processes.

- the species momentum balance

$$\frac{\partial}{\partial t}(\rho_i \vec{u_i}) + \nabla \cdot (\rho_i \vec{u_i}\vec{u_i}) = -\nabla \cdot P_i + n_i\vec{F_i} + \sum_j \vec{R_{ij}} + S_i^m, \tag{2.8}$$

  with $\rho_i = m_i n_i$ is the mass density, S_i^m is a source of momentum generated by collisions, $\vec{R_{ij}}$ is the friction force caused by other particle fluxes

$$\vec{R_{ij}} = \int m_i \vec{u_i}\left(\frac{\partial f_i(\vec{x},\vec{v})}{\partial t}\right)_{coll}^{j} d\vec{v_i}$$

and P_i is the pressure tensor

$$P_i = \rho_i \left\langle (\vec{v} - \vec{u_i}) (\vec{v} - \vec{u_i}) \right\rangle .$$

- the species energy balance

$$\frac{\partial \rho_i e_i}{\partial t} + \frac{1}{2}\frac{\partial \rho_i u_i^2}{\partial t} + \nabla \cdot (\rho_i e_i \vec{u_i}) + \frac{1}{2}\nabla \cdot \left(\rho_i u_i^2 \vec{u_i}\right) + (\nabla \vec{u_i}) : P_i + \nabla \cdot \vec{q_i} - n_i \vec{F_i} \cdot \vec{u_i} = S^E, \quad (2.9)$$

with e_i is the thermal energy per unit mass, $\vec{q_i}$ is the heat flux and S^E is the energy source term.

2.2.3 Local density calculation

The calculation time of species densities can be reduced by introducing an elemental density. A general species transport equation can be expressed in these elemental densities. After that the limits of strong convection and strong diffusion are considered to reduce this equation to a more simple form.

The system of multiple species continuity equations 2.7 can be rewritten in terms of elemental densities. In LTE the particle density can be described by the local elemental density, pressure and temperature. The elemental density can be expressed as

$$n_\alpha = \sum_i n_i R_{i\alpha}, \quad (2.10)$$

with n_α the elemental density, n_i the species density and $R_{i\alpha}$ the stoicheometric coefficient. For example in a pure mercury lamp it's sufficient to consider the following species: Hg, Hg^+, Hg_2. The elemental density of mercury can then be expressed as

$$n_{\{Hg\}} = n_{Hg} + n_{Hg^+} + 2n_{Hg_2}. \quad (2.11)$$

Curly brackets are used to indicate that the elemental density is considered. An elemental pressure can be introduced by using the ideal gas law as

$$p_\alpha = n_\alpha k_B T. \quad (2.12)$$

Summation of the species continuity equations results in the elemental continuity equation given by

$$\nabla \cdot \left(\frac{D_\alpha}{k_B T} \nabla p_\alpha + \frac{p_\alpha}{k_B T} \vec{c_\alpha} \right) = 0, \quad (2.13)$$

where D_α is the elemental diffusion coefficient and $\vec{c_\alpha}$ is the elemental velocity. In equation 2.13 the source term is absent. This means that the elemental flux is conserved and that elements can not be created or destroyed.

In the diffusion and convection limits derived by Fischer [23] Eq 2.13 can be replaced by more simple expressions.

The convection limit is achieved at high pressures and at large radii. The strong convection makes sure that the additives are well mixed. As an approximation it can be assumed that the elemental pressure is constant as a function of the radius [24]:

$$\sum_i R_{i\alpha} p_i = p_\alpha = n_\alpha k_B T = constant, \quad (2.14)$$

with p_i the partial pressure of species i and α the element under consideration. The constant value of the elemental pressure can be obtained at the coldspot since this value only depends on the coldspot temperature.

The diffusion limit is achieved at low buffer gas pressures and at small radii. In this limit the following approximation can be made [24]:

$$\sum_i D_i^* R_{i\alpha} p_i = C_\alpha = \sum_i D_i^* R_{i\alpha} n_a k_B T = constant, \tag{2.15}$$

with D_i^* the reduced (temperature independent) binary diffusion coefficient calculated for hard sphere interactions between species i and the buffer gas (mercury). By introducing the effective elemental diffusion coefficient D_{eff} defined as

$$D_{eff} = \frac{\sum_i D_i^* R_{i\alpha} p_i}{\sum_i R_{i\alpha} p_i} = \frac{\sum_i D_i^* R_{i\alpha} n_i}{\sum_i R_{i\alpha} n_i}, \tag{2.16}$$

the elemental pressure can be obtained from an iterative procedure. The first iteration uses the result of the convection limit. The remaining iterations calculate the partial pressure with an underrelaxation parameter δ as

$$p_\alpha = n_\alpha k_B T = \frac{C_\alpha}{D_{eff}} \delta + (1 - \delta)\, p_{\alpha, previous}$$

until the final result is considered to be sufficiently converged.

The calculated elemental pressures, obtained from the convection or diffusion limit, can be supplied to CHEMAPP which is a commercial program for Gibbs energy minimization. For all species the chemical potential is set to zero as

$$\mu_i = \left.\frac{\partial G}{\partial N_i}\right|_{T,p} = 0, \tag{2.17}$$

with the constraint that the summed elemental density inside the lamp is equal to an input value B_α

$$\sum_i R_{i\alpha} N_i = B_\alpha. \tag{2.18}$$

The Gibbs energy for species i in the gas can be expressed as

$$\mu_i = \mu_i^0 (T) + RTln\left(\frac{N_i}{N_0}\right) + ln\left(\frac{p_i}{p_0}\right) \tag{2.19}$$

and at the cold spot temperature with

$$\mu_i = \mu_i^0 (T)\,. \tag{2.20}$$

2.2.4 Bulk equations

The species transport equations can be summed to obtain the bulk transport equations. The results in this section are similar to Beks [8]. By using the following relation for the average species velocity

$$\vec{u_i} = \vec{u} + \vec{u_i}',$$

where $\vec{u}$ is the average bulk velocity and $\vec{u_i}'$ is the deviation from this velocity and summing all species force balances (2.8) the result is [32]

$$\frac{\partial}{\partial t}(\rho\vec{u}) + \sum_i \nabla \cdot \rho_i \left(\vec{u_i}'\vec{u_i}' + 2\vec{u_i}'\vec{u} + \vec{u}\vec{u}\right) = \sum_i \left(-\nabla \cdot P_i + \frac{\rho_i}{m_i}\vec{F_i}\right). \tag{2.21}$$

This expression can be rearranged to the Navier-Stokes equation

$$\frac{\partial}{\partial t}(\rho\vec{u}) + \nabla \cdot \rho\vec{u}\vec{u} = -\nabla \cdot P + \sum_i \left(\frac{\rho_i}{m_i}\vec{F}_i\right), \tag{2.22}$$

with the pressure tensor

$$P = \sum_i \left(P_i + \rho_i \vec{u_i}' \vec{u_i}'\right) = \Pi + pI = \Pi + \frac{1}{3}\sum_i \rho_i \left\langle (\vec{v_i} - \vec{u_i})^2 \right\rangle I,$$

where Π is the viscosity tensor and p is the scalar pressure. For a Newtonian fluid the viscosity tensor can be related to the dynamic viscosity μ. The Navier-Stokes equation then reduces to

$$\frac{\partial}{\partial t}(\rho\vec{u}) + \nabla \cdot \rho\vec{u}\vec{u} = -\nabla p + \nabla \cdot (\mu\nabla\vec{u}) + \sum_i \left(\frac{\rho_i}{m_i}\vec{F}_i\right). \tag{2.23}$$

Similarly the species energy balances (2.9) can be summed. By subtracting the force balance and the equation of mass conservation multiplied with $\frac{1}{2}\rho v^2$ the following equation can be obtained [32]

$$\nabla \cdot (c_V \vec{u}\nabla T) + P : \nabla\vec{u} + \nabla \cdot \vec{q} + p \cdot \nabla\vec{u} = \sigma E^2 - q_{rad}, \tag{2.24}$$

where c_V is the volumetric heat capacity, σ is the electrical conductivity and $\vec{q}$ is the heat flux. The terms in the energy balance represent: energy transported by convection, viscous dissipation, energy transported by a heat flux, compression work, ohmic dissipation and q_{rad} is the power emitted or absorbed by the radiation field.

2.2.5 1D transport equations

Elenbaas [6] described the high pressure mercury lamp successfully using a one dimensional approach. In this section a similar approach is made to describe metal halide lamps. Due to the inherent non 1D nature of most CMH lamps such an appoach can only give approximate results. The discharge tube's diameter to height ratio of the lamps that are discussed in this work indeed result in non 1D behavior.

2.2.5.1 Momentum balance

When the axial velocity is known an estimate of the Peclet number can be made. The Peclet number can be used as an indication of the validity of the convection or diffusion limit. Elenbaas developed a method of solving the momentum balance, Eq 2.8 by neglecting the total derivative. The bulk momentum balance then reduces to

$$-\nabla p + \nabla \cdot (\mu\nabla\vec{u}) + \rho g = 0. \tag{2.25}$$

For a vertically operated lamp the velocity can be approximated to be a function of the radius only. The velocity has one non zero component which is directed along the axis of the discharge. The momentum balance for the axial component can then be written as

$$-\frac{\partial p}{\partial z} + \frac{1}{r}\frac{\partial}{\partial r}\left(\mu r \frac{\partial u_z}{\partial r}\right) + \rho g = 0. \tag{2.26}$$

The pressure gradient along the axis is assumed to be independent of the radius. Multiplication with the radius and integration over the radius then gives

$$-\frac{\partial p}{\partial z}\frac{r^2}{2} + \mu r \frac{\partial u_z}{\partial r} + g\int_0^r \rho r" dr" = C, \tag{2.27}$$

with C an integration constant. By evaluating the equation at $r = 0$ it is concluded that $C = 0$. After dividing by the viscosity and the radius and integrating over the radius an expression for the axial velocity is obtained:

$$u_z(r) = u_z(0) + \frac{\partial p}{\partial z} \int_0^r \frac{r'}{\mu} dr' - \int_0^r \frac{g}{r'\mu} \left[\int_0^{r'} \rho r" dr" \right] dr'. \tag{2.28}$$

The velocity at the axis can be calculated by applying the no slip condition at the wall

$$u_z(0) = -\frac{\partial p}{\partial z} \int_0^R \frac{r'}{\mu} dr' + \int_0^R \frac{g}{r'\mu} \left[\int_0^{r'} \rho r" dr" \right] dr'. \tag{2.29}$$

An expression for the pressure gradient can be obtained by calculating the total mass flow in axial direction and setting it to zero. The results is

$$\frac{\partial p}{\partial z} = \frac{-\int_0^R \rho r \left[\int_r^R \frac{1}{r'\mu} \left(\int_0^{r'} \rho r" dr" \right) dr' \right] dr}{\frac{1}{2} \int_0^R \rho r \left[\int_r^R \frac{r'}{\mu} dr' \right] dr}. \tag{2.30}$$

Due to the reduction of the momentum balance to one dimension the derived equations are only valid for long and thin lamps. However for a metal halide lamp the axial velocity and pressure gradient should still be a reasonable approximation in the plane halfway between the electrodes.

2.2.5.2 Energy balance

The energy balance equation, Eq 2.24, was reduced to one dimension by Elenbaas and Heller by neglecting convection, viscous dissipation and compression work. That means the heat flux, ohmic heating and the radiation losses make up the energy balance as

$$\nabla \cdot q = \sigma E^2 - q_{rad}, \tag{2.31}$$

with the heat flux given by Fourier's law as

$$q = -\lambda \nabla T. \tag{2.32}$$

The heat flux contains the thermal conductivity, λ, which can be expressed as the sum of the reactive, λ_r, and the collisional, λ_c conductivity. The collisional conductivity represents the energy transfered by particle collisions. The reactive conductivity accounts for the energy transfered via chemical reactions. An example of such a reactive transport mechanism is the recombination process: Neutral particles diffuse into the hot core and are ionized. At the same time ions and electrons will diffuse out of the hot core and then recombine. This complete process effectively results in the transport of the ionization energy from the hot core to the colder areas of the discharge. Similar contributions result from dissociation and association reactions for molecular species.

In the one dimensional approximation it is assumed that the electric field is constant along the radius of the discharge tube. The electric field can then be calculated by integrating the ohmic heating term as

$$P_{discharge} = P_{in} - P_{elec} = \int_0^R 2\pi r h_{elec} \sigma(r) E^2 dr, \tag{2.33}$$

which results in an electric field of

$$E = \sqrt{\frac{P_{in} - P_{elec}}{h_{elec} \int_0^R 2\pi r \sigma(r) dr}}. \tag{2.34}$$

In these equations P_{in} is used for the input power, P_{elec} is used for the dissipated power in the electrodes, h_{elec} is used for the distance between the electrodes and σ represents the electrical conductivity.

2.3 Transport constants

The calculations of the transport coefficients which appear in Eq 2.31 , the energy balance, are discussed in this section. These transport coefficients are the electrical and reactive conductivities. The electrical conductivity [12] can be expressed as

$$\sigma_e = \frac{n_e e^2}{m_e \overline{\nu_{ea}}}, \tag{2.35}$$

with n_e the electron density, e the elementary charge, m_e the mass of an electron and $\overline{\nu_{ea}}$ the sum of the electron-heavy particle collision frequencies. The collision frequency [13] can be written as

$$\nu_{ea} = n_a \int_0^\infty u f(u) Q_{ea}(u) du = n_a \left\langle u Q_{ea}(u) \right\rangle, \tag{2.36}$$

with n_a the heavy particle density of species a, u the velocity, $f(u)$ the Maxwell-Boltzmann velocity distribution and $Q_{ea}(u)$ the electron-heavy particle momentum transfer cross section. In LTE the Maxwell-Boltzmann velocity distribution can be calculated exactly with

$$f(u) = 4\pi \left(\frac{m}{2\pi k_B T} \right)^{\frac{3}{2}} u^2 e^{\frac{m u^2}{2 k_B T}}. \tag{2.37}$$

In metal halide lamps the additive densities are relatively low in comparison with the buffer gas densities. The electron-heavy particle collision frequencies can therefore be approximated with the electron-buffer gas collision frequency. For the lamps investigated in this project the buffer gas is mercury.

The expression for the reactive conductivity is taken from Butler and Brokaw [14, 15]. They reduce the system of chemical reactions to a system of χ independent reactions. An independent reaction is defined as a reaction which can not be written as the sum of other reactions. Independent reaction i can be written as

$$\sum_{k=1}^{\mu} n_{ik} X^k = 0, \tag{2.38}$$

with n_{ik} the stoicheometric coefficient of species k in independent reaction i, X^k represents species k and μ is the total number of species. If species k is not involved in reaction i then the stoicheometric coefficient n_{ik} is zero. The reaction energy of independent reaction i can be written as

$$\Delta H_i = \sum_{k=1}^{\mu} n_{ik} H_k, \tag{2.39}$$

with ΔH_i the reaction energy of independent reaction i and H_k the enthalpy of species k. For such a system the reactive conductivity can be expressed as

$$\lambda_r = -\frac{1}{RT^2} \frac{\begin{vmatrix} A_{11} & \cdots & A_{1\nu} & \Delta H_1 \\ \vdots & & \vdots & \vdots \\ A_{\nu 1} & \cdots & A_{\nu\nu} & \Delta H_\nu \\ \Delta H_1 & \cdots & \Delta H_\nu & 0 \end{vmatrix}}{\begin{vmatrix} A_{11} & \cdots & A_{1\nu} \\ \vdots & & \vdots \\ A_{\nu 1} & \cdots & A_{\nu\nu} \end{vmatrix}}, \tag{2.40}$$

with R the gas constant. The vertical bars indicate that the determinant of the matrix is taken. The matrix elements A_{ij} are given by

$$A_{ij} = A_{ji} = \sum_{k=1}^{\mu-1} \sum_{l=k+1}^{\mu} \frac{RT}{D_{kl}p} x_k x_l \left[\frac{n_{ik}}{x_k} - \frac{n_{il}}{x_l}\right] \left[\frac{n_{jk}}{x_k} - \frac{n_{jl}}{x_l}\right], \tag{2.41}$$

with p the pressure of the gas, x_k the partial pressure of species k and D_{kl} the binary diffusion coefficient for species k and l.

The expression for the binary diffusion coefficient is taken from Johnston [16] and is given by

$$D_{kl} = \frac{3}{16} \frac{k_B^2 T^2}{p\mu_{kl}\Omega_{kl}^{(1,1)}}, \tag{2.42}$$

with μ_{kl} the reduced mass and $\Omega_{kl}^{(1,1)}$ the collision integral. The collision integral can be calculated as

$$\Omega_{kl}^{(1,1)} = \sqrt{\frac{k_B T}{2\pi\mu_{kl}}} \int_0^\infty e^{-\gamma^2} \gamma^5 Q_{kl}(g) d\gamma, \tag{2.43}$$

with γ the dimensionless energy given by $\gamma = \frac{\mu g^2}{2k_B T}$, g is the velocity difference between particles k and l and Q_{kl} is the momentum transfer cross section.

When determining momentum transfer cross sections in a plasma three types of interactions can be distinguished. These are the neutral-neutral, charged-neutral and charged-charged interactions. The momentum transfer cross section for neutral-neutral interactions is taken as

$$Q_{ab} = \pi \left(\frac{R_a + R_b}{2}\right)^2, \tag{2.44}$$

with R_i the hard sphere radius of particle i. The momentum transfer cross section for charged-neutral interactions is given by the Langevin polarizability model [12] as

$$Q_{a+b} = \sqrt{\frac{\pi\alpha_b q_a^2}{\mu_{ab}\epsilon_0 g_{ab}^2}}, \tag{2.45}$$

with α_b the polarizability of the neutral particle in m^3, q_a the charge of the charged particle, ϵ_o the electrical permittivity and g_{ab} the velocity difference between particles a and b. The momentum transfer cross section for charged-charged interactions is given by the shielded Coulomb cross section as

$$Q_{a^+b^+} = 4\pi b_0^2 ln \left[\sqrt{1 + \left(\frac{\lambda_D}{b_0}\right)^2}\right], \tag{2.46}$$

with b_0 given by

$$b_0 = \frac{Z_a Z_b e^2}{12\pi\epsilon_0 k_B T}, \tag{2.47}$$

where Z_a is the charge of particle a expressed in elementary charges. In equation 2.46 λ_D is the Debye length given by

$$\lambda_D = \sqrt{\frac{\epsilon_0 k_B T}{n_e e^2}}. \tag{2.48}$$

2.4 Radiation

In this section the term q_{rad} from the energy balance, Eq 2.31, is discussed. Due to the non local nature of emission and absorption processes a calculation of this term is not straight forward. The consequences of the LTE assumption are discussed here along with a discrete solution of the

equation of radiative transport and a short summary of line broadening theory. A more detailed discussion of radiation theory is given by van der Heijden [9].

All equations are derived in units of frequency (units: Hz), ν. In spectroscopy it is customary to express spectra in wavenumbers (units: cm^{-1}), $\tilde{\nu}$. These quantities are related by

$$\nu\left(Hz\right) = \frac{c}{\lambda\left(m\right)} = \frac{c\tilde{\nu}\left(cm^{-1}\right)}{100}, \tag{2.49}$$

with c the speed of light and λ the wavelength.

2.4.1 Radiative transport

The power transported by radiation can be expressed as a function of the radiative flux. The radiative flux is a function of the radiance. The radiance is determined by the local properties of the plasma and can be calculated with the equation of radiative transport. This equation is given by

$$\frac{dI}{ds} = j - \kappa I, \tag{2.50}$$

with j the emission (units: $Wm^{-3}Hz^{-1}sr^{-1}$), κ the absorption (units: m^{-1}), I the radiance (units: $Wm^{-2}Hz^{-1}sr^{-1}$) and s the path (units: m) traversed by the radiation. Its important to note that the emission, absorption and the radiance all depend on the local composition of the plasma. The radiative flux, Φ (units: WHz^{-1}), passing through a surface area, A, in the direction $\vec{s}$, covering a solid angle, $d\Omega$, is given by

$$\Phi = I\vec{s}\cdot\vec{A}d\Omega = Id\vec{\Omega}\cdot\vec{A}. \tag{2.51}$$

The power density passing through that surface can then be calculated by integrating over the frequency

$$P_{rad} = \int \frac{\Phi}{V} d\nu, \tag{2.52}$$

with V the local volume of the considered gas.

2.4.2 Radiation in LTE

Three types of radiation are discussed in this section: Atomic, molecular and continuous radiation. In general for none of these processes direct relations exist between the emission and absorption. Both quantities have to be calculated separately before the equation of radiative transport can be solved.

For atomic radiation the emission can be calculated as

$$j = \frac{h\nu}{4\pi} A n_u \phi\left(\nu\right), \tag{2.53}$$

with h Planck's constant, ν the frequency corresponding to the difference between the energy levels of the radiator, A the Einstein coefficient of spontaneous decay, n_u the density of species in the upper energy state of the transition and $\phi\left(\nu\right)$ is the line profile. The absorption should be calculated independent of the emission as

$$\kappa = \sigma_{abs}\left(\nu\right) n_l - \sigma_{stim}\left(\nu\right) n_u, \tag{2.54}$$

with $\sigma_{abs}\left(\nu\right)$ the cross section for absorption, $\sigma_{stim}\left(\nu\right)$ the cross section for stimulated emission and n_l the density of species in the lower energy state of the transition. However in LTE the radiation field is in equilibrium with the gas. That means that equation 2.50 reduces to

$$j = \kappa I, \tag{2.55}$$

which states that the amount of emitted radiation is equal to the absorbed radiation. From LTE theory it is also known that the radiance emitted by an object is equal to the blackbody radiance, I_{BB}, given by

$$I_{BB} = \frac{2h\nu^3}{c^2} \frac{1}{exp\left(\frac{h\nu}{k_B T}\right) - 1}, \tag{2.56}$$

with c the speed of light in vacuum. These considerations lead to a direct relation of the absorption with the emission given by

$$\kappa = \frac{j}{I_{BB}}. \tag{2.57}$$

For atomic radiation the absorption is thus given by

$$\kappa = \frac{c^2 A n_u \phi(\nu)}{8\pi\nu^2} \left(exp\left(\frac{h\nu}{k_B T}\right) - 1\right). \tag{2.58}$$

Molecular radiation can also be included with Eq 2.57 similar to atomic radiation if the molecular emission can be calculated. However molecular radiation is more complex since the electronic states are split up further in rotational and vibrational states. The calculation of molecular emission requires knowledge of the potential curves as a function of intermolecular separation and also requires accurate transition probabilities. Due to the difficulty of obtaining this data molecular radiation is out of the scope of this work.

Continuous radiation can also be included with Eq 2.57. This radiation arises from electron-ion interactions. Electrons and ions can recombine to form atoms. The kinetic energy of the electron and the ionization energy can be released as radiation:

$$A^+ + e^- + E_{kin} \rightarrow A + h\nu. \tag{2.59}$$

A second interaction involves the ion reducing the speed of the electron. The energy lost by the electron in this 'breaking process' is radiated as bremsstrahlung:

$$A^+ + e^- + E_{kin,1} \rightarrow A^+ + e^- + E_{kin,2} + h\nu. \tag{2.60}$$

2.4.3 Discretized radiance calculation

The calculation of radiative energy transport can in general not be expressed as an analytical expression. Computer models are required for these calculations. These models require a discretization of a system in control volumes. In this section an expression for the change in radiance is calculated for an arbitrary direction through an arbitrary control volume.

The solution of Eq 2.50 can be written down in integral form as

$$I(s) = \int_{s_0}^{s} j\left(s^{'}\right) exp\left(-\int_{s^{'}}^{s} \kappa\left(s^{"}\right) ds^{"}\right) ds^{'}, \tag{2.61}$$

which can be simplefied as

$$I(s) = \int_{s_0}^{s} j\left(s^{'}\right) exp(-\tau)\, ds^{'}, \tag{2.62}$$

by introducing the optical depth, τ, defined as

$$\tau = \int_{s^{'}}^{s} \kappa\left(s^{"}\right) ds^{"}. \tag{2.63}$$

An arbitrary discretization can be applied for the integration of Eq 2.62 through one control volume. The following result can be obtained for the radiance originating in this single control volume given by

$$\int_{s}^{s+\Delta s_k} j\left(s^{'}\right) exp\left(-\kappa\left(s^{'}\right)\left(s + \Delta s_k - s^{'}\right)\right) ds' = \frac{j_k}{\kappa_k}\left[1 - exp(-\kappa_k \Delta s_k)\right], \tag{2.64}$$

with Δs_k the distance traversed through control volume k. This result has been obtained by using constant values for the emission, j_k and absorption, κ_k for the entire volume represented by control volume k. By also considering the radiance which entered this control volume, I_k, the radiation leaving this volume, I_{k+1} is given by

$$I_{k+1} = I_k exp\left(-\kappa_k \Delta s_k\right) + \frac{j_k}{\kappa_k}\left[1 - exp\left(-\kappa_k \Delta s_k\right)\right] = I_k exp\left(-\tau_k\right) + \frac{j_k}{\kappa_k}\left[1 - exp\left(-\tau_k\right)\right]. \quad (2.65)$$

The change of the radiance in one control volume, ΔI_k, can then be expressed as

$$\Delta I_k = I_{k+1} - I_k = \left(\frac{j_k}{\kappa_k} - I_k\right)\left[1 - exp\left(-\tau_k\right)\right]. \quad (2.66)$$

By applying the LTE result for the absorption this equation can be rewritten as

$$\Delta I_k = \left(I_{BB,k} - I_k\right)\left[1 - exp\left(-\tau_k\right)\right], \quad (2.67)$$

which makes the interpretation of the change in radiance easier. In LTE the difference between the ingoing radiance, I_k and the local blackbody radiance, $I_{BB,k}$ is being reduced by a factor $[1 - exp\left(-\tau_k\right)]$ inside control volume k. Two limits can be distinguished. In the optical thick limit $\tau \ggg 1$ which means the outgoing radiance, I_{k+1} is always equal to the local blackbody radiance, $I_{BB,k}$. In this case the power emitted as radiation can be calculated locally as

$$P_{rad} = \int\int\int I_{BB} d\vec{\Omega} \cdot d\vec{A} d\nu. \quad (2.68)$$

In the optical thin limit $\tau \lll 1$ which means Eq 2.66 can be approximated by

$$\Delta I_k \approx \left(\frac{j_k}{\kappa_k} - I_k\right)\kappa_k \Delta s_k = j_k \Delta s_k - I_k \kappa_k \Delta s_k \approx j_k \Delta s_k. \quad (2.69)$$

The power emitted as thin radiation can be calculated locally as

$$P_{rad} = \int\int j \cdot 4\pi dV d\nu. \quad (2.70)$$

In general a local calculation of the radation is not possible. The results will depend on the geometry. In section 3.2.3 the implementation for a cylindrical geometry is discussed.

2.4.4 Line broadening

In this section a few mechanisms responsible for line broadening are discussed. These are natural, Doppler, resonance, Stark and van der Waals broadening. Resonance, Stark and van der Waals broadening are all considered in the impact limit. Additionally, van der Waals contributions in the quasistatic limit are considered as well. Experimental broadening is not discussed in this section.

Line broadening is generally calculated in either the impact or the quasi static regime. The impact regime assumes that collisions occur instantaneously: The time required for one collision is much smaller than the average time between two collisions. In the quasi static theory the perturbing particles are assumed to travel only a small distance during the lifetime of the excited state and can thus be considered as static particles. Due to the differences in lifetime the impact theory predicts the core of a line profile while the wings are described by quasi static theory [18]. Tortai [18] gives a short summary of the validity of the approaches. The transition from impact to quasi static theory is predicted to occur at a wavelength limit, $\Delta\lambda_L$ given by

$$\Delta\lambda_L = \frac{\lambda^2 W}{2\pi c \rho_w}, \quad (2.71)$$

with λ the unperturbed wavelength of the transition, W the average thermal velocity of the interacting species and ρ_w the Weisskopf radius. Sobelman [19] provides an expression for the Weisskopf radius given by

$$\rho_w = \left(\frac{\alpha_n C_n}{W}\right)^{\frac{1}{n-1}}, \tag{2.72}$$

with α_n a constant expressed in the gamma function, Γ, as

$$\alpha_n = \sqrt{\pi}\frac{\Gamma\left(\frac{n-1}{2}\right)}{\Gamma\left(\frac{n}{2}\right)} \tag{2.73}$$

and n and C_n are given by the type of interaction responsible for line broadening

$$V = \hbar\frac{C_n}{r^n}. \tag{2.74}$$

2.4.4.1 Natural and Doppler broadening

Natural line broadening is responsible for a Lorentzian profile and can be explained by applying the Heisenberg uncertainty principle to the energy levels of the initial and final states of the transition. The life time of the spectral line can be estimated by examining the rate of spontaneous decay. Laux [25] calculates the FWHM as

$$\Delta\lambda_{nat} = \frac{\lambda_{ul}^2}{2\pi c}\left[\sum_{j<u} A_{uj} + \sum_{j<l} A_{lj}\right], \tag{2.75}$$

with u and l the upper and lower energy state of the transition. These half-width are smaller than 10^{-12} nm and can therefore be neglected.

Doppler broadening is caused by the relative motion of the radiating gas and the observer. If the velocity of the observer is neglected and the gas is assumed to have a Maxwellian velocity distribution the line profile will be gaussian. The FWHM can be calculated as

$$\Delta\lambda_{Dop} = \lambda_{ul}\sqrt{\frac{8k_B T ln\,(2)}{mc^2}}, \tag{2.76}$$

with m the mass of the emitting particle.

2.4.4.2 Impact broadening

Impact broadening is taken into account for resonance, Stark and van der Waals interactions. Regardless of the type of interaction the impact theory results in a Lorentzian profile given by

$$\phi\,(\lambda) = \frac{\Delta\lambda_{1/2}}{2\pi}\frac{1}{(\lambda - \lambda_s - \lambda_0)^2 + \left(\frac{\Delta\lambda_{1/2}}{2}\right)^2}, \tag{2.77}$$

with $\Delta\lambda_{1/2}$ the full width half maximum (FWHM) , λ_s the shift of the line and λ_0 the unperturbed wavelength of the line.

Resonance broadening is caused by interactions between particles of the same species via the dipole-dipole (C_3) interaction. According to Bates [17], these dipole interactions can facilitate excitation exchange. Perturbing particles with an allowed transition from the upper or the lower state of the transition to the energy state of the perturber can cause resonance broadening. Since the contribution of a given perturber energy state to the broadening mechanism is proportional to the density of this state, it is generally sufficient to only consider broadening caused by the ground state of the perturbers[25]. The transitions to the ground

state are called resonant transitions [20]. According to the impact theory of Griem [26] the FWHM for resonance broadening can be calculated with an expression [25] given by

$$\Delta\lambda_{res} = \frac{3e^2}{8\pi^2\epsilon_0 m_e c^2}\lambda_{ul}^2\left[\lambda_{lg}f_{gl}\sqrt{\frac{g_g}{g_l}}n_g + \lambda_{ug}f_{gu}\sqrt{\frac{g_g}{g_u}}n_g + \lambda_{ul}f_{lu}\sqrt{\frac{g_l}{g_u}}n_l\right], \tag{2.78}$$

with g_i the degeneracy of state i, the subscripts g,l and u indicating values for the ground, lower and upper states respectively,λ_{ul} the wavelength corresponding to a transition from state u to state l, f_{lu} the absorption oscillator strength for a transition from state u to state l and n_i is the perturber density in energy state i. It is important to note that Tortai [18] and Born [20] interpret Griem's theory in such a way that they only include the last term in equation 2.78 and use the total perturber density instead of n_l . It is also important to note that resonance broadening calculated from different theories results in the same expression with a different proportionality constant given by $\frac{k_r}{8}$. One of them is discussed by Tortai [18] who claims $k_r = 0.96$ is the most commonly used value (calculated by Zaidi). Chien [21] shows a longer list which includes Griem theory. In this work Griem theory is used which calculates a value of $k_r = \frac{3}{2}$ [21]. By expressing the oscillator strength in the Einstein coefficient as

$$f_{lu} = \frac{g_u}{g_l}\frac{\lambda_{ul}^2\epsilon_0 m_e c A_{ul}}{2\pi e^2}, \tag{2.79}$$

Eq 2.78 can be rewritten as

$$\Delta\lambda_{res} = \frac{\lambda_{ul}^2}{c}\left(C_{3,lg}n_g + C_{3,ug}n_g + C_{3,ul}n_l\right), \tag{2.80}$$

with

$$C_{3,ji} = \frac{3}{16\pi^3}\sqrt{\frac{g_j}{g_i}}A_{ji}\lambda_{ji}^3, \tag{2.81}$$

with j covering the upper state of the allowed transition and i covering the lower states of the allowed transitions from state j to state i.

Quadratic Stark broadening is caused by Coulomb interactions between charged particles and the radiating species. It is proportional to the square of the electric field. Tortai [18] presents an expression from Griem who writes Stark broadening as a combination of electron contributions in the impact regime and ion contributions in the quasi static regime. The FWHM is given by

$$\Delta\lambda_{Stark} = \left[1 + 1.75\alpha\left(\frac{n_e}{10^{22}}\right)^{1/4}(1 - 0.75r)\right]2\omega\left(\frac{n_e}{10^{22}}\right), \tag{2.82}$$

with r the Debye shielding parameter given by

$$r = \frac{\rho_{ion}}{\rho_D}, \tag{2.83}$$

with

$$\rho_{ion} = \left(\frac{3}{4\pi n_{ions}}\right)^{1/3} \tag{2.84}$$

and

$$\rho_D = \sqrt{\frac{\epsilon_0 k_B T}{n_e e^2}}. \tag{2.85}$$

Such a description relies on tabulated values of the ion parameter α the electron parameter ω as a function of the temperature. The expression for Stark broadening is only accurate for $0.05 < \alpha < 0.5$ and $r < 0.8$. For the species which are important in this project tabulated values of α and ω only exist for sodium. Therefore Stark broadening can generally only be taken into account if experimental values are available.

Van der Waals broadening is caused by the presence of other particles which interact with the radiating species via the van der Waals potential (C_6). The FWHM is given by Born [20] as

$$\Delta\lambda_{vdW} = \frac{\lambda_{ul}^2}{2\pi c} 8.08 \sum_j \left(\frac{8k_B T}{\pi \mu_j}\right)^{3/10} C_{6,j}^{2/5} N_j, \tag{2.86}$$

with 8.08 being a constant which for example is given by Tortai [18] as 7.566, j is a summation variable which represents all perturbing species (in practice only the buffer gas is considered), μ_j is the reduced mass of the perturber and the radiator and $C_{6,j}$ is the van der Waals constant which is given by Tortai as

$$C_6 = \frac{1}{2h\epsilon_0} e^2 \alpha \left| \left\langle r_u^2 \right\rangle - \left\langle r_l^2 \right\rangle \right|, \tag{2.87}$$

with α the polarizability of the perturbing atom in m^3 and $\left\langle r_i^2 \right\rangle$the mean square radius of the emitting atoms in state i given by

$$\left\langle r_i^2 \right\rangle = a_0^2 \frac{(n_i^*)^2}{2Z_a^2} \left\langle 5\,(n_i^*)^2 + 1 - 3l_i\,(l_i+1) \right\rangle, \tag{2.88}$$

with a_0 the Bohr radius, l_i the orbital quantum number of state i, Z_a the hydrogen equivalent charge of the atom which is equal to 1 for neutral atoms and n_i^* is the effective quantum number given by

$$(n_i^*)^2 = \frac{E_H}{E_{ion} - E_i}, \tag{2.89}$$

with E_H the ionization energy of hydrogen, E_{ion} the ionization energy of the radiating species and E_i the energy of state i. When calculating the van der Waals broadening a hydrogen like approximation was made. It is important to note that this approximation is not accurate for all atomic species.

2.4.4.3 Quasi-static broadening

In quasi static theory the spectral lines are broadened solely to the red side of the spectrum by the van der Waals interaction. Stormberg [22] uses a line shape with a Levy distribution given by

$$\begin{cases} \phi(\lambda) = \frac{\sqrt{\Delta\lambda_0}}{2(\lambda-\lambda_0)^{3/2}} exp\left(-\frac{\pi\Delta\lambda_0}{4(\lambda-\lambda_0)}\right) & for\ \lambda > \lambda_0 \\ \phi(\lambda) = 0 & for\ \lambda < \lambda_0 \end{cases}, \tag{2.90}$$

with λ_0 the unperturbed wavelength and $\Delta\lambda_0$ the characteristic wavelength of this interaction given by

$$\Delta\lambda_0 = \frac{\lambda_0^2}{2\pi c} C_6 \left(\frac{4}{3}\pi N\right)^2, \tag{2.91}$$

with C_6 the van der Waals broadening constant and N the perturber density.

2.4.4.4 General line profile

At low number densities the most important contributions for line broadening are Doppler broadening and pressure broadening from impact theory. The line profile can be calculated by convoluting a Gaussian distribution with a Lorentzian distribution. The result is a Voigt profile which can be calculated as

$$\phi(\lambda) = \frac{Re\,(Erfc(Z))}{\Delta\lambda_D\sqrt{2\pi}}, \tag{2.92}$$

with $\Delta\lambda_D$ the FWHM of the Doppler profile and $Erfc$ is the Fadeeva function. The argument Z is given by

$$Z = \frac{\lambda - \lambda_0 + i\frac{\Delta\lambda_{1/2}}{2}}{\Delta\lambda_D\sqrt{2}}, \tag{2.93}$$

with $\Delta\lambda_{1/2}$ the FWHM of the Lorentzian profile and λ_0 the unperturbed wavelength.

For lamps in the high pressure limit neither the impact theory nor the quasi static theory are sufficient to describe the line profile on their own. Stormberg [22] is followed who proposed to convolute the line profiles from both theories to obtain the final line profile. Stormberg determined an analytical solution for this line profile given by

$$\phi(\lambda) = Re\left(\frac{1}{\pi\Delta\lambda_{1/2}(1+a^2)} - i\frac{c\pi}{2}exp\left(\frac{-ab}{1+a^2}\right)A\right), \tag{2.94}$$

with A given by

$$A = Z_1^{3/2}exp\left(-\frac{ib}{1+a^2}\right)Erfc\left(\sqrt{Z_1 b}\right) - Z_2^{3/2}exp\left(\frac{ib}{1+a^2}\right)Erfc\left(\sqrt{Z_2 b}\right), \tag{2.95}$$

with a, b,c, Z_1 and Z_2 given by

$$a = \frac{\lambda - \lambda_0}{\Delta\lambda_{1/2}}, \tag{2.96}$$

$$b = \frac{\pi\Delta\lambda_0}{4\Delta\lambda_{1/2}}, \tag{2.97}$$

$$c = \frac{\sqrt{\Delta\lambda_0}}{2\pi\left(\Delta\lambda_{1/2}\right)^{3/2}}, \tag{2.98}$$

$$Z_{1,2} = \frac{-a \mp i}{1+a^2}, \tag{2.99}$$

with $\Delta\lambda_0$ the characteristic wavelength for the quasi static profile. It is important to note that Stormberg [22] defined the c constant incorrect in the main text. In the appendix he gives the correct expression. The differences with the expression in the main text are a factor π in the denominator and $\lambda - \lambda_0$ should be replaced with $\Delta\lambda_{1/2}$. Stormberg applied this line shape to describe a mercury plasma with 18 different transitions. For the 254, 365, 436 and 546 nm lines he makes a comparison between the simulated and measured lines and obtains a good agreement.

At intermediate number densities the Doppler broadening can not always be neglected. For such densities the convolution of equation 2.94 with a Gaussian profile should be calculated. In this work this convolution is approximated by

$$\phi(\lambda) = Re\left(V(\lambda) - i\frac{V(\lambda)}{L(\lambda)}\frac{c\pi}{2}exp\left(\frac{-ab}{1+a^2}\right)A\right), \tag{2.100}$$

with $V(\lambda)$ the Voigt profile and $L(\lambda)$ the Lorentzian profile. In the centre of the line the profile is equal to the Voigt profile. In the far wings this expression reduces to the expression given by Stormberg. The transition between these limits is made continuously by applying the ratio of the Voigt and the Lorentz profiles to the complex perturbation function.

2.5 Jack-Koedam theory

Elenbaas [6] and Jack and Koedam [7] estimated the conduction losses in a lamp by measuring lamps at multiple input powers. Elenbaas observed that the power in the discharge per unit length P_{dis} is lost as conduction P_{cond} and radiation P_{rad} losses per unit length. The conduction losses per unit length are given by

$$P_{cond} = -2\pi r\lambda(T)\frac{dT}{dr}. \tag{2.101}$$

Elenbaas noted that the thermal conductivity is independent of the vapour pressure and that the axis temperature is a weak function of pressure, input power and diameter. In a first approximation the conduction losses per unit length can therefore be assumed to be independent of the input power. The input power per unit length at the wall can be written as

$$P_{dis}(R) = P_{cond}(R) + P_{rad}(R), \tag{2.102}$$

with R the radius of the discharge tube. Between the centre and the boundary of the hot centre and the cooler outer mantle, r_0, all power is dissipated. From this point on only absorption will occur. The radiation losses at the wall are proportional to the radiation at r_0 as

$$P_{rad}(R) = \alpha P_{rad}(r_0), \tag{2.103}$$

with α the transmission of the outer mantle. The radiation losses can thus be written as

$$P_{rad}(R) = \alpha \left(P_{dis} - P_{cond}(r_0)\right). \tag{2.104}$$

The $P_{cond}(r_0)$ term is an estimate of the conduction losses of the hot centre to the outer mantle. The P_{dis} term can be written as

$$P_{dis} = \frac{P_{in} - P_{el}}{L_{el}}, \tag{2.105}$$

with P_{in} the input power, P_{el} the electrode losses and L_{el} the electrode separation.

Chapter 3

The model

In this chapter the solver for the one dimensional transport equations will be discussed. After that the implementation of the transport equations is covered.

3.1 Transport solver

In this work a solver is used that is derived from the Plasimo team. It is also used in the course 'Computational plasma physics' [27]. This code was converted from C++ to Matlab. The Matlab models have recently been added to extend this course.

The code uses a fluid description of the plasma and is capable of solving a generalized transport equation. In such a description different transport equations can be solved with the same code expressed in a general variable which can for example represent a density, a velocity or a temperature. This general equation is given by

$$\frac{\partial\left(\alpha_{\Phi}\Phi\right)}{\partial t}+\nabla\cdot\Gamma_{\Phi}=S_{\Phi}=S_{c}+S_{p}\Phi, \tag{3.1}$$

with Φ the generalized variable which will be called 'phi variable' from now on, α_{Φ} the time variation constant, S_{Φ} a source term which can be written as the sum of a constant source term S_c and a source term which is proportional to the phi variable S_p and Γ_{Φ} the generalized flux. The generalized flux is given by

$$\Gamma_{\Phi}=\beta_{\Phi}W_{\Phi}\Phi-\lambda_{\Phi}\nabla\Phi, \tag{3.2}$$

with β_{Φ} the velocity proportionality constant, W_{Φ} the generalized velocity and λ_{Φ} the generalized conductivity term. The velocity is defined on the boundary points while the generalized conductivity is defined on the nodal points.

For the numerical solution of equation 3.1 a discretization is required. In this case a discretization with equally sized control volumes is used. Each control volume contains a grid point at the centre of its volume. These points are called nodal points. Additionally on the outer left and outer right boundaries of the grid an extra nodal point is placed. That means that for a grid with n control volumes there will be $n+2$ nodal points. Points on the boundaries of a control volume are called boundary points. There are $n+1$ boundary points. For clarification the discretized grid is shown in figure 3.1.1.

The time independent phi equation given by

$$\nabla\cdot\left(\beta_{\Phi}W_{\Phi}\Phi-\lambda_{\Phi}\nabla\Phi\right)=S_{\Phi}=S_{c}+S_{p}\Phi, \tag{3.3}$$

can be discretized. In control volume np this discretization is given by

$$a_{np}\Phi_{np}=a_{L}\Phi_{L}+a_{R}\Phi_{R}+b, \tag{3.4}$$

with the indexes L and R referring to the control volumes at the left and the right of control volume np. The constants a_{np}, a_L,a_R and b can be expressed as a function of the parameters β_{Φ},

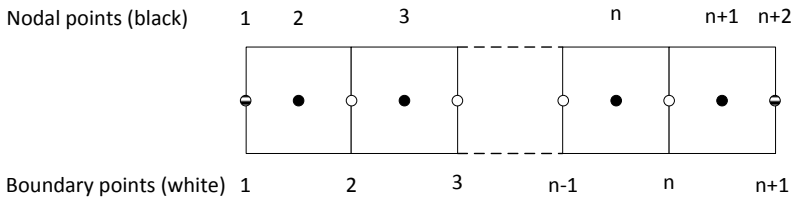

Figure 3.1.1: *Grid discretization. Nodal points are shown in black, boundary points in white.*

W_Φ, λ_Φ,S_c, S_p, V_{np}, $\delta_{i,np}$ and $A_{i,np}$. The volume of control volume np is given by V_{np}, $\delta_{i,np}$ is the distance between the nodal points i and np and $A_{i,np}$ the surface area between control volumes i and np. Boundary conditions can be applied by setting the constants a_{np},a_L,a_R and b in the most outer nodal points (1 and $n+2$). The system of $n+2$ equations can then be solved with the Tri Diagonal Matrix Algorithm (TDMA) to obtain the Φ values on every nodal point. More details about the solution procedure can be found in the syllabus [27].

3.2 Implementation

In this section is shown how the energy balance equation is translated into the generalized phi equation. Then is shown how the phi equation terms are expressed in transport constants and what literature values have been used. After that the method of calculating the interaction of the radiation field with the gas is discussed for a cylindrical geometry.

3.2.1 Transport equations

The energy balance given by

$$\nabla \cdot (-\lambda \nabla T) = \sigma_e E^2 - q_{rad}, \tag{3.5}$$

can be written as a phi equation by comparing both equations

$$\nabla \cdot (\beta_\Phi W_\Phi \Phi - \lambda_\Phi \nabla \Phi) = S_\Phi = S_c + S_p \Phi. \tag{3.6}$$

The non-zero values are Φ, λ_Φ and S_Φ which are given by

$$\Phi = T, \tag{3.7}$$

$$\lambda_\Phi = \lambda = \lambda_c + \lambda_r, \tag{3.8}$$

$$S_c = \sigma_e E^2 - q_{rad}. \tag{3.9}$$

The boundary conditions for the energy balance in a cylindrical geometry are given by

$$\left.\frac{\partial T}{\partial r}\right|_{r=0} = 0, \tag{3.10}$$

$$T(R) = T_{wall}, \tag{3.11}$$

with T_{wall} the temperature of the discharge tube wall.

3.2.2 Transport constants

The calculation of the axial velocity according to equation 2.29 requires the input of a dynamic viscosity. For the lamps investigated in this project it may be assumed that mercury dominates the transport coefficients which means that the dynamic viscosity of the gas can be approximated with the dynamic viscosity of mercury. Experimental results from Svehla [28] in the temperature range of 200-5000 K where used to make a third order polynomial fit. The fit is shown in figure

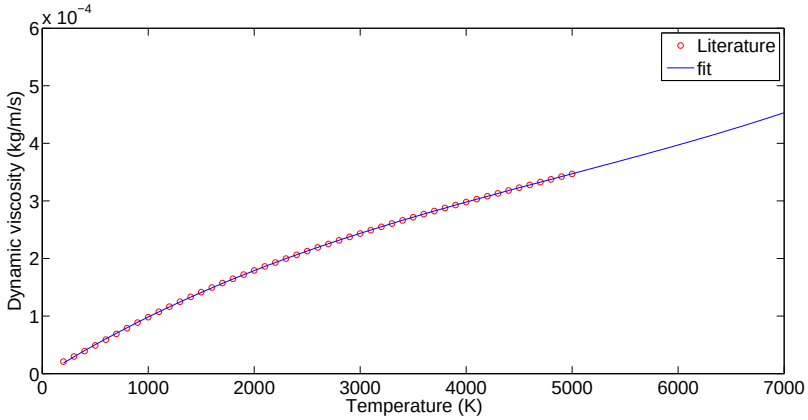

Figure 3.2.1: *Dynamic viscosity of mercury as a function of temperature. A third order polynomial fit was made.*

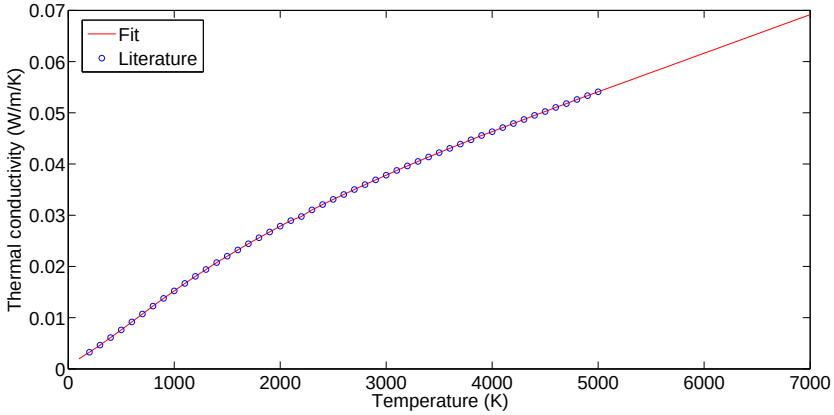

Figure 3.2.2: *Thermal conductivity as a function of temperature. An extrapolation of the literature data was made with a local cubic fitting procedure.*

3.2.1. Extrapolations up to 6000 K are required in a pure mercury lamp. For metal-halide lamps the extrapolated temperature range is lower due to lower axis temperatures.

The thermal conductivity of the gas is also approximated by the thermal conductivity of mercury. Again experimental results from Svehla [28] where used. This time matlab's one dimensional interpolation function 'interp1' was used. This function appeared to give the most stable extrapolation after 5000 K since it uses a local cubic fitting procedure. The thermal conductivity is shown in figure 3.2.2.

The calculation of the reactive conductivity is done according to the method of Butler and Brokaw [14, 15]. This calculation requires a set of independent reactions. These reactions can not be written as the sum of other reactions. An independent reaction is given by

$$\Delta H_i = \sum_{k=1}^{\mu} n_{ik} H_k. \tag{3.12}$$

The Gibbs energy as a function of temperature for all species is acquired from Philips [24]. The Gibbs energy G is related to the enthalpy by

$$\left[\frac{\partial}{\partial T}\left(\frac{G}{T}\right)_p\right] = -\frac{H}{T^2}. \tag{3.13}$$

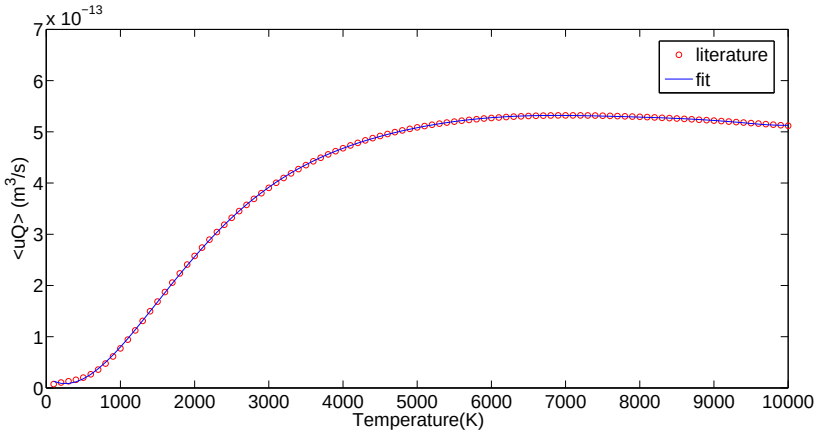

Figure 3.2.3: $\langle uQ_{e-Hg} \rangle$ *as a function of temperature. A ninth order polynomial fit function was used.*

In this work Rini's [29] description of the reactive conductivity is followed who chose to write all molecules as the sum of their atomic constituents. The stoicheometry matrix n , also required in equation 2.41, is sorted in such a way that the first elements are the independent species and the last elements are the dependent species. The matrix can then be written as

$$n = \begin{bmatrix} I & -B^T \\ B & I \end{bmatrix}, \tag{3.14}$$

with I the identity matrix. The elements B_{ij} are given by the number of dependent atoms of species j which are present in independent molecular species i. Ionized species are considered as molecular species where a deficit of electrons results in a negative value of B_{ij} when j represents the electron.

The calculation of the reactive conductivity requires an expression for the binary diffusion coefficients. With equations 2.42 till 2.46 the diffusion coefficients can be written as a function of the cross sections for neutral-neutral, neutral-charged and charged-charged interactions. These cross sections require input for the interaction radius R_i which was acquired from Philips [24] and the polarizability α. The atomic polarizablities were obtained from Patil [30]. The molecular polarizabilities were estimated as the sum of the atomic polarizabilities. This approximation is necessary since no molecular polarizabilities are available. The impact of this approximation on the reactive conductivity is small since the molecular partial pressures are low in the centre of the discharge and the diffusion coefficient is only dependent on the square root of the polarizability for neutral-charged interactions.

The electrical conductivity can also be approximated to be completely determined by mercury as

$$\sigma_e = \frac{n_e e^2}{m_e n_{Hg} \langle uQ_{e-Hg}(u) \rangle}. \tag{3.15}$$

The elastic momentum transfer cross section of mercury with electrons, $Q_{e-Hg}(u)$, was taken from the Landolt-Bornstein database who obtained their data from Buckman and Elford [31]. This cross section was multiplied with the velocity and averaged over the Maxwell-Boltzmann velocity distribution. By using the matlab interpolate function the averaged cross section was calculated till 10000 K with steps of 100 K. The resulting fit for $\langle uQ_{e-Hg} \rangle$ as a function of temperature is shown in figure 3.2.3.

3.2.3 Radiative transport

In section 2.4.3 it was shown how the radiance of a ray with an arbitrary direction vector changes due to interaction with the gas in a control volume. In this section a method is described which is

used to calculate the radiative energy transport in a cylindrical geometry. It is called raytracing. The method samples the evolution of the radiance along a set of rays in multiple directions through the discharge. This method is similar to the method used by van der Heijden [9].

Previously in section 3.2.3 was shown that the radiative flux can be calculated as

$$\Phi = I\vec{s} \cdot \vec{A} d\Omega = Id\vec{\Omega} \cdot \vec{A}, \tag{3.16}$$

with I the radiance, $\vec{A}$ the area of the control volume the ray passes through and $d\vec{\Omega}$ the solid angle covered by the ray in direction $\vec{s}$. The radiative flux passing through a small area $d\vec{A}$ on the surface of a cylindrical shell can be discretized by following the evolution of the radiance along a few rays. The direction vectors are chosen in a way that all rays originate on a boundary point and form a tangent line to a different nodal point. These tangent lines are only drawn for nodal points with a smaller radius than the radius of the boundary point. The first nodal point is not included since it represents no volume. The discretization of the radiative flux through $d\vec{A}$ for the two boundary points with the largest radii is shown in figure 3.2.4.

Azimuthal symmetry is used to reduce the number of rays required to cover the total angle in the plane. For both cases the rays can be rearranged by making use of azimuthal symmetry. The result is shown in figure 3.2.5. In this figure is shown that rays originating on the outer boundary point follow the same path as rays originating on other boundary points. The number of rays required to sample the radiance is thus reduced to the number of control volumes. The distance through a control volume $\Delta s_{j,i}$ shown in figure 3.2.7 for rays in a horizontal plane is given by

$$\begin{cases} \Delta s_{j,i} = \sqrt{R_i^2 - r_j^2} - \sqrt{R_{i-1}^2 - r_j^2} & i > j \\ \Delta s_{j,i} = 2\sqrt{R_j^2 - r_j^2} & i = j \end{cases}, \tag{3.17}$$

with j the nodal point number with the smallest radius the ray passes through and i the nodal point number indicating in what control volume this distance is calculated. R is used to represent the radius of the boundary points and r is used for the radius of the nodal points.

In a real lamp there will also be rays with a different zenith angle θ. This angle is discretized as

$$\theta_t = \frac{t_{max} - 0.5 - t + 1}{t_{max} - 0.5} \frac{\pi}{2}, \tag{3.18}$$

with $1 \leq t \leq t_{max}$ and t_{max} the total number of points used for the discretization of θ. Only the upper half of the zenith angle is considered due to the availability of a symmetry plane at $\theta = \pi/2$. The discretization was made in such a way that no ray has a zenith angle of zero. The first zenith ray has a zenith angle with a value of $\pi/2$ and covers the part of the zenith angle which lies half above and half below the symmetry plane. An image of the zenith angle points is shown in figure 3.2.6. The distance through a control volume $\Delta s_{j,i}$ can now be expressed as

$$\begin{cases} \Delta s_{j,i} = \frac{\sqrt{R_i^2 - r_j^2} - \sqrt{R_{i-1}^2 - r_j^2}}{sin(\theta)} & i > j \\ \Delta s_{j,i} = \frac{2\sqrt{R_j^2 - r_j^2}}{sin(\theta)} & i = j \end{cases}, \tag{3.19}$$

The calculation of the radiative flux also requires the calculation of the inner product between the normal of the area of the control volume and the ray. The angle in the plane $\alpha_{j,i}$ can be expressed as

$$sin\left(\alpha_{j,i}\right) = \frac{r_j}{R_i}, \tag{3.20}$$

with the indices j and i defined similar to the indices in $\Delta s_{j,i}$. In figure 3.2.7 the calculations of $\alpha_{j,i}$ and $\Delta s_{j,i}$ are clarified.

The radiative flux going through area $\vec{n}dA$ can be written as

$$d\vec{\Phi} = I\left(\vec{n} \cdot \vec{s}\right) dA d\Omega. \tag{3.21}$$

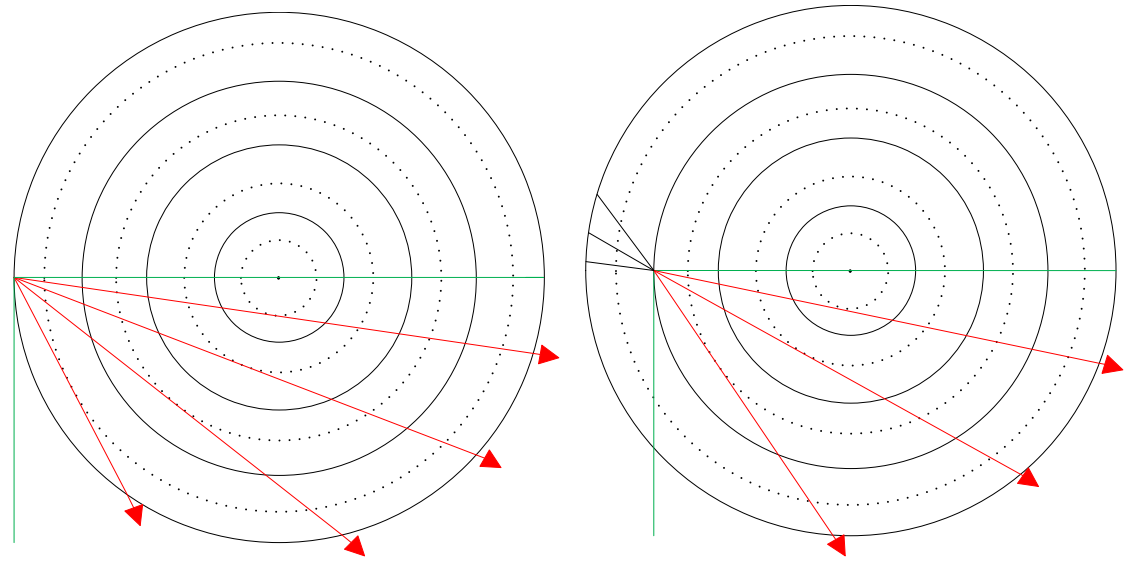

(a) (b)

Figure 3.2.4: *Discretization of the radiative flux at a point on the largest (a) and second largest (b) boundary point. The nodal points are shown in dotted lines and the boundary points are shown in full lines. A red line shows the direction vector. The direction vectors of the rays are chosen in such a way that every ray is a tangent line to a different nodal point. The black lines preceeding the red lines in figure b show were the lines used for the sampling of the second shell originated. The green lines show the sampled angle in the cylindrical plane.*

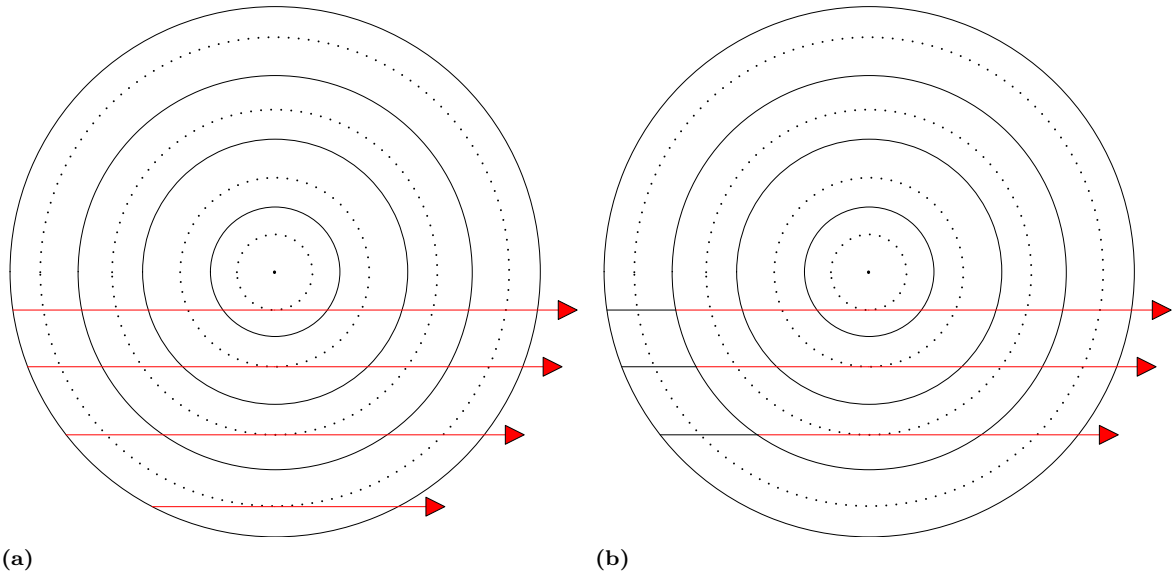

(a) (b)

Figure 3.2.5: *Rays emerging at different boundary points can all be rearranged to the same set of parallel rays. In figure a the rays emerging at the outer shell are shown and in figure b the rays that emerge at the second largest shell are shown. The rays in figure a and in figure b follow the same path. This means that the number of rays required to sample the radiance is reduced.*

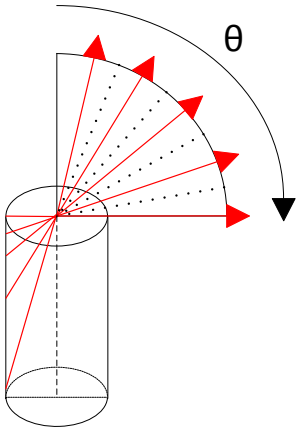

Figure 3.2.6: *The red arrows indicate how the zenith angle has been discretized. All possible rays with an angle between the adjacent black dots are represented by the red arrow. The ray at $\theta = \pi/2$ covers a zenith angle that is half above and half below the symmetry plane.*

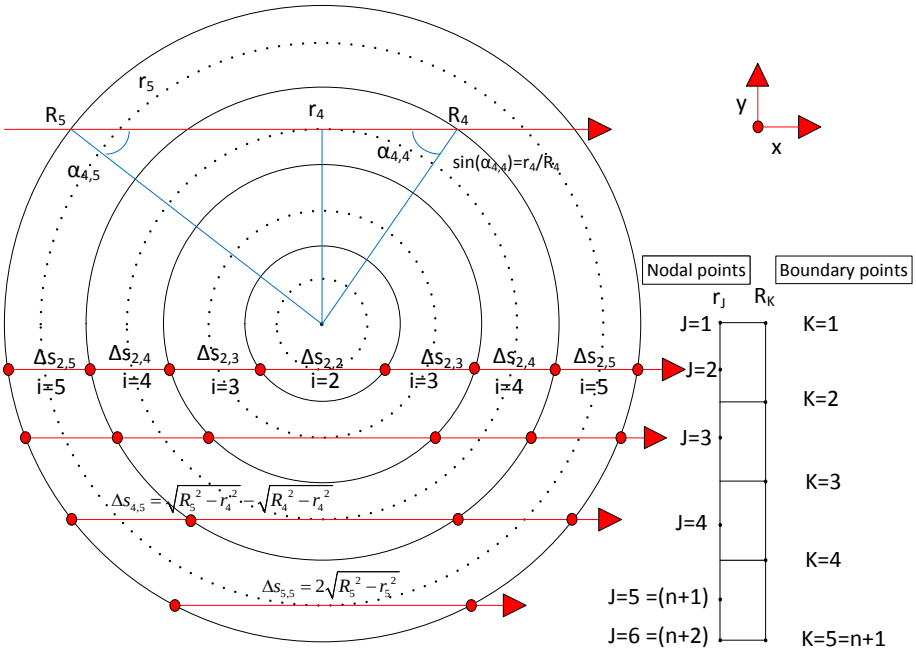

Figure 3.2.7: *The distance a ray travels between control volumes is given by the line segment between the red dots. For clarification the definition of the nodal and boundary points is included. The curved blue lines indicate the angle between the normal of the area of the control volume and the ray.*

The normal vector $\vec{n}$ and the ray's direction vector $\vec{s}$ can be expressed in cartesian coordinates as

$$\vec{n} = cos\alpha\hat{x} + sin\alpha\hat{y}, \tag{3.22}$$

$$\vec{s} = sin\theta\hat{x} + cos\theta\hat{z}. \tag{3.23}$$

The dot product is thus given by $sin\theta cos\alpha$. The solid angle can be written as

$$d\Omega = sin\theta d\theta d\alpha. \tag{3.24}$$

The radiative flux can now be rewritten as

$$d\vec{\Phi}_{j,i} = 2 \cdot 2\pi R_i \Delta z I sin^2(\theta)\, cos\alpha_{j,i} d\alpha_{j,i} d\theta d\nu. \tag{3.25}$$

This expression can be rewritten by taking the derivative of equation 3.20 to the nodal point coordinate as

$$cos\alpha_{j,i} d\alpha_{j,i} = \frac{dr_j}{R_i}. \tag{3.26}$$

The result is

$$d\vec{\Phi}_{j,i} = 2 \cdot 2\pi \Delta z I sin^2(\theta)\, dr_j d\theta_t d\nu \tag{3.27}$$

The first factor 2 is the result of the application of azimuthal symmetry since the integration from $-R_{wall}$ till R_{wall} is rewritten as the integral from 0 till R_{wall} . The contribution of ray segment i belonging to ray j can be calculated by integrating from one boundary point to the next boundary point. This contribution to the power density is given by

$$dQ_{j,i} = \int_{R_{i-1}}^{R_i} \frac{1}{V} \frac{d\vec{\Phi}_{j,i}}{dr_j} dr_j = \frac{4\pi \Delta z \Delta I_{j,i,\nu}(\theta)\, sin^2(\theta)\, (R_j - R_{j-1})\, d\theta_t d\nu}{\pi \left(R_i^2 - R_{i-1}^2\right) \Delta z}. \tag{3.28}$$

Since all boundary points have an equal spacing $R_{j-}R_{j-1}$ can be rewritten as ΔR. The contribution to the control volume with nodal point number i is given by summing all contributions from all ray's that reach this control volume. These contributions are given by

$$dQ_i = \frac{4\pi sin^2(\theta)\, \Delta R \sum_{j=2}^{j=i} \left(\Delta I_{j,i,\nu}^{first}(\theta) + \Delta I_{j,i,\nu}^{second}(\theta)\right) d\theta_t d\nu}{\pi \left(R_i^2 - R_{i-1}^2\right)}, \tag{3.29}$$

with $\Delta I_{j,i}^{first}$ the contribution from the first time that ray j passes through control volume i and $\Delta I_{j,i}^{second}$ the contribution from the second passage. The total contribution is given by integrating over the frequency and the zenith angle. The integral over the zenith angle uses a symmetry plane to write $\int_0^{\pi} dQ_i$ as $2\int_0^{\pi/2} dQ_i$. The total contribution is given by

$$Q_{rad} = \int\int \frac{d^2 Q_i}{d\theta d\nu} d\theta d\nu = \frac{\int_0^{\infty}\int_0^{\pi/2} 8\pi sin^2(\theta)\, \Delta R \sum_{j=2}^{j=i} \left(\Delta I_{j,i,\nu}^{first}(\theta) + \Delta I_{j,i,\nu}^{second}(\theta)\right) d\theta d\nu}{\pi \left(R_i^2 - R_{i-1}^2\right)} \approx \frac{\sum_{t=1}^{t_{max}} \sum_{\nu=1}^{\nu_{max}} 8\pi sin^2(\theta_t)\, \Delta R \sum_{j=2}^{j=i} \left(\Delta I_{j,i,\nu,t}^{first} + \Delta I_{j,i,\nu,t}^{second}\right)}{\pi \left(R_i^2 - R_{i-1}^2\right)}. \tag{3.30}$$

3.3 Emission

In this section the calculation of the emission of atomic radiation and electron-mercury Bremsstrahlung is discussed. The atomic radiation is calculated as

$$j = \frac{h\nu}{4\pi} A n_u \phi(\nu), \tag{3.31}$$

with the density of excited particles given by

$$n_u = n_{tot} \frac{g_u}{Z} exp\left(-\frac{E_u}{k_B T}\right). \tag{3.32}$$

The spectroscopic constants, ν, g_u, E_u and A, are taken from the NIST database [39] or the database from the university of Hannover [40]. The database from the university of Hannover is only used when the parameters are unavailable on the NIST database. The partition function Z is determined as a function of temperature via the NIST database.

The line profile requires a discretization of the spectral grid. For every line a spectral interval is chosen manually. This interval is divided in equal blocks. The centre of each block contains the spectral position of that block. This grid is similar to the discretization of the spatial positions shown in figure 3.1.1. The nodal points are the equivalent of the spectral position and the difference between the boundary points determines the $\Delta\nu$ corresponding to that spectral position. Some lines have an increased density of spectral points near the unperturbed wavelength to make sure all details of the line centre are correctly taken into account. When the spectral positions of multiple lines overlap all equal spectral positions are removed. For the remaining spectral points the new spectral boundary points are calculated. The spectral positions are recalculated to make sure that these points are placed in the centre of the new blocks. The emission of any line is calculated on all spectral points of all lines which overlap either directly or indirectly.

The emission of electron-mercury Bremsstrahlung is calculated according to Lawler [**?**, **?**]. He expressed the emission as

$$j_{Bremm} = K_{\nu,T} I_{BB} n_e n_{Hg}, \tag{3.33}$$

with $K_{\nu,T}$ a proportionality constant tabulated as a function of frequency and temperature, I_{BB} the blackbody function, n_e the electron density and n_{Hg} the mercury density. The Bremsstrahlung is calculated analytically. This radiation is optically thin which means only a small error is made when Bremsstrahlung is not available for absorption.

Chapter 4

Modeling results

In this chapter the simulation results for the single salt lamps are shown. First the model calibration is considered. After that the results for the single salt lamps are shown. A comparison between the simulated and measured spectra and the predicted and experimentally determined energy balances is made in chapter 7.

The total amount of mercury and metal halides in the lamp is known. The lamps are saturated with salts. This means that the coldspot temperature determines what amount of metal halides is actually available in the gas phase. The coldspot temperature is unknown for all lamps. Therefore the density profiles can not be calculated accurately and will be estimated.

The reactive conductivity is currently not included for the simulations which contain iodide species. Adding the reactive conductivity is expected to result in a slightly lower axis temperature. The effect will be small since the diffusion coefficients are relatively low due to the high mercury pressure.

It is important to note that the mercury simulation was calibrated for the visible radiation only. The ultraviolet radiation in mercury lamps is crucial for the radiative energy transport and thus has a significant impact on the energy balance. The sodium iodide simulation was only calibrated for the self reversal width of the sodium D-lines. The thallium iodide and indium iodide simulations are not calibrated at all. As a consequence the results for the thallium iodide and indium iodide simulations are less accurate than for the mercury and sodium iodide simulations.

4.1 Model verification

In this section the results of the simulations will be shown for the 250 W mercury lamp and the 70 W and 400 W SON lamps. All of these lamps can be considered one dimensional. A SON lamp contains both mercury and sodium but no iodide.

4.1.1 250 W Mercury lamp

The 250 W mercury lamp's discharge tube has a radius of 7.75 mm and an electrode separation of 58 mm. The heigth to diameter ratio is approximately four. The lamp can therefore be considered one dimensional. The mercury pressure is around 5 bar.

This lamp was measured at Philips OCM. The calibrated visible spectrum was used to determine the broadening constants of the 404, 436 and 546 nm lines. The broadening constants of these self reversed lines[1] were chosen such that the energy of the simulated visible lines matched the measured energy. The broadening constants of the resonant 185 and 254 nm lines were tuned to obtain the correct energy in the 577 and 579 nm lines. Since these lines are optically thin and therefore not self reversed the line shape has no influence on the energy in these transitions. In

[1] Self reversed lines have a lower radiative output in the line centre than in the line wings because part of the radiation from the line centre is absorbed in the outer mantle.

LTE at a given mercury pressure the energy in these lines is solely determined by the temperature distribution. The shape of the resonant lines has the largest influence on the temperature distribution therefore their broadening constants are adjusted. As an additional restriction the shape of the 254 nm line adjusted to make sure that is resembles the shape measured by Stormberg [43].

The simulated mercury side-on spectra for the ray going through the centre control volume are shown in figures 4.1.1-4.1.3 for several atomic transitions. The resonant lines have a red wing which is severely broadened by van der Waals interactions. The radiative output from the left wing and the line centre of the 185 nm line are negligible. The radiation from these wavelengths follows the blackbody radiance almost perfectly due to the high optical depth. As indicated in eq 2.57 the low temperature near the wall and the small wavelengths decrease the blackbody radiance which increases the optical depth. The evolution of two distinct spectral points for the 185 nm line for the ray going through the centre control volume are shown in figure 4.1.4. The spectral area close to the line centre is able to follow the radiance of a blackbody. Just beyond the centre of the discharge a point is reached where the radiance exceeds the radiance of a blackbody. Along the remaining path of the ray more radiation is absorbed than emitted. Further away from the line centre the optical depth is smaller because the line profile has decreased. The radiance therefore increases slowly. The point where absorption is dominant is reached close to the wall. For resonant transitions in this lamp the optical depth increases at positions closer to the wall because the temperature decreases. As a result the mercury density increases. Therefore close to the wall the radiance decreases most for wavelengths far away from the line centre. The reasoning is as follows:

$$\tau \sim \phi(\lambda, T)\, n_{Hg} \frac{exp\left(\frac{hc}{\lambda k_B T}\right) - 1}{exp\left(\frac{E_u}{k_B T}\right)}, \tag{4.1}$$

$$\phi(\lambda, T) \sim C_6 n_{Hg}^2 \quad \lambda \gg \lambda_0, \tag{4.2}$$

$$n_{Hg} \sim \frac{p_{Hg}}{T}, \tag{4.3}$$

$$\tau \sim \frac{p_{Hg}^3}{T^3} \frac{exp\left(\frac{hc}{\lambda k_B T}\right) - 1}{exp\left(\frac{E_u}{k_B T}\right)}. \tag{4.4}$$

At lower temperatures for a resonant transition the ratio of the exponents is equal to one. For this lamp the convection limit was assumed which means the elemental pressure is constant through the entire lamp. For mercury the elemental density is almost equal to the atomic mercury density and can be assumed to be constant as well. This means the optical depth increases with decreasing temperature.

For the spectral part closer to the line centre the broadening calculated from impact theory is dominant. For a transition where resonance broadening is most important the proportionality is given by

$$\phi(\lambda, T) \sim C_3 n_{Hg} exp\left(-\frac{E_l}{k_B T}\right) \quad \lambda \gg \Delta\lambda_{1/2} \tag{4.5}$$

$$\tau \sim \frac{p_{Hg}^2}{T^2} \frac{exp\left(\frac{hc}{\lambda k_B T}\right) - 1}{exp\left(\frac{E_u + E_l}{k_B T}\right)}, \tag{4.6}$$

this shows that for resonant transitions the optical depth increases towards the wall since $E_l = 0\,\mathrm{J}$. For non-resonant transitions the optical depth decreases since $E_u + E_l > \frac{hc}{\lambda}$. Similar expressions can be derived for Stark and van der Waals broadening for impact theory. The optical depth for Stark broadening always decreases towards the wall because of the decreasing electron density and for van der Waals broadening the optical depth increases because of the increasing perturber density.

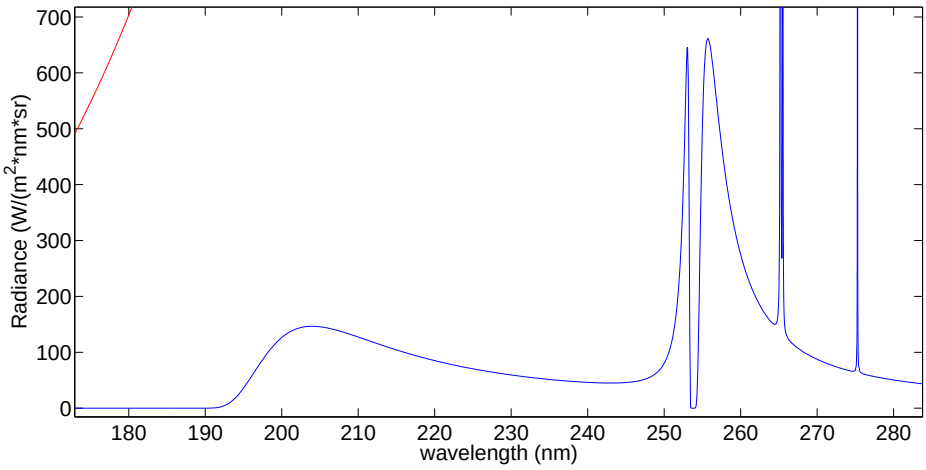

Figure 4.1.1: *The 185 and 254 nm resonant mercury lines along a ray passing through the centre of the discharge. The 185 nm line is completely absorbed in its left wing and in its line centre. Its right wing survives because the maximum radiance, equal to the radiance of a blackbody source with the axis temperature shown in red in the upper left corner, is much higher for these wavelengths. The 254 nm line is self reversed and has also got a significantly broadened right wing.*

Close to the wall LTE will be no longer valid. At these positions the radiance of a blackbody at the gas temperature will not describe the ratio of emission to absorption accurately. A more accurate value could be obtained by considering a two temperature system of heavy particles and electrons. The density of excited states is determined by electron impact. The distribution of the excited states can be approximated with a Boltzmann distribution with the electron temperature. The equation of radiative transport can then be approximated to be a function of the radiance of a blackbody at the electron temperature. In the centre of the discharge such a calculation will result in similar values for the emission and the absorption. In the outer mantle of the discharge the amount of radiation which is absorbed is currently overestimated for lines with a high optical depth. For lines with a low optical depth the impact of a two temperature calculation will be small since these lines do not have a significant interaction with the gas in the outer mantle. The difference between the evolution of the radiance for an optical thin line and an optical thick line is shown in figures 4.1.5 and 4.1.6. The isosurfaces of the radiance of the optical thick line show significant curvature near the wall which indicates strong absorption. The isosurfaces of the radiance of the optical thin line are straight lines near the wall. This means that in the outer part of the discharge there is no interaction between the radiation and the gas.

The temperature distribution and the cumulative energy for radiation, conduction and ohmic heating are shown in figure 4.1.7. The shape of the temperature distribution is similar to the profiles shown by Elenbaas [6] for different mercury discharges. The calculated axis temperature is 5800 W. A wall temperature of 900 K was taken from Stormberg and Schäfer [43]. The cumulative energy transported as radiation decreases from a certain radius. This radius is called r_0. At this radius more radiation is absorbed than emitted. The absorption of radiation reaches a maximum and then slightly decreases towards the wall. The maximum in the amount of radiation that is absorbed for a given wavelength occurs at the position where the gradient with respect to the blackbody curve is largest. Beyond this radius the absorption of radiation decreases because the radiance in the line centre has already been decreased significantly. The smaller gradient of the blackbody curve thus limits the absorption. In the most outer part of the discharge there is a sudden increase of absorption. This is related to the low number of grid points used to cover the strong temperature gradient near the wall. Such a sudden increase is unphysical and can be removed by adding more grid points near the wall. Between the centre of the discharge and r_0

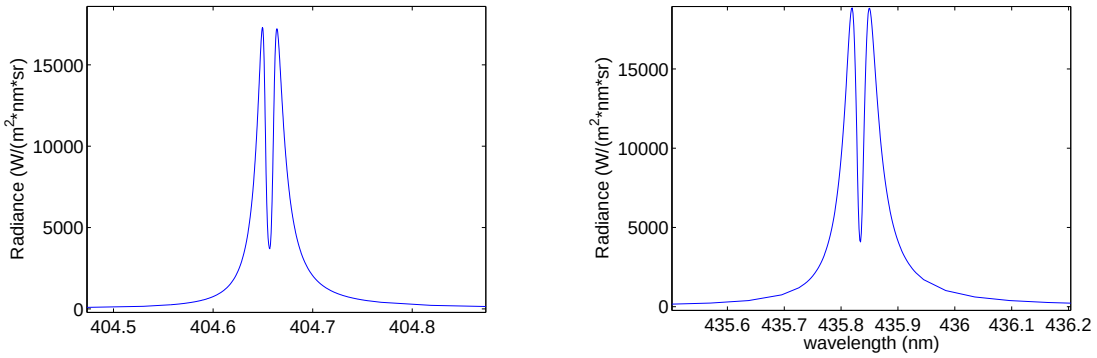

(a) **(b)**

Figure 4.1.2: *The self reversed 404 and 436 nm mercury lines. The broadening constants of both lines were adjusted to obtain the correct energy in the lines.*

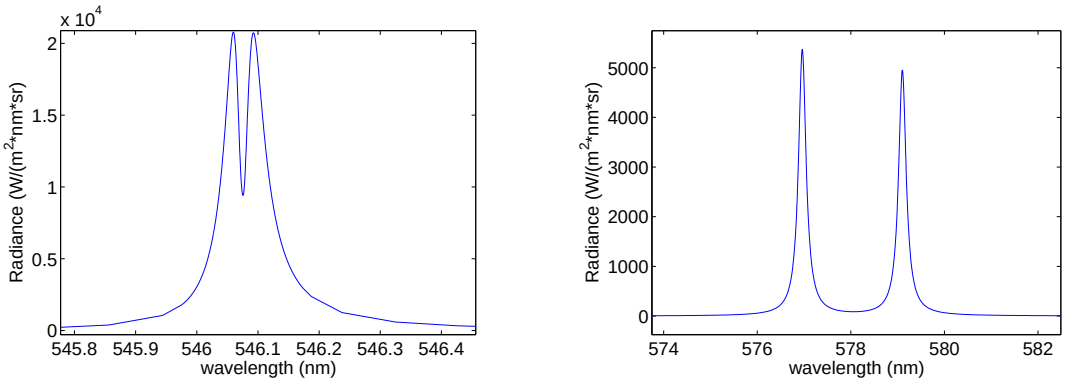

(a) **(b)**

Figure 4.1.3: *a) The self reversed 546 nm line is shown. Its broadening constants were chosen such that the simulated energy matches the measured energy in the line. b) The optically thin 577 and 579 nm lines. The broadening constants of the resonant lines were matched to obtain the correct energy output in the 577 and 579 nm lines.*

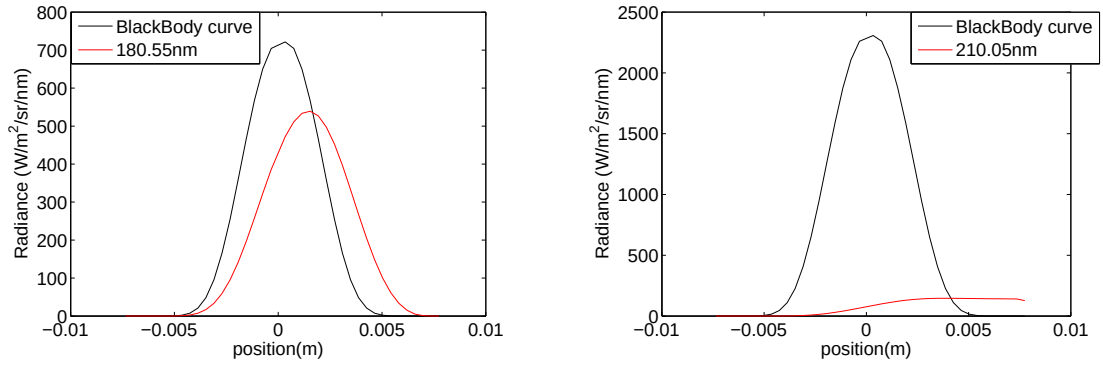

(a) **(b)**

Figure 4.1.4: *a) The evolution along a ray passing through the centre of the discharge for a wavelength close to the unperturbed wavelength. The optical depth is high enough to follow the blackbody curve. At a certain position when the ray is moving away from the centre of the discharge the radiance of the ray is above the radiance of the blackbody curve. From this point on more radiation is absorbed than emitted. b) The evolution along a ray passing through the centre of the discharge for a wavelength far from the unperturbed wavelength. The optical depth is not high enough to follow the blackbody curve. The position where the radiance of the ray is above the radiance of the blackbody curve is reached at a point close to the wall. From this position on the optical depth increases due to the strong temperature gradients.*

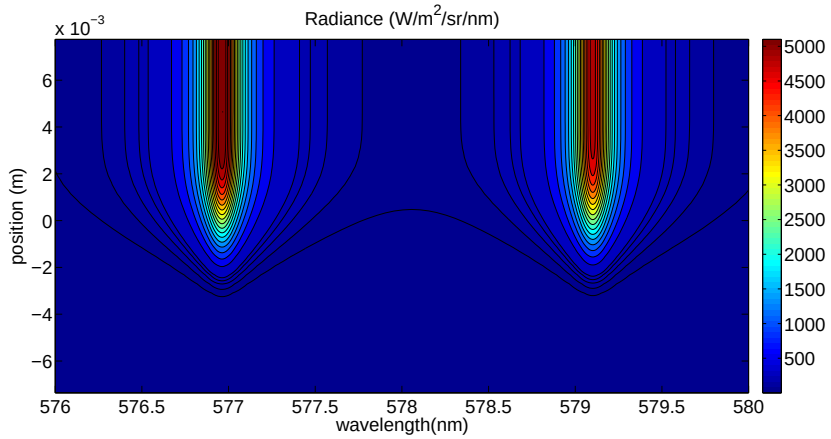

Figure 4.1.5: *The evolution of the optical thin 577 and 579 nm mercury lines through the discharge. The radiance of these lines increases untill a certain point where the optical depth is to low to interact with the gas.*

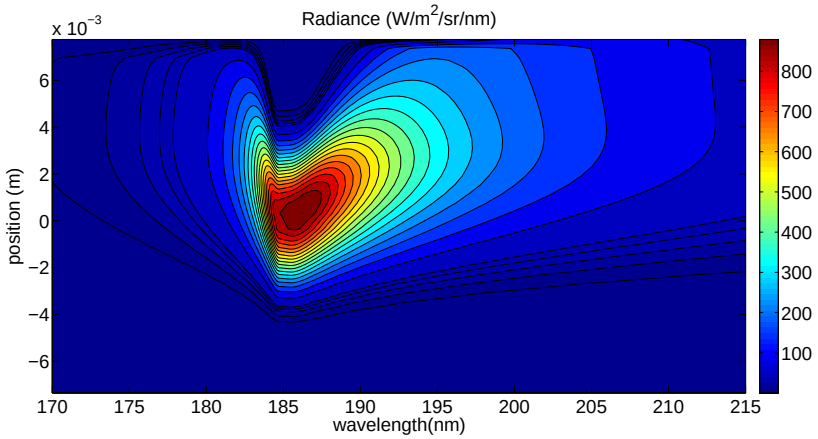

Figure 4.1.6: *The evolution of the 185 nm line through the discharge. The contour curves are not symmetrical due to strong van der Waals broadening. The strong temperature gradient near the wall causes significant reabsorption of radiation.*

	Energy (W)
UV	63.0
VIS	28.6
IR	37.0
Non-radiative losses	95.9
Electrodes	25.0
Total	249.6

Table 4.1.1: *The output energy balance of the 250 W mercury lamp. The ultraviolet is responsible for a large part of the radiation. The infrared radiation is almost completely caused by Bremmstrahlung. The only included atomic infrared transition is the 1014 nm line. Other infrared lines were not included because no transition probability was available. The contribution of the remaining infrared lines is in the order of the energy in the 1014 nm line as is indicated in table 6.1.2. This means that only a small error is made by neglecting these lines.*

almost all ohmic heating takes place. For radii larger than r_0 the radiation losses are partially converted to conduction losses.

The thermal conductivity as a function of the radius is shown in figure 4.1.8. The thermal conductivity is dominated by collisional transport. The reactive conductivity in the centre of the discharge due to ionization reactions is small since mercury has a high ionization potential. An output energy balance is shown in table 4.1.1. A comparison can be made with an energy balance of a 400 W mercury lamp measured by Jack and Koedam [7]. Although the dimensions of this lamp are not similar the normalized energy balance should still exhibit the same trends. The ultraviolet output is in the order of 25 %. This value is relatively large in comparison to the 18 % determined by Jack and Koedam. The visible contribution is approximately 11 % where Jack and Koedam determined 15 %. The infrared is in both cases approximately 15 %. Jack and Koedam estimated the non-radiative losses with 45 % while in this simulation these losses are around 38 %. The electrode losses are estimated with 10 % while Jack and Koedam determined 7.5 %. Since both lamps are not completely the same these differences are acceptable.

The visible spectrum of this lamp is measured at Philips for multiple input powers ranging from 190 W to 310 W. The broadening constants of the simulation model were calibrated by matching the energy in the simulated visible lines with the energy in the measured lines at an input power of 250 W. With these constants the energy in the visible lines was predicted for the other input powers. The results are shown in table 4.1.2. The energy of the 404, 407 and the 435 nm lines are

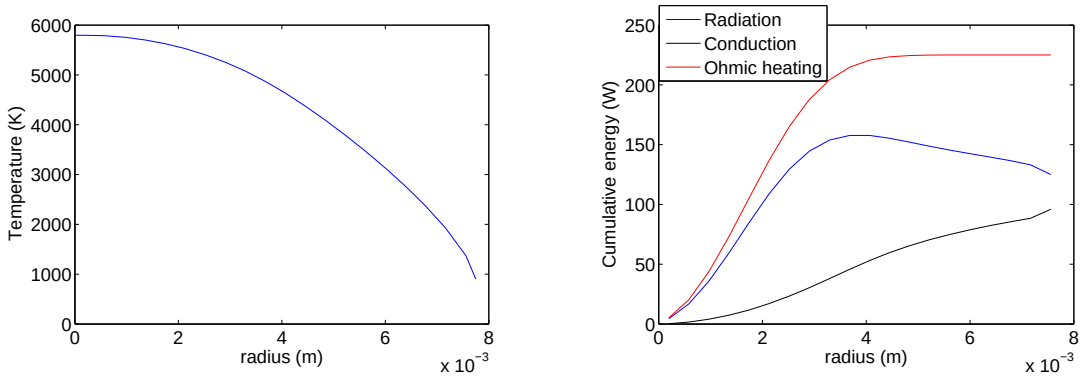

(a) **(b)**

Figure 4.1.7: *a) The calculated temperature profile for the 250 W Hg lamp. The axis temperature is 5800 K and the wall temperature is 900 K. b) The cumulative energy for radiation and conduction losses and ohmic heating. The cumulative radiation losses are decreasing from a certain radius on. This means that more radiation is absorbed than emitted. In the most outer point of the discharge the absorption of radiation increases again. This sudden increase is unphysical and can be removed by using more grid points near the wall.*

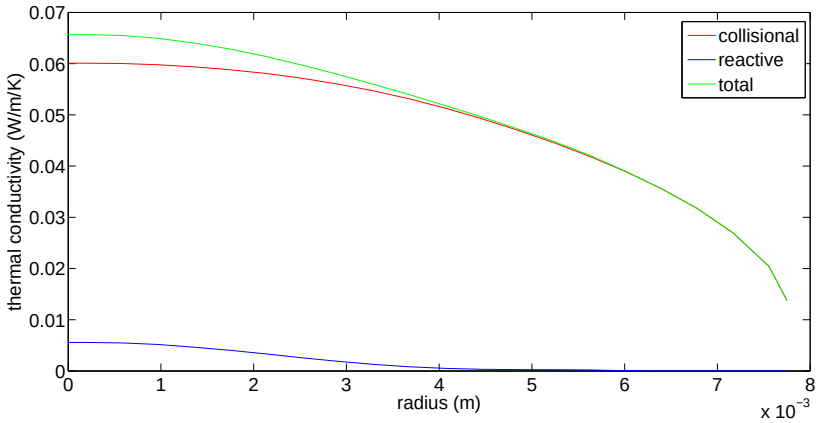

Figure 4.1.8: *The thermal conductivity of the 250 W mercury lamp. The reactive conductivity makes a small contribution to the total thermal conductivity. In the centre of the discharge the chemical transport of energy is caused by* the species involved in the ionization reaction: Hg, Hg^+ and e^-.

	190 W	210 W	230 W	250 W	270 W	290 W	310 W
M: 404+407 nm (W)	3.00	3.14	3.75	3.96	4.31	4.45	4.97
S: 404+407 nm (W)	2.90	3.27	3.64	4.02	4.39	4.76	5.14
M: 435 nm (W)	5.13	5.35	6.41	6.83	7.38	7.65	8.52
S: 435 nm (W)	4.91	5.50	6.09	6.69	7.28	7.88	8.47
M: 546 nm (W)	6.17	6.44	7.31	7.60	7.92	8.08	8.56
S: 546 nm (W)	5.74	6.35	6.97	7.60	8.20	8.81	9.41
M: 577+579 nm (W)	6.28	6.59	8.22	8.79	9.61	9.92	11.35
S: 577+579 nm (W)	5.68	6.66	7.64	8.66	9.71	10.78	11.87
M: total (W)	20.58	21.52	25.69	27.19	29.22	30.09	33.40
S: total (W)	19.23	21.78	24.35	26.96	29.58	32.23	34.89

Table 4.1.2: *The results for the measurements and the simulations of the powerscan of the 250 W Hg lamp. In the first column an M indicates the measured energy and an S indicates the energy acquired from the simulation. The output of the visible lines in the simulations were matched with the measured output for the 250 W measurement. With the same broadening constants the predictions were made for the other powers. The total energy error is smaller than* 1.5 W for every input power.

predicted accurately for all input powers. The differences between the simulated and measured energy for the 546 nm line are approximately 0.8 W for the highest input powers. For the 577 and 579 nm lines the the predictions are also less accurate. Since these two lines are not self reversed the energy difference between measurement and simulation indicates that the predicted temperature profile is not completely correct. The temperature profile is strongly dependent on the broadening constants of the 185 and 254 nm lines. These differences indicate that a calibrated ultraviolet spectrum is required to determine the broadening of the resonant mercury lines more accurately. Despite the lack of knowledge of the exact shape of the resonant lines the energy in the visible lines was predicted within 1.5 W for various input powers.

4.1.2 SON lamp

In this section the results for the SON 70 W and SON 400 W lamp simulations are shown. These lamps can be considered one dimensional. The radius of the SON 70 W discharge tube is 1.9 mm and the electrode separation is 40 mm. The radius of the SON 400 W discharge tube is 3.75 mm and the electrode separation is 82 mm. Both lamps have a ratio of the electrode separation to the radius which is more than 20. The SON 70 W lamp is used to calibrate the self reversal width of the sodium D-lines.

The simulated and measured spectrum of the SON 70 W lamp are shown in figure 4.1.9. The setup was realigned but not recalibrated. The measured spectrum is thus not completely correct. The sum of the spectral energy and the conduction losses can not account for 12.5 W. Therefore the broadening constants for the sodium D-lines were adjusted to match the self reversal width of the measured spectrum. The sodium pressure in the discharge was estimated by using an empirical relation from De Groot and van Vliet [11] given by

$$p_{Na} = \frac{2.7 \pm 0.5}{\sqrt{R}} 2\Delta\lambda_B, \tag{4.7}$$

with P_{Na} the sodium pressure in kPa, R the radius of the discharge tube in mm and $\Delta\lambda_B$ the width between the blue self reversal maximum and the line centre in nm. The sodium pressure is estimated as (9.8 ± 1.8) kPa. The mercury pressure was adjusted to obtain agreement between the measured voltage of 75.1 V and the simulated voltage. The required mercury pressure is 1.3 bar. The luminous efficacy η is a measure of the efficiency of the production of useful radiation. It can

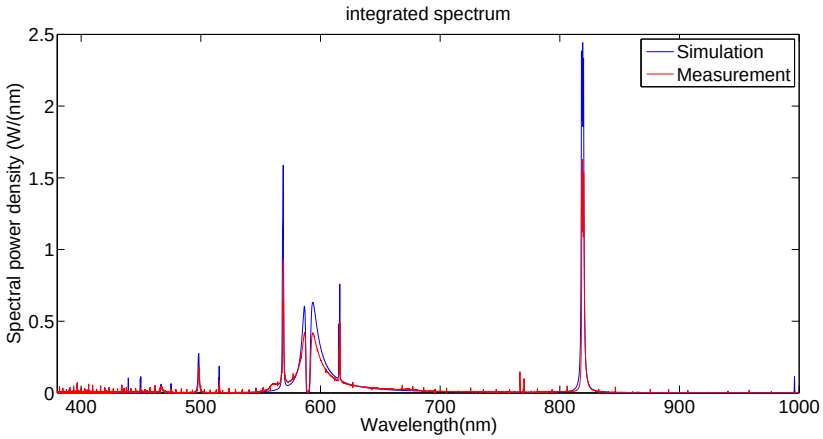

Figure 4.1.9: *The simulated and measured SON 70W spectra. The measured spectrum can not be used as an absolute comparison because the setup was realigned but not recalibrated. The broadening constants of the sodium D-lines were adjusted to obtain the same self reversal width as in the measurement.*

be calculated as

$$\eta = \frac{683.002 \int_0^\infty P_{rad}(\lambda) V(\lambda) d\lambda}{P_{in}}, \tag{4.8}$$

with $P_{rad}(\lambda)$ the spectral power density, $V(\lambda)$ the eye sensitivity curve and P_{in} the input power. With the estimated pressures the luminous efficacy of the simulated lamp is 108 lumens/W. According to De Groot and Van Vliet [11] the luminous efficacy is around 90 lumens/W. The luminous efficacy determined from the measured spectrum is 86 lumens/W which indicates that the realignment of the setup hardly changed the visible calibration.

The simulated temperature profile and cumulative integrated source terms are shown in figure 4.1.10. The thermal conductivity is shown in figure 4.1.11. The combination of the large amount of radiation from the sodium lines and the increased reactive conductivity in the centre of the discharge due to ionization of sodium decreases the temperature profile drastically in comparison with the pure mercury lamp. The calculated axis temperature is 4600 K and a wall temperature of 1500 K was assumed similar to the SON 400 W lamp described by de Groot and van Vliet [11]. The cumulative radiated energy reaches a maximum at approximately 2/3 of the tube radius. From this point on about 7 W of radiation is absorbed.

The same broadening constants were used to predict the spectrum of the SON 400 W lamp. The spectrum is shown in figure 4.1.12. By using the same broadening constants as for the SON 70 W lamp the self reversal width for the simulated SON 400 W sodium D-lines is also in agreement with the measured width. The simulated efficacy is 158 lumens/W. According to de Groot and van Vliet [11] the efficacy of this lamp is 120 lumens/W. The output of most of the sodium lines is overestimated similar to the energy in the SON 70 W simulation. A better calibration of the sodium broadening constants of the SON 70 W model will therefore also improve the SON 400 W model. Including reflections from the discharge tube will specifically reduce the radiative output of the self reversal maxima [24]. These are currently slightly overestimated.

The simulated temperature profile is similar to the SON 70 W lamp. The axis temperature is 4700 K and the wall temperature is set to 1500 K. According to de Groot and van Vliet [11] the axis temperature for this lamp should be around 4000 K. The overestimated axis temperature explains the overestimated luminous efficacy. Since the axis temperature of the 400 W SON lamp is overestimated the axis temperature of the 70 W lamp is most likely overestimated as well. The mercury pressure in the 70 W SON lamp may be overestimated too since the potential between the electrodes was used as a fitting parameter. The potential is dependent on the temperature in the centre of the discharge.

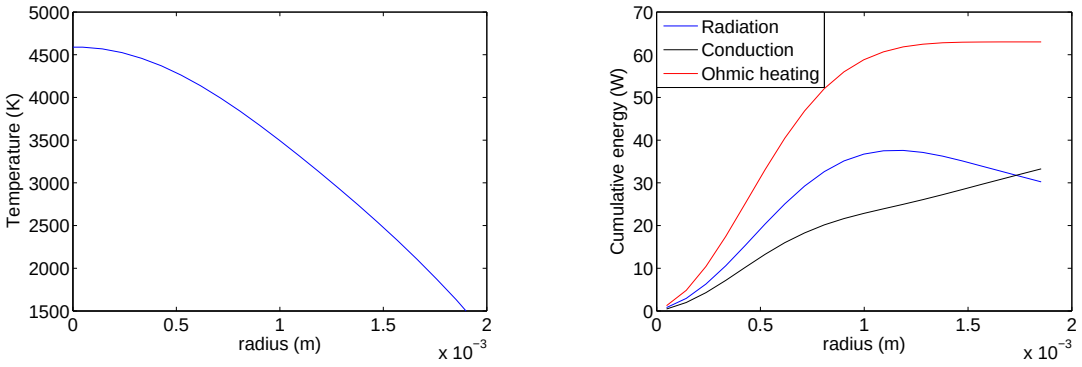

(a) **(b)**

Figure 4.1.10: *a) The temperature profile of the SON 70 W simulation. The axis temperature is around 4600 K and the wall temperature is set to 1500 K. b) The energy dissipated as ohmic heating and radiation or conduction losses. From approximately 2/3 of the radius of the discharge tube the absorption of radiation is more dominant than emission.*

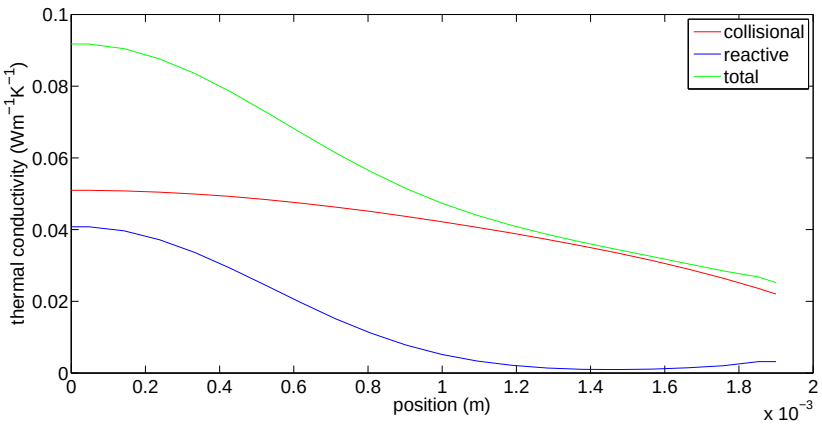

Figure 4.1.11: *The thermal conductivity of the SON 70 W lamp. In the centre of the discharge the reactive conductivity is responsible for almost half of the total thermal conductivity due to ionization reactions. Close to the wall the reactive conductivity increases again due to the formation of molecular sodium.*

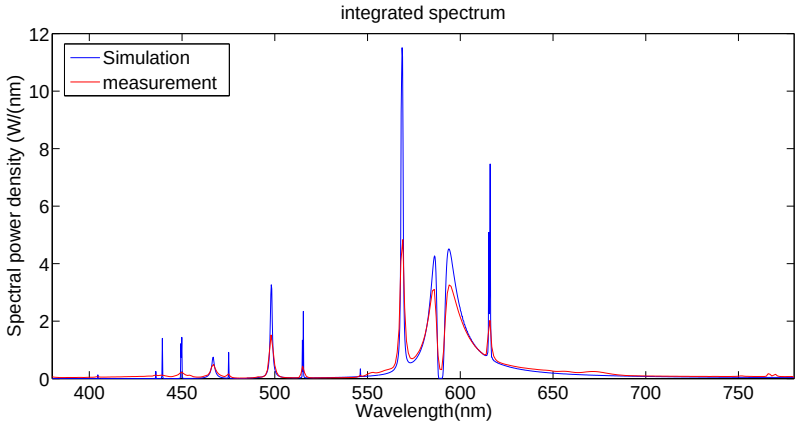

Figure 4.1.12: *The measured and simulated spectra of the SON 400 W lamp. The same self reversal width for the simulated sodium D-lines is obtained as in the measurement. Similar to the SON 70 W lamp the output of most lines is overestimated.*

	P_{UV} (W)	(%)	P_{vis} (W)	(%)	P_{IR} (W)	(%)	$P_{non\ rad}$ at R (W)	(%)
SON 70 W sim	0.6	0.9	16.6	24	13.1	19	33.2	47
SON 400 W sim	0.5	0.1	139	35	105	26	116	29
SON 400 W [11]	1	0.3	123	31	84	21	169	42
400 W Hg+Na [7]	2	0.5	118	30	80	20	176	44

Table 4.1.3: *The energy balance for the simulated SON 70 W and SON 400 W. As a reference the energy balance for the SON 400 W determined by de Groot and van Vliet [11] is included as well. Their IR losses only cover 780-2500 nm and also include thermal radiation from the electrodes and discharge tube. The total power in these processes was estimated as 16 W and substracted from the 100 W which was measured. The sodium lamp measured by Jack and Koedam [7] has a radius of 23 mm and is 220 mm long which means the height to radius ratio is smaller for that lamp.*

An output energy balance for the simulated SON 70 W and SON 400 W lamps and the measured SON 400 W [11] and 400 W sodium lamp [7] is shown in table 4.1.3. The energy balance also shows that the predicted radiative output for the SON 400 W lamp is slightly overestimated. The energy balance of the 400 W Hg+Na lamp is similar to the SON 400 W lamp. The non-radiative losses of the 400 W Hg+Na lamp should therefore be representative for the SON 400 W lamp. In the simulation this contribution is currently strongly underestimated. The non-radiative losses at R is the sum of the energy which is directly transported by conduction and the energy which is absorbed. In the 400 W SON lamp the energy which is directly transported by conduction is 62 W. For the 400 W Hg+Na lamp these losses are 66 W according to Jack and Koedam [7] which is in agreement with the simulation. The remaining 110 W in their lamp is the result of absorption of radiation. In the simulation only 44 W was absorbed in the outer mantle. This indicates that the broadening constants of the sodium D-lines should be reconsidered.

The energy balance of the SON 70 W lamp deviates from the SON 400 W lamp because of the significant increase of the non radiative losses. For the SON 70 W lamp the ratio of the surface area to the volume of the tube is larger which enhances conduction losses. The radiated energy is therefore lower.

4.2 Hg

The pure mercury lamp contains 8.5 mg of mercury. The mercury pressure is estimated from the ideal gas law as

$$p_{Hg} = \frac{M_{Hg}}{m_{Hg}} \frac{k_B T_{eff}}{V}, \tag{4.9}$$

with M_{Hg} the mercury dosage, m_{Hg} the mass of one mercury atom, V the volume of the discharge tube and T_{eff} the effective temperature defined by

$$T_{eff} = \frac{V}{\int_0^R \frac{dV}{T}}. \tag{4.10}$$

For a mercury discharge the effective temperature is estimated with 2500 K. The resulting mercury pressure is approximately 30 bar. The simulated temperature profile and cumulative integrated source terms for this discharge are shown in figure 4.2.1. The temperature profile is more flat in the centre of the discharge in comparison with the 250 W mercury lamp. The higher pressure in the 70 W lamp increases the radiation losses while the conduction losses are independent of pressure. As a result the radiative heating of the area close to the centre of the discharge is stronger and the temperature profile is flattened. The predicted axis temperature is 5800 K. The simulated potential between the electrodes is 63.3 V. A potential of 89.8 V was measured. From these values it is concluded that either the predicted temperature profile is too high which results in an overestimated electron density or the mercury pressure is slightly underestimated.

The calculated integrated spectrum is shown in figure 4.2.2. The increase of mercury pressure from 5 bar for the 250 W lamp to 30 bar for the 70 W lamp strongly increases the van der Waals broadening of the red wings of the resonance lines. The self reversal maximum of the red wing of the 185 nm line moved from 207 nm for the 250 W lamp to 226 nm for this 70 W lamp. The far wing of these resonance lines even extends somewhat into the visible part of the spectrum. Such strong broadening is not observed in measured spectra which indicates that the van der Waals broadening constant is overestimated. In comparison with the recommended values from Hartel et al [44] the broadening constants for van der Waals broadening were already reduced by more than an order of magnitude. The exact shape of the resonant mercury lines at high pressures is unknown. For example Hartel et al [44] summarize multiple values for the van der Waals broadening constant of the 254 nm line. The highest value is about 15 times larger than the lowest value. For the resonance broadening constant of this line the highest reported value is 35 times larger than the lowest value which shows how difficult it is to determine these constants.

4.3 Hg+NaI

The sodium iodide lamp contains 8.5 mg of mercury and 5 mg of sodium iodine. Due to the lower temperature in the sodium discharge the mercury pressure has decreased. The mercury pressure is estimated to be 25 bar which corresponds to an effective temperature of around 2100 K. The coldspot temperature is estimated to be 1200 K. The convection limit is used to calculate the density profile. At a temperature of 4000 K the sodium pressure is 2.6 kPa which is about a quarter of the sodium pressure in the SON lamps.

The simulated temperature profile and cumulative integrated source terms for this discharge are shown in figure 4.3.1. The calculated axis temperature is approximately 5300 K and the wall temperature is set to 1375 K. The axis temperature is higher in comparison with the SON lamps because of the lower sodium dosage. The temperature profile near the wall first shows a small increase of the slope and than a larger decrease of the slope. The increase of the slope is related to the absorption of radiation. The subsequent decrease is caused by the formation of sodium iodine. This limits the amount of atomic sodium that is available for absorption of radiation. The cumulative radiation losses show that around 5 W of radiation is absorbed in the outer mantle.

The calculated integrated spectrum for the sodium iodine discharge is shown in figure 4.3.2. The mercury density and temperature are increased in comparison with the SON lamp. As a

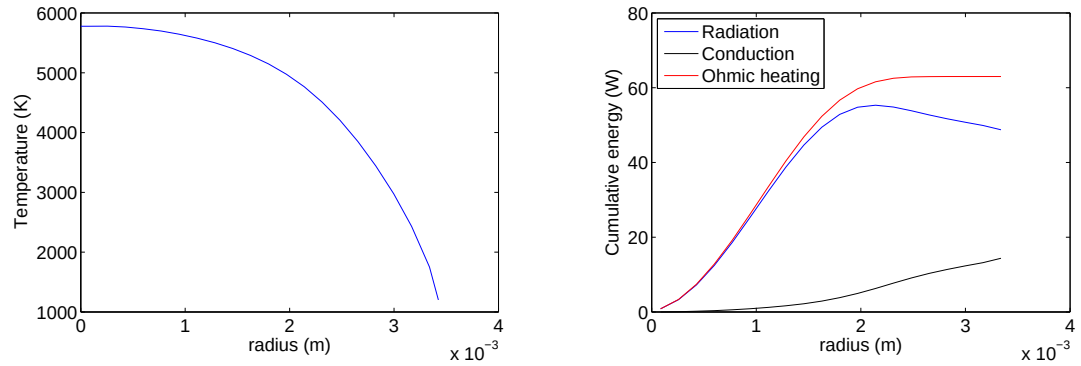

(a) (b)

Figure 4.2.1: *a) The simulated temperature profile of the pure mercury lamp. The axis temperature is around 5800 K and the wall temperature is set to 1200 K. b) The cumulative integrated source terms. Starting from the point where the cumulative radiated energy reaches a maximum an additional 6.6 W is absorbed in the outer mantle.*

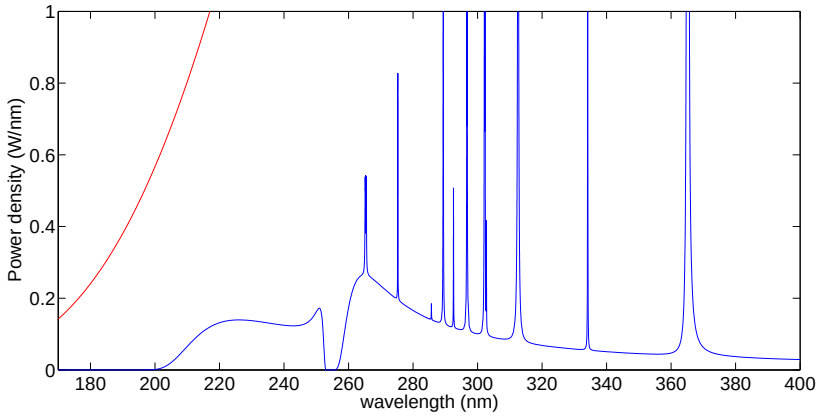

Figure 4.2.2: *The resonant lines for the 70 W mercury lamp. In comparison with the 250 W mercury lamp the van der Waals broadening of the red wings of the resonant lines has increased considerably.*

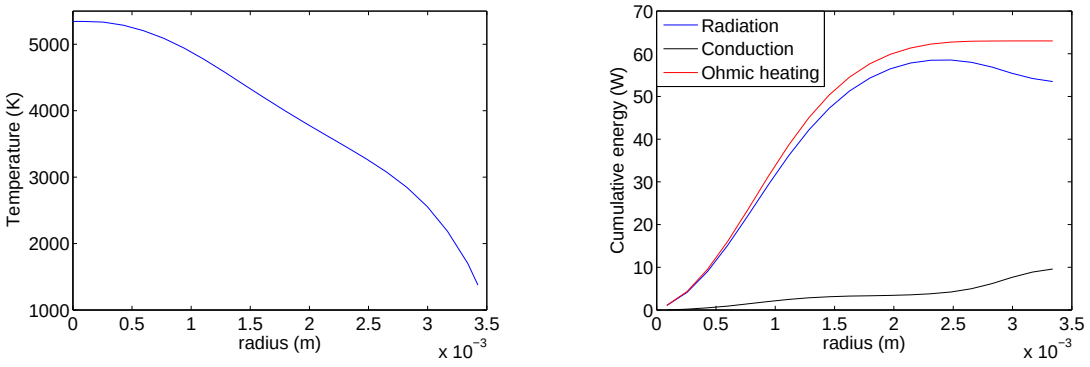

(a) (b)

Figure 4.3.1: *a) The temperature profile of the sodium iodine lamp. Near the wall the slope of the temperature profile first increases slightly due to an increase in absorption of radiation. Even closer to the wall the absorption decreases because of the sodium that is bound in molecular compounds. Therefore the slope decreases again. b) The cumulative integrated source terms for the sodium iodine discharge. Close to the wall the same increase and decrease of absorption can be observed as in the temperature profile.*

consequence the mercury radiation of several transitions in the visible can be observed. The much higher mercury density also increases the broadening of the red wing of the sodium D-lines and the 818-819 nm lines.

4.4 Hg+TlI

The thallium iodide lamp contains 8.5 mg of mercury and 3.33 mg of thallium iodide. Measurements of the thallium spectrum show that the spectrum is dominated by continuum radiation. This continuum reduces the axis temperature in such a way that the emission of mercury radiation is no longer visible. Currently this continuum can not be taken into account in the model. This section therefore only covers a thallium iodide simulation without molecular radiation. Due to the low temperature the mercury pressure is estimated with 15 bar. At 4000 K the thallium pressure is 0.65 bar when a coldspot temperature of 1200 K is used in the convection limit.

The simulated temperature profile and cumulative integrated source terms are shown in figure 4.4.1. The calculated axis temperature is around 5300 K and the wall temperature is set to 1375 K. The temperature profile exhibits a similar shape in comparison with the temperature profile of the sodium iodide lamp. Close to the wall the decay of the temperature profile decreases due to absorption of radiation. When the thallium which is responsible for the absorption is bound to form thallium iodide the amount of radiation which is absorbed decreases. As a result the temperature profile decays faster near the wall. This 'bump' in the temperature profile appears at a lower radius in comparison with the sodium lamp. This is an indication that the amount of radiation absorbed near the centre of the discharge is higher in the thallium lamp. In the outer mantle only 3.8 W of radiation is absorbed. In the measured thallium iodide lamp the 535 nm thallium line also absorbs a part of the continuum radiation which is emitted close in the wavelength interval close to the line centre.

The calculated integrated spectrum is shown in figure 4.4.2. The resonance and van der Waals broadening constants used for this simulation are all calculated theoretically. The spectrum is dominated by thallium radiation. The thallium spectrum has two strong ultraviolet transitions at 352 and 378 nm. In lamps thallium is mainly used for the 535 nm line radiation. Measurements show that thallium also has some significant infrared lines. These lines were not included because no transition probability is available.

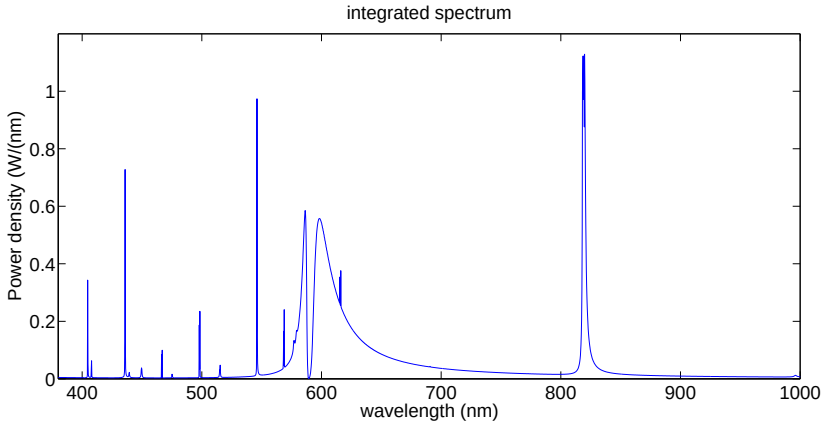

Figure 4.3.2: *The integrated spectrum for the sodium iodine lamp. In comparison with the SON lamp the mercury lines are visible because of the higher mercury density and temperature. The van der Waals broadening of the sodium D-lines is also more prominent.*

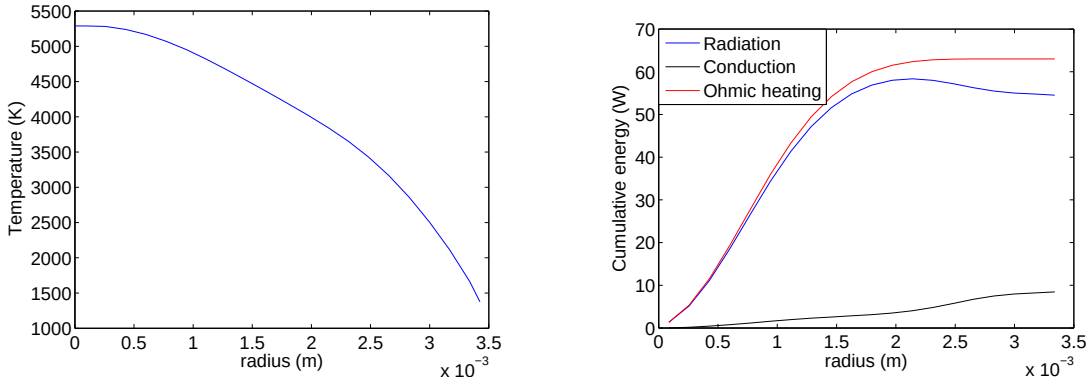

(a) **(b)**

Figure 4.4.1: *a) The temperature profile of the thallium iodide simulation. The temperature profile is similar to the sodium iodide lamp. There is an increase of the slope of the temperature profile close to the wall related to absorption and a decrease of the slope where the thallium atoms are forming thallium iodide. b) The cumulative integrated source terms for the thallium iodide lamp. In the outer mantle 3.8 W of radiation is absorbed.*

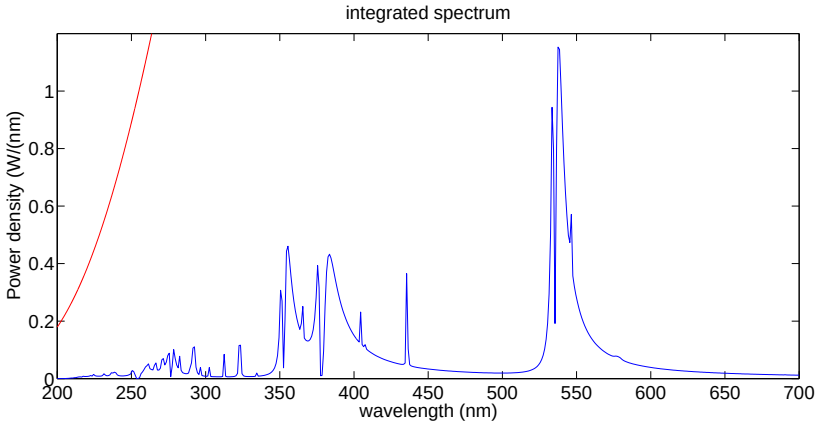

Figure 4.4.2: *The simulated thallium iodide integrated spectrum. The output of the 352, 378 and 535 nm thallium lines dominate the spectrum. Due to the high mercury pressure all of these lines have a strongly broadened red wing.*

4.5 Hg+InI

The indium iodide lamp contains 8.5 mg of mercury and 3.33 mg of indium iodide. Measurements of the indium spectrum show that the amount of indium radiation is relatively low. Therefore it is assumed that the same effective temperature which was used for the pure mercury lamp can be used to estimate the mercury pressure in the indium iodide lamp. The mercury pressure thus is taken to be 30 bar. By using a coldspot temperature of 1200 K the indium pressure at 5000 K is 2.6 bar in the convection limit. With this indium pressure the calculated spectrum is dominated by indium radiation as shown in figure 4.5.1. The indium dosage in the simulation was therefore reduced with a factor 10000 to obtain better agreement with the experiment. The indium dosage had to be adjusted since the lowest available coldspot temperature still resulted in a pressure which was too high. This strongly suggests that the specified amount of indium is incorrect. The indium pressure with the adjusted dosage is 37 Pa at 5000 K. The measured calibrated spectrum of the indium iodide lamp is shown in figure 6.4.1.

The simulated temperature profile and cumulative integrated source terms for the simulation with the adjusted dosage are shown in figure 4.5.2. The predicted axis temperature is 5700 K and the wall temperature is set to 1375 K. The temperature profile is more flat in comparison with the sodium iodide lamp. This difference is caused because the indium iodide spectrum is dominated by mercury radiation. The optical depth of this radiation is very high which means absorption already takes place close to the centre of the discharge. In the outer mantle 6.7 W of radiation is absorbed.

The calculated integrated spectrum is shown in figure 4.5.3. The van der Waals and resonance broadening constants of the indium lines are calculated theoretically. The model contains seven indium transitions. These are the 256, 271, 303, 325.6, 325.9, 410 and 451 nm lines. All of these lines are self reversed. None of these lines has a line centre which is completely absorbed similar to the 185 and 254 nm mercury lines. The reabsorption of this radiation therefore mainly occurs close to the centre of the discharge and is negligible in comparison with the reabsorption of the mercury radiation.

4.6 Conclusion

Simulations of all four single salt lamps were made. The broadening constants of the species in the discharge are important input parameters. These parameters have been obtained by comparing simulated spectra with measured spectra. Such a comparison is possible for the pure mercury

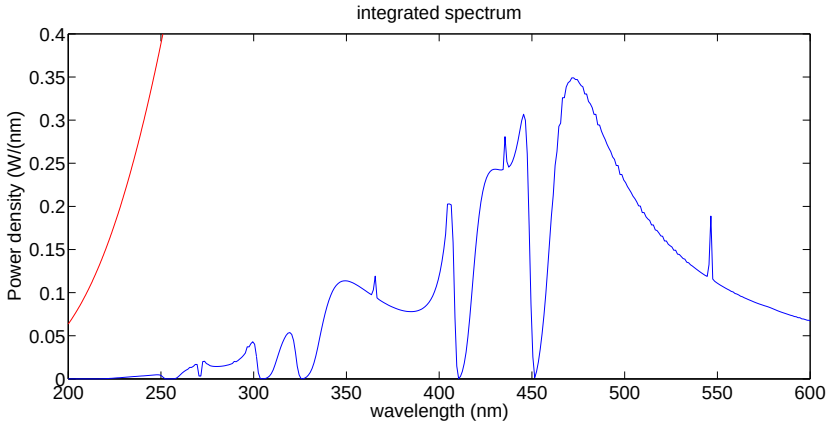

Figure 4.5.1: *The spectrum for the indium iodide simulation with a coldspot temperature of 1200 K. The radiation from the indium 271, 303, 325, 410 and 451 nm lines dominate the spectrum.*

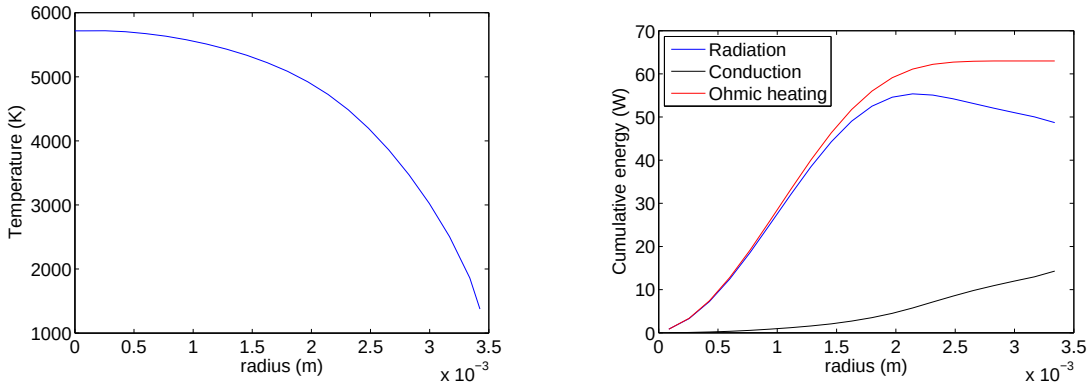

(a) **(b)**

Figure 4.5.2: *a) The temperature profile of the indium iodide lamp. The temperature profile in the centre is very flat. This is caused by strong radiative heating of the area close to the centre of the discharge by absorption of mercury radiation. b) The cumulative integrated source terms. In the outer mantle 6.7 W of radiation is absorbed.*

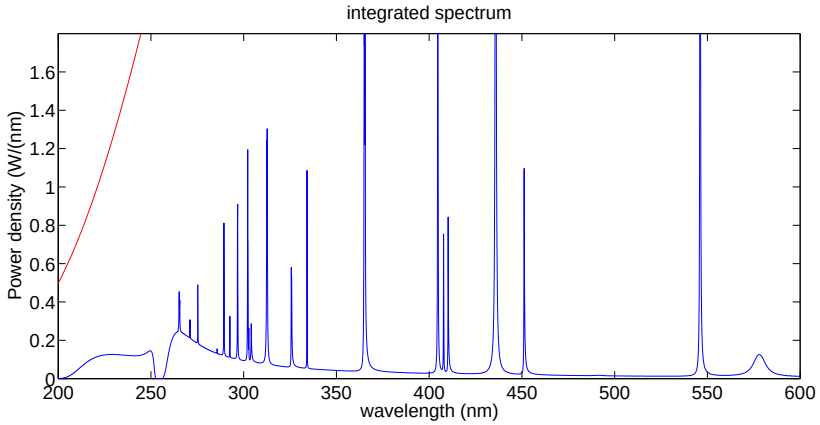

Figure 4.5.3: *The integrated spectrum for the indium iodide lamp for a reduced dosage. All indium lines are self reversed. None of these lines has a line centre which is completely absorbed. As a consequence most of the absorption of the indium lines takes place close to the centre of the discharge. The reabsorption of the mercury radiation therefore controls the temperature profile.*

lamp and the sodium iodide lamp. The lamps which are used for this comparion are the 250 W mercury lamp and the 70 and 400 W SON lamps. For these lamps the reactive conductivity is included in the model. This means that for these one dimensional lamps all important phenomena are accounted for and a comparison of the spectrum is thus meaningfull.

Only for mercury broadening constants from literature are available. A comparison of the constants from literature with the constants used in the model shows that the van der Waals broadening constants for the resonant mercury lines are reduced considerably to obtain the correct energy in the 577 and 579 nm lines. With these constants a good agreement was reached between the measured and simulated energy in the visible mercury lines of the 250 W mercury lamp. The 70 W mercury lamp showed a strong broadening of the red wings of the resonant lines. The mercury model should therefore be recalibrated with an ultraviolet spectrum.

The luminous efficacy of the 70 W SON lamp could be predicted with an accuracy of 20 %. This lamp was only calibrated for the self reversal width of the sodium D-lines. With the same broadening constants the luminous efficacy of the 400 W SON lamp was predicted within 30 %. This difference is related to the uncertainty in the broadening constants of the sodium D-lines and the mercury pressure in the 70 W SON lamp.

Predictions for the sodium, thallium and indium iodide lamps are difficult because the coldspot temperature is unknown and the reactive conductivity is not included. For the indium lamp the species dosage differs from the specified dosage. For all of these lamps a temperature profile is obtained which can be expected from these lamps. Depending on the optical depth of the dominant radiating species there is a point in the discharge where the absorption of radiation is strongest. At this point the gradient of the temperature profile increases. If the dominant radiating species can be bound with iodide this absorption decreases rapidly which results in a decrease of the temperature gradient.

Chapter 5

Setup and methods

In this chapter the setup and the experimental methods are discussed. The setup will be examined first. The most important components are discussed in more detail. These components are the integrating sphere and the fourier transform spectrometer. After that the calibration and measurement procedure are considered. An error analysis for the calibrated spectra is given as well.

5.1 Setup

In this section the setup is discussed in more detail. The primary components of the setup are the integrating sphere and the fourier transform spectrometer. These components are discussed first before the complete setup is addressed.

5.1.1 Integrating sphere

An integrating sphere measures the spectral radiant flux of a lamp. This is the spatially and angularly integrated spectral radiance. First some basic integrating sphere theory is discussed. After that the most important design considerations for a good integrating sphere are considered. These design considerations are compared with the design of the integrating sphere in our setup.

5.1.1.1 Theory

Ideally an integrating sphere has a perfectly diffusive surface. Such a surface reflects the incoming radiation with a cosine angular dependency as a Lambertian surface. The total radiant flux Φ_t emitted by the surface of the sphere is given by

$$\Phi_t = \Phi_L \sum_{i=1}^{\infty} \rho^i (1-f)^i = \Phi_L \rho (1-f) \sum_{i=0}^{\infty} \rho^i (1-f)^i = \frac{\Phi_L \rho (1-f)}{1-\rho(1-f)}. \tag{5.1}$$

with Φ_L the radiant flux of the source, ρ the reflectivity of the surface and f the ratio of the area of the gap to the total area given by

$$f = \frac{A_g}{A} = \frac{A_g}{A_s + A_g}, \tag{5.2}$$

with A_g the area of the gap and A_s the surface area of the sphere and A the total area given by $A = A_s + A_g$. The total radiance of the sphere surface is given by [33]

$$I_s = \frac{\Phi_t}{\pi A_s} = \frac{\Phi_L}{\pi A} \frac{\rho}{1-\rho(1-f)} = \frac{\Phi_s}{\pi A} M, \tag{5.3}$$

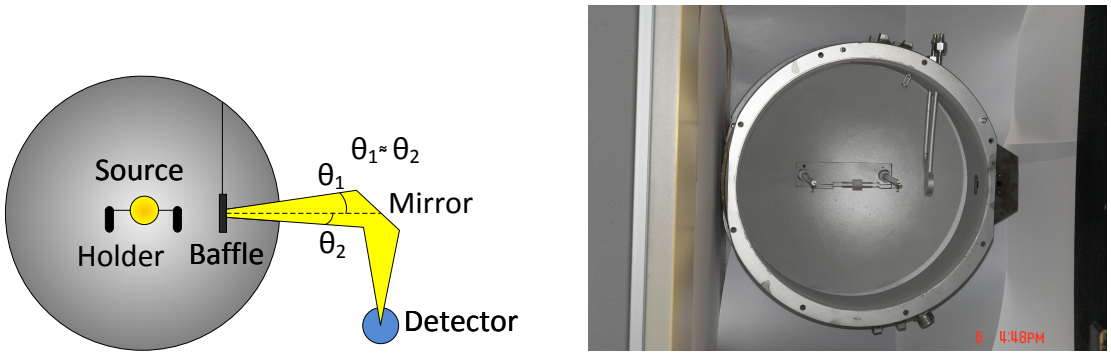

(a) (b)

Figure 5.1.1: *a) The integrating sphere contains a few foreign objects. These are a holder and a baffle. The lamp can be mounted in the holder and the baffle prevents the radiation of the lamp from leaving the sphere without any reflections. The detector is focused on the baffle. The radiance of the baffle can be approximated with the radiance of the sphere surface. The solid angle which is projected on the detector is a function of the zenith angles θ_1 and θ_2. These angles are approximately equal. b) A picture of the integrating sphere. The cylindrical part and one concave part are shown. A discharge tube was removed from the outer bulb and mounted in the holder. The baffle shielding the gap is visible as well.*

with M the sphere multiplier. It is important to note that this equation is derived for an empty sphere. A real integrating sphere always contains foreign objects. As a result the predicted radiance is overestimated. Equation 5.3 shows that the surface radiance increases in the following cases:

- A smaller radius of the sphere which decreases the surface area
- A smaller ratio of the area of the gap and the area of the sphere
- A higher reflectance

The radiative flux that reaches the detector is given by

$$\Phi_d = I_s A_d \Omega_d, \tag{5.4}$$

with I_s the radiance of the sphere surface, A_d the focus area of the detector on the baffle and Ω_d the solid angle which is projected on the detector. The solid angle can be approximated by

$$\Omega_d = \int_0^{\theta} sin\theta' cos\theta' d\theta' \int_0^{2\pi} d\phi = \pi sin^2(\theta), \tag{5.5}$$

when it is assumed that the surface is a Lambertian radiator. The drawing presented in figure 5.1.1 defines the angle θ.

5.1.1.2 Design considerations

The performance of an integrating sphere is influenced by the baffle, the radius, the reflectivity and the holder. These properties are discussed by Bergmann and Ohno [34]. A summary is given here.

The baffle is an object that is placed before the gap to prevent a direct passage of the radiation from the lamp towards the detector. This means that any radiation reaching the detector is reflected at least twice inside the sphere. The introduction of the baffle results in an area

behind the baffle which can not be reached directly by the radiation of the lamp. Such an area also exists at the other side of the baffle. This area has no direct passage to the detector. The presence of these areas disturbs the uniform integrating performance. The baffle is coated with a reflective coating to minimize absorption.

The radius should be as large as possible since a larger radius reduces the relative area of foreign objects like the baffle, the lamp and the lamp holder. The absorption of these objects disturbs a uniform integrating performance. The size of the sphere is limited since an increase of the radius reduces the surface radiance.

The reflectivity is dependent on the application. A high reflectivity, 0.95-0.98, is required for reducing the spatial non-uniformity and increasing the surface radiance. A drawback of higher reflectivity is the increased sensitivity to self absorption by foreign objects. Lower reflectance, 0.8-0.9, is more stable in the long term since for these reflectivities the sphere multiplier is less sensitive to small changes in the reflectance.

The holder can mount the lamp. The absorption of this object can be minimized using a high reflectance coating.

5.1.1.3 The integrating sphere

The integrating sphere used for the experiments described in this report consists out of three sections. Two sections are concave parts and the section in between is cylindrical. The cylindrical part has a 14 cm radius and a height of 10 cm. A hatch is made in one of the concave parts. This is where the lamp can be mounted in the sphere by placing it in the holder.

The coating of the sphere is chosen to ensure measurements in a wide spectral range. An aluminium coating is used since aluminium has a good reflectivity in the visible and the infrared. Prior to the coating the inner surface of the sphere was made diffuse by pearl blasting it.

A large amount of radiation is absorbed by the sphere. Measurements in the infrared require a setup with a stabilized temperature. Therefore the sphere is made of a 4 mm thick wall of copper to ensure a good thermal conductivity. A system of square tubes is wound around the sphere as a temperature regulation system. Square tubes are chosen to maximize the contact area of the temperature regulation system with the sphere. By pumping water through the tubes the sphere can be maintained at a constant temperature with an estimated error of 0.1 K. The baffle and the holder are cooled with a separate system. The water flows through the baffle. The holder is cooled from the outer surface of the sphere. The holder contains the electrical wiring which provides the input power to the lamp. One rod of the holder also contains a thermo couple to be able to measure the temperature at the top side of the rod. This temperature will be used to estimate the conduction losses through the rods of the holder. A picture of the inner side of the sphere is shown in figure 5.1.1.

5.1.2 Fourier transform spectroscopy

In this section the principles of Fourier transform spectroscopy are discussed. Fourier transform spectroscopy, or FTIR, modulates every wavelength by a different frequency and obtains a spectrum by Fourier transforming the result. These modulations can be achieved with a Michelson interferometer. A schematic drawing of the FTIR is presented in figure 5.1.2. The radiation incident on the FTIR is divided in two beams by a beamsplitter. One of these beams traverses a constant path. The path of the other beam is dependent on the position of a continuously moving mirror. As a result both beams interfere. The detector thus measures an interferogram.

The interference of monochromatic radiation with wave number $\tilde{\nu}$, spectral radiance $I_0(\tilde{\nu})$ and optical path difference x can be expressed as

$$I(x, \tilde{\nu}) = \frac{1}{2} I_0(\tilde{\nu}) \left[1 + cos(2\pi\tilde{\nu}x)\right]. \tag{5.6}$$

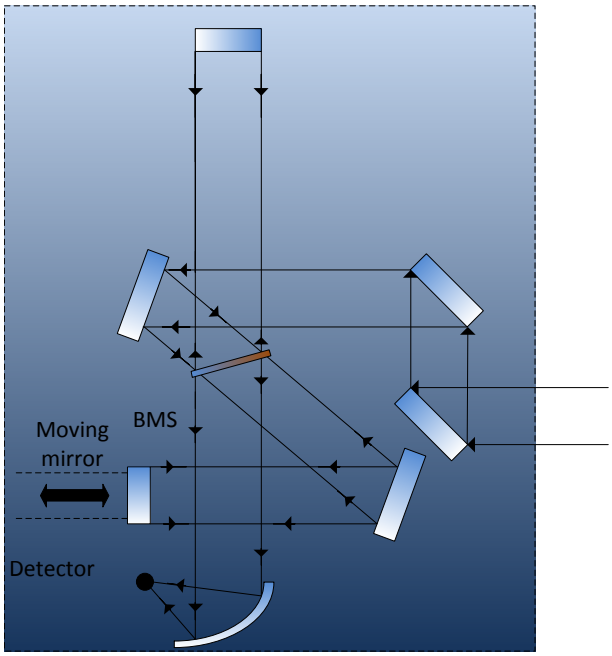

Figure 5.1.2: *The path of the radiation inside the FTIR. The Michelson interferometer separates the incoming beam with a beam splitter (BMS). One beam traverses a constant path while the path length of the other beam is dependent on the position of the moving mirror. As a result an interferogram is measured at the detector.*

The varying part of the radiance can then be expressed as

$$I(x) = \frac{1}{2}\int_0^\infty I_0(\tilde{\nu})\, cos(2\pi\tilde{\nu}x)\, d\tilde{\nu} = \int_{-\infty}^\infty B(\tilde{\nu})\, exp(i2\pi\tilde{\nu}x)\, d\tilde{\nu}, \tag{5.7}$$

with $B(\tilde{\nu}) = \frac{1}{4}I_0(\tilde{\nu})$. Therefore it is concluded that the radiance reaches a maximum for all wavenumbers when the path difference is zero[1]. The varying part of the radiance is equal to the Fourier transform of $B(\tilde{\nu})$. This function can be calculated by taking the inverse Fourier transform of the interferogram as

$$B(\tilde{\nu}) = \frac{1}{2\pi}\int_{-\infty}^\infty I(x)\, exp(-i2\pi\tilde{\nu}x)\, dx. \tag{5.8}$$

In reality the interferogram can only be measured over a finite length L. The resolution of the resulting spectrum can be approximated with $\Delta\tilde{\nu} \approx \frac{1}{L}$. In an ideal case only one side of the interferogram has to be measured since $I(x) = I(-x)$. In general this relation is not valid due to experimental imperfections [42]. Dispersion in the beamsplitter is an example of one of these imperfections. These imperfections can be calculated by measuring a small double sided interval around $x = 0$. When this information is applied in a one sided interferogram the measurement time can be decreased or the resolution can be increased.

5.1.3 Setup

A schematic view of the complete setup is shown in figure 5.1.3. The integrating sphere surface is cooled with circulating water. The holder and the baffle are cooled with a separate system. The

[1]The beamsplitter used in the FTIR has only one reflecting side. That means the reflections on the low pressure-BMS interface are external and reflections on the BMS-air interface are internal . The externally reflected beam is phaseshifted by π rad. The interferogram is therefore asymmetric and actually reaches a minimum at a path difference of zero.

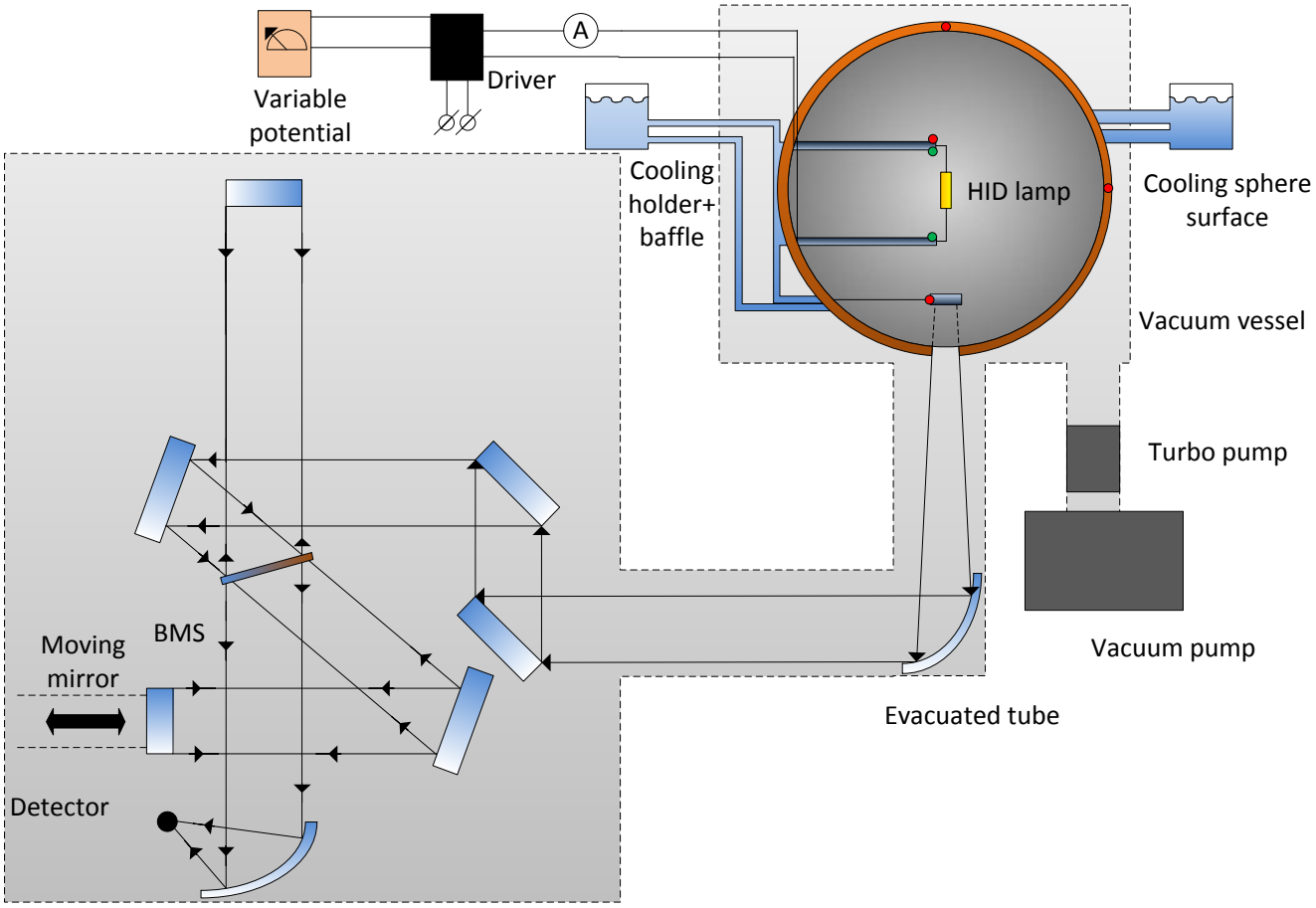

Figure 5.1.3: *The complete setup: The integrating sphere is kept at a constant temperature with a cooling system. The holder and the baffle are cooled with a separate system. The lamp is operated by a driver. The driver regulates the input power for the lamp as a function of the potential applied to it. A power analyzer measures the lamp current. Simultaneously the lamp voltage is measured at the positions indicated on the holder with green dots. The four red dots indicate the positions where the temperature is measured. The complete path of the radiation from the sphere to the FTIR is in a vacuum environment. The sphere reaches a low pressure of approximately* 10^{-3} *Pa with a multistage roots pump. The FTIR is a separated vacuum system. Its pressure is maintained at a few mbar.*

water flows through the baffle. The holder is cooled via conduction through the surface of the sphere. The consequence is that a small temperature gradient exists across the rods of the holder. The conduction losses are estimated by measuring the temperature at the top of one of the rods of the holder. The temperature at the bottom of the rod is taken as the temperature of the cooling water. Temperature measurements are also made at the baffle, the top of the sphere and a side of the sphere to estimate temperature stability and temperature uniformity.

The lamp is operated by a driver. The lamp power supplied by the driver can be regulated. The lamp voltage and the lamp current are measured with a power analyzer.

The sphere is placed in a vacuum vessel. The vacuum environment prevents corrosion of the discharge tube and absorption of radiation. The vacuum vessel is kept at a pressure of a few millipascal by a multistage roots pump. A tube connects the optical path of the FTIR and the sphere with each other. The tube is a part of the vacuum vessel. The environment of the FTIR is a separate vacuum system. Its pressure is kept at a few mbar.

Insulation material is used to built a box around the FTIR. Inside this box a heating system is placed which regulates the temperature of the air surrounding the FTIR. This will improve the stability of the FTIR temperature and makes it less sensitive to seasonal and day to night variations of the laboratory temperature.

5.2 Measurement procedures

The sphere calibration procedure and the calibration sources are discussed first. Then the measurement procedures along with the detectors and beamsplitters used to cover the spectral range from 380 nm to 10 μm are considered. After that an estimate of the error of the calibrated spectra is given.

5.2.1 Calibration sources and procedures

No standard calibration procedure is present for integrating sphere measurements in the infrared. A calibration requires a stable infrared source with a known output. Tests indicated that a platinum ribbon was most stable. The radiative flux emitted by the ribbon is calculated using a numerical model. The remaining part of the spectrum is calibrated with a halogen lamp. The radiative flux of the halogen lamp is determined at Philips OCM calibration laboratories.

The spectral power can be determined from the measured signal at the detector. It is important to note that each measured signal $S_{\tilde{\nu}}$ is an average of multiple individual measurements. Each individual measurement is determined by taking the average of at least one hundred spectra. The total number of spectra sampled to obtain $S_{\tilde{\nu}}$ is therefore in the order of a few hundred. The measured signal at the detector can be expressed as

$$S_{\tilde{\nu},source} = k_1 \Phi_{\tilde{\nu},source} + k_2 \Phi_{\tilde{\nu},sphere}\left(T_{sphere}\right) + k_3 R_{\tilde{\nu}}, \tag{5.9}$$

with k_x a proportionality function, $\Phi_{\tilde{\nu},source}$ the spectral power emitted by the source, $\Phi_{\tilde{\nu},sphere}\left(T_{sphere}\right)$ the spectral power emitted by the sphere and $R_{\tilde{\nu}}$ the spectral power emitted by objects outside the integrating sphere. The proportionality function of the measured signal with the spectral power of the source can be extracted by making a background measurement:

$$k_1 = \frac{S_{\tilde{\nu},source} - S_{\tilde{\nu},BG}}{\Phi_{\tilde{\nu},source} - \Phi_{\tilde{\nu},BG}} \approx \frac{S_{\tilde{\nu},source} - S_{\tilde{\nu},BG}}{\Phi_{\tilde{\nu},source}}, \tag{5.10}$$

where it was assumed that the spectral power of the source at the sphere temperature in the background measurement can be neglected when compared with the spectral power of the source in operation. A calibrated spectrum can be obtained as

$$\Phi_{\tilde{\nu},lamp} = \frac{S_{\tilde{\nu},lamp} - S_{\tilde{\nu},BG}}{k_1} = (S_{\tilde{\nu},lamp} - S_{\tilde{\nu},BG}) k_{\tilde{\nu},ref}, \tag{5.11}$$

with $\Phi_{\tilde{\nu},lamp}$ the calibrated spectral power, $S_{\tilde{\nu},lamp}$ and $S_{\tilde{\nu},BG}$ the measured signals of a lamp turned on and a lamp turned off and $k_{\tilde{\nu},ref}$ the calibration function defined as $\frac{1}{k_1}$.

5.2.1.1 Platinum ribbon

The calibration function for the spectral part calibrated with the platinum ribbon is defined as

$$k_{\tilde{\nu},ribbon} = \frac{\Phi_{\tilde{\nu},ribbon}}{S_{\tilde{\nu},ribbon} - S_{\tilde{\nu},BG}}. \tag{5.12}$$

The spectral power of the platinum ribbon, $\Phi_{\tilde{\nu},ribbon}$, is calculated with a numerical model. First the energy balance for the ribbon is solved to obtain the temperature profile. After that the temperature profile is used to calculate the spectral radiance.

The thickness and the width of the ribbon are small compared to its length. In the calculations the ribbon can thus be considered as a one dimensional object. A numerical solution can be obtained with equation 3.6. The energy balance for the platinum ribbon contains ohmic heating, thermal radiation and conduction terms:

$$I^2 \frac{\Delta x}{A} \rho_{ribbon} = \epsilon_{ribbon} \sigma \left(T^4 - T_0^4\right) - \lambda_{ribbon} \nabla^2 T, \tag{5.13}$$

with I the current, Δx the length of one control volume, A the cross section of the ribbon, ρ_{ribbon} the resistivity of platinum [37], ϵ_{ribbon} the effective emissivity [35], σ is the Stefan-Boltzmann constant, T_0 the sphere temperature and λ_{ribbon} the conductivity of platinum [36]. Convection is neglected because the platinum ribbon will be measured in an evacuated integrating sphere. The temperature profile can be calculated for different currents as shown in figure 5.2.1.

When the temperature profile is known the spectral radiance emitted by the surface of one control volume can be calculated as

$$\Phi_{\tilde{\nu},ribbon} = \pi \Delta x p\left(x\right) \epsilon\left(\tilde{\nu}, T\right) I_{BB}\left(\tilde{\nu}, T\right), \tag{5.14}$$

with $p\left(x\right)$ the perimeter at position x, $\epsilon\left(\tilde{\nu, T}\right)$ the spectral emissivity [38] and $I_{BB}\left(\tilde{\nu}, T\right)$ the spectral radiance of a blackbody. The spectral emissivity is only known for a few wavelengths. Therefore the spectral emissivity is interpolated. The spectral emissivity can be related to the effective emissivity as

$$\epsilon_{ribbon}\left(T\right) = \frac{\pi \int_0^\infty \epsilon\left(\tilde{\nu}, T\right) I_{BB}\left(\tilde{\nu}, T\right) d\tilde{\nu}}{\sigma T^4}, \tag{5.15}$$

where it was assumed that the surface is a Lambertian radiator. In general the integrated spectral emissivity is not equal to the effective emissivity. Therefore the spectral radiance is corrected with the ratio of the effective emissivity to the integrated spectral emissivity. The calculated spectral power for several currents is shown in figure 5.2.1. The part of the spectrum that can be calibrated with the ribbon is determined by two constraints. The first constraint concerns the possibility of separating the measured background signal from the measured signal of the strip. For wavenumbers below $1000\,\mathrm{cm^{-1}}$ the accuracy of this operation decreases rapidly. The second constraint is that the spectral power of the strip is sufficiently high. For wavenumbers above $12821\,\mathrm{cm^{-1}}$ this criterium is no longer fulfilled.

5.2.1.2 Halogen lamp

The calibration function for the spectral part calibrated with the halogen lamp is given by

$$k_{\tilde{\nu},halogen} = \frac{\Phi_{\tilde{\nu},halogen}}{S_{\tilde{\nu},halogen} - S_{\tilde{\nu},BG}}. \tag{5.16}$$

The spectral power of the halogen lamp $\Phi_{\tilde{\nu},halogen}$ is measured at Philips OCM calibration laboratories. The spectral power is plotted in figure 5.2.2. The spectral part which can be calibrated with the halogen lamp is limited by the sensitivity of the detectors and the transmittance of the beamsplitters that are available. In this setup the halogen lamp can be used as a calibration source until $26316\,\mathrm{cm^{-1}}$.

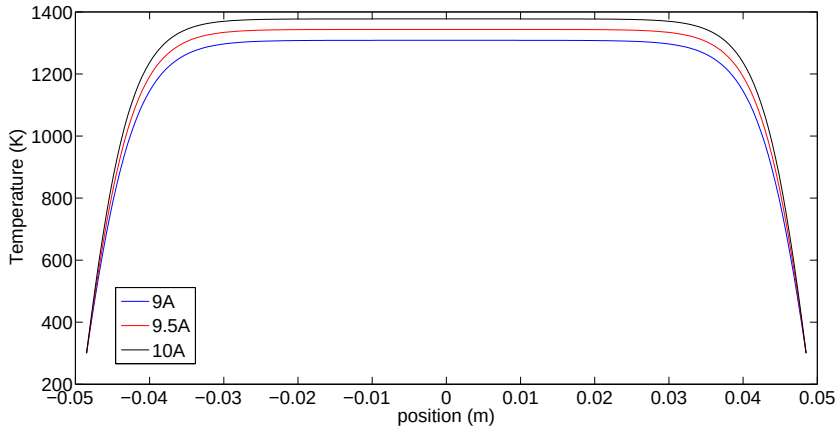

(a)

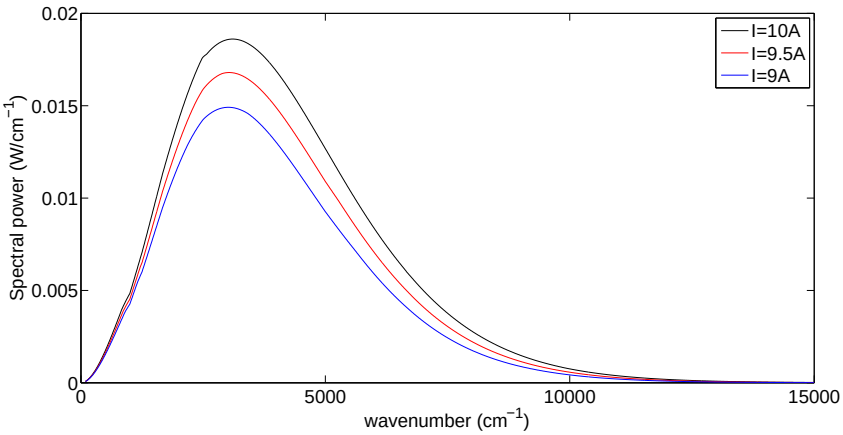

(b)

Figure 5.2.1: *a) The calculated temperature profile of the platinum ribbon is shown for 3 different currents. b) The spectral power emitted by the platinum ribbon for 3 different currents. The spectral power decays fast for high wavenumbers which means that a different calibration source is required for the visible spectrum. The platinum ribbon is used as a calibration source in the spectral range* $1000 - 12821\ cm^{-1}$.

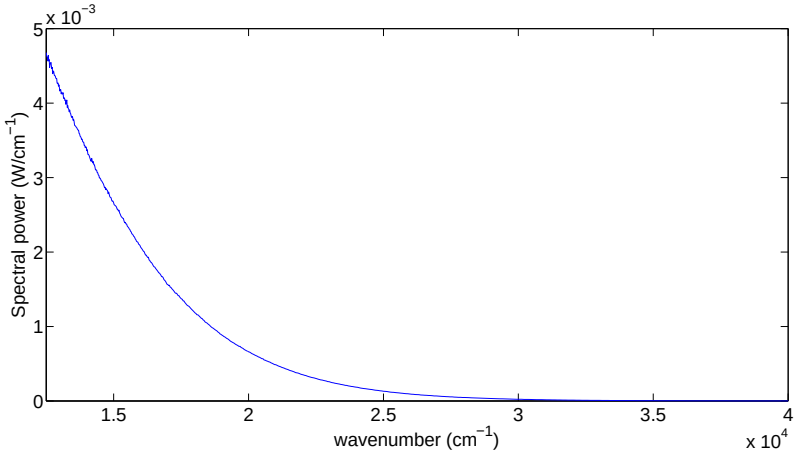

Figure 5.2.2: *The spectral power of the halogen lamp used in the visible calibration. The spectral range which is calibrated with the halogen lamp is* $12821 - 26316\ cm^{-1}$.

5.2.2 Calibrated measurements

Measurements in the spectral range from $1000 - 26316\,\mathrm{cm}^{-1}$ require the usage of multiple detectors and beamsplitters. In this section the detector and beamsplitter combinations that have been used for a good coverage of the spectrum are discussed. The calibration function will be used to demonstrate the accuracy of the calibration. The calibration function for the spectral part calibrated with the platinum ribbon is made for multiple currents. Since the calibration function of the system should not be dependent on the current sent through the ribbon this is a way of verifying the accuracy of the calibration. The calibration function has a reciprocal proportionality with the sensitivity which means that low values of the calibration function indicate a high sensitivity. For every lamp measurement an estimate will be made for the conduction losses as well.

5.2.2.1 Far infrared

In this work the far infrared is defined as the spectral range from $1000 - 2500\,\mathrm{cm}^{-1}$ which is equivalent to $10 - 4\,\mu\mathrm{m}$. The measurements in the far infrared are made with a DLaTGS detector and a KBr beamsplitter. A DLaTGS detector measures the potential of a crystal. This potential is dependent on the spectral radiant flux incident on the cell. Small temperature changes influence the polarization of the crystal. This principle is called pyroelectricity. In a background measurement the polarization of the crystal is proportional to the temperature difference between the integrating sphere and the detector. That means when both objects have the same temperature no signal is measured.

The temperature of the DLaTGS detector in operation conditions is approximately 305 K. The sphere temperature is kept at an approximate temperature of 308 K. This temperature is the highest temperature which can be reached by the current temperature regulation system. Lower sphere temperatures can not be used because the temperature of the DLaTGS detector should always be lower than the integrating sphere to perform a correct background correction. When the temperature of the sphere is below the temperature of the detector a dip appears in the infrared spectrum. As a consequence the measurements are sensitive to the stability of the cooling system of the sphere and the stability of the temperature regulation system of the spectrometer. Currently the detector temperature is ineffectively kept stable by placing the FTIR in an environment with a regulated air temperature. In the future this problem is reduced by cooling the DLaTGS detector directly with a Peltier element.

The calibration function is shown in figure 5.2.3. The calibrations made with multiple currents show the same calibration function. For wavenumbers above $2500\,\mathrm{cm}^{-1}$ the signal to noise ratio

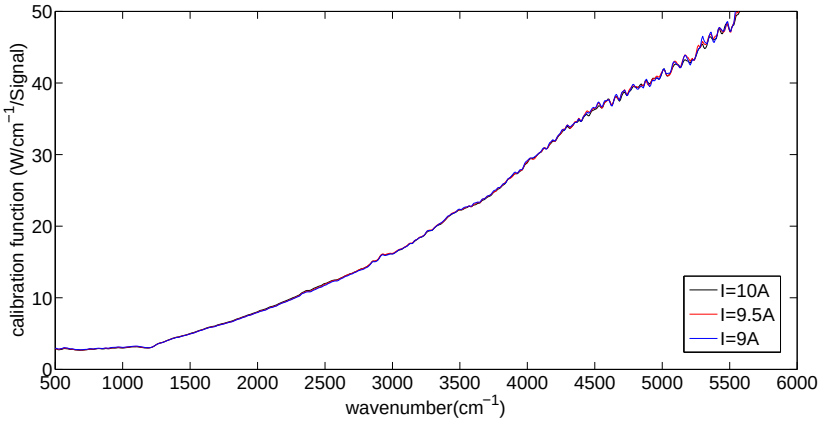

Figure 5.2.3: *The calibration function for the DLaTGS detector and the KBr beamsplitter. The calibration function was determined with the platinum ribbon which was operated at different currents. The calibration function is the same for all currents. This combination is used for* $1000 - 2500\ cm^{-1}$. *Above* $2500\ cm^{-1}$ *the DLaTGS sensitivity decays which results in a bad signal to noise ratio and below* $1000\ cm^{-1}$ *the systematic errors in the background correction are too large.*

rapidly decreases. For wavenumbers below $2000\,\mathrm{cm^{-1}}$ the systematic errors in the background correction are increasing since the integrating sphere is not maintained at the exact same temperature for the background and lamp measurements. This temperature error is estimated to be $0.1 - 0.2\,\mathrm{K}$.

The energy in the spectral part below $1000\,\mathrm{cm^{-1}}$ is estimated by integrating a blackbody curve which was scaled to match the calibrated spectral point at $1000\,\mathrm{cm^{-1}}$. This is an accurate estimate since the emissivity of the PCA is equal to one for this spectral part. The wall temperature used in this extrapolation is $1300\,\mathrm{K}$.

5.2.2.2 Near infrared

The near infrared is defined in this work as $2500 - 12821\,\mathrm{cm^{-1}}$ which is equivalent to $4 - 0.78\,\mu\mathrm{m}$. This range is covered with the MCT and Si detectors. Both detectors are semiconductors. For the MCT detector the principle of detection is the measurement of the resistance while for the Si detector the current is measured. Both detectors are used in combination with a CaF_2 beamsplitter. The MCT detector is cooled with liquid nitrogen to minimize thermal excitations due to its own temperature.

The MCT detector covers $2500 - 8500\,\mathrm{cm^{-1}}$ which is equivalent to $4 - 1.18\,\mu\mathrm{m}$. The calibration function for the MCT detector and CaF_2 is shown in figure 5.2.4. Again the calibrations determined for different currents provide the same calibration function. The MCT detector delivers a higher sensitivity in parts of the spectrum calibrated with the DLaTGS detector. However the DLaTGS detector is still prefered in this spectral area. In the far infrared the amount of thermal radiation of the sphere is much larger than the infrared radiation emitted by the lamp. For the MCT detector the background and lamp measurements therefore provide roughly the same amount of signal. The DLaTGS detector is not able to measure most of the sphere radiation. With the DLaTGS detector the difference between the amount of signal in the background and lamp measurements is thus larger. This larger difference decreases the errors made in the calibration. The upper limit of the spectral range calibrated with the MCT detector is set by the sensitivity of the detector. From a certain wavenumber on the signal to noise ratio is not sufficient anymore to obtain an accurately calibrated spectrum.

The Si detector covers $8500 - 12821\,\mathrm{cm^{-1}}$ or $1.18 - 0.78\,\mu\mathrm{m}$. The calibration function for the Si detector calibrated with the platinum ribbon is shown in figure 5.2.5. Again the calibration functions are equal for all settings. The stability of the Si detector is not good for wavenumbers below $8500\,\mathrm{cm^{-1}}$. This results in the undesirable situation with bad overlap between the calibrated

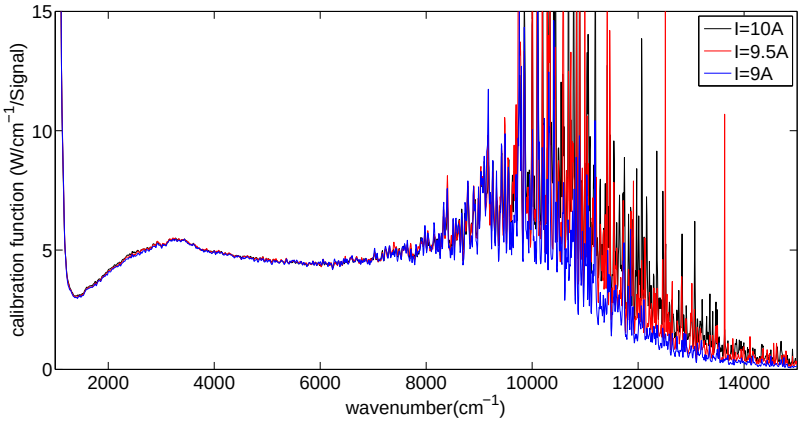

Figure 5.2.4: *The calibration function determined with the platinum ribbon and measured with the MCT detector and CaF_2 beamsplitter. The spectral part calibrated with these settings is* $2500 - 8500\ cm^{-1}$. *In this range the calibration function is the same for all currents. The spectrum is not calibated with these settings below* $2500\ cm^{-1}$ *because background and lamp measurements provide approximately the same amount of signal. Therefore relative errors are large in the calibration procedure. For high wavenumbers the accuracy of the calibration function is decreasing since the MCT detector can not measure the weak platinum ribbon radiance.*

spectrum measured with the MCT and the Si detectors. This makes a cross verification more difficult. The upper limit of the spectral range is determined by the lack of sufficient signal from the calibration source at wavenumbers above $12821\,\mathrm{cm}^{-1}$.

5.2.2.3 Visible

The visible part is defined as $380 - 780\,\mathrm{nm}$. This part is calibrated with a halogen lamp and is measured with a Si detector and a CaF_2 beamsplitter. The calibration function for these settings is shown in figure 5.2.6. The lower stability of the calibration function limits the range which can be calibrated accurately to approximately $24000\,\mathrm{cm}^{-1}$ or $417\,\mathrm{nm}$. That means a small part of the visible spectrum is calibrated with a lower accuracy. Around $16000\,\mathrm{cm}^{-1}$ a disturbance of the calibration function can be observed. This disturbance is caused by the laser beam which is used to determine the position of the moving mirror in the FTIR. Part of the laser beam was removed from the signal by placing an object in the beam path. The laser signal could not be removed completely and therefore an interpolation is made for this small spectral interval.

5.2.2.4 Conduction

The conduction losses through the holder can be estimated by assuming a linear temperature gradient. The bottom of the holder is kept at a constant temperature due to the temperature regulation system of the holder. The temperature at the top of one of the rods of the holder is measured. This temperature is also assumed for the top of the other cylindrical part. The conduction losses q_{cond} for both cylindrical parts can then be calculated as

$$q_{cond} = -2\lambda_{copper}\frac{T_{top} - T_{sphere}}{L}\pi R_{holder}^2, \tag{5.17}$$

with λ_{copper} the conductivity of copper, T_{top} the temperature measured at the top of one of the cylindrical parts of the holder, T_{sphere} the sphere temperature, L the length of the cylindrical part and R_{holder} the radius of the cylindrical part.

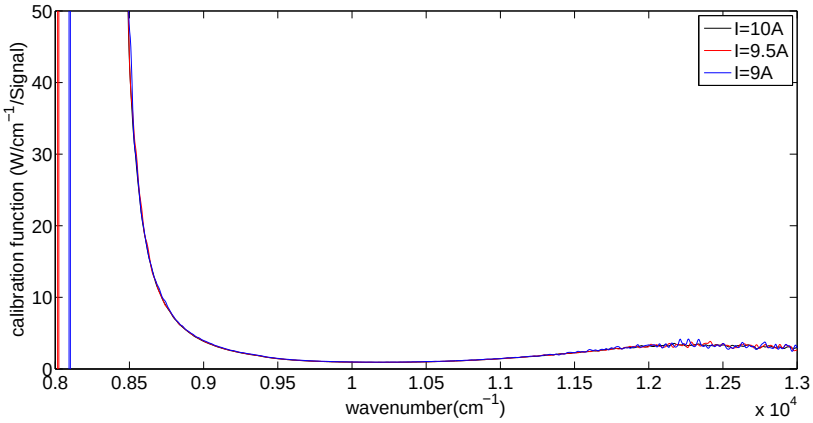

Figure 5.2.5: *The calibration function for the spectral part calibrated with the platinum ribbon and measured with the Si detector and CaF_2 beamsplitter. The spectral range $8500 - 12821\ cm^{-1}$ is calibrated with this detector. The accuracy of the calibration functions is decreasing above $12000\ cm^{-1}$ because the spectral radiance of the ribbon is very low in this spectral part.*

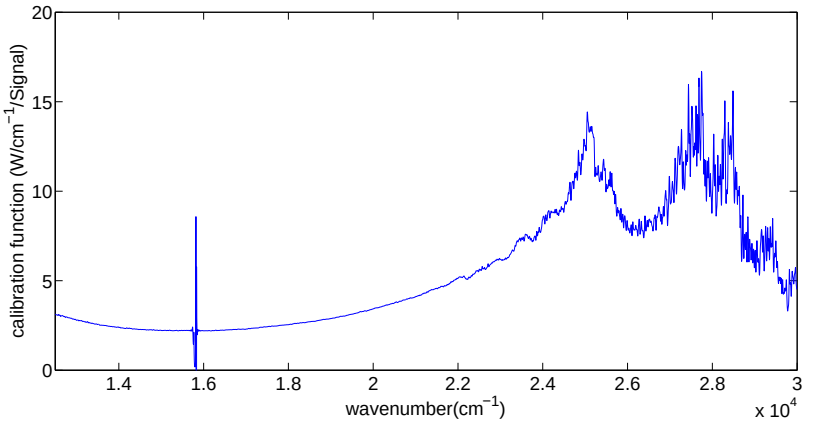

Figure 5.2.6: *The calibration function for the spectral part which is calibrated with a halogen lamp and measured with a Si detector and CaF_2 beamsplitter. The stability of the calibration function is decreasing at $24000\ cm^{-1}$. A small part of the visible spectrum is therefore calibrated with a lower accuracy. Around $16000\ cm^{-1}$ the calibration function is disturbed by the alignment laser beam of the FTIR. This signal is partly removed from the beam incident on the detector by placing an object in the beam. Since this signal could not be removed completely this part of the spectrum is interpolated.*

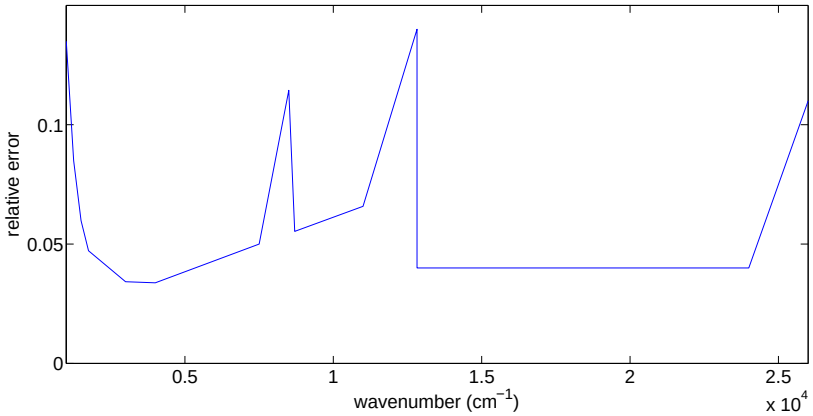

Figure 5.3.1: *The relative error for the spectral range considered in this work. The calibration errors made with the platinum ribbon increase towards the visible part of the spectrum. The calibration error made with the halogen lamp is constant in the visible part of the spectrum. In the far infrared additional errors are made because of the temperature stability problem of the integrating sphere. In the ranges* $7500 - 8700\ cm^{-1}$ *and* $11000 - 12821\ cm^{-1}$ *the lower sensitivity of the detectors limits the accuracy of the calibrated spectrum. Therefore a small additional error is added in those ranges. Above* $24000\ cm^{-1}$ *the sensitivity of the Si detector is decreasing.*

5.3 Error analysis

In this section an estimate of the error of the calibration is made. The total relative error is summarized in figure 5.3.1. The errors are caused by four factors. These factors are the temperature stability of the sphere and DLaTGS detector, errors in the spectral radiance of the calibration source, the reproducibility of the measured lamp signal and errors caused by a non uniform integration inside the integrating sphere.

The temperature stability is taken into account for wavenumbers up to $3000\,\mathrm{cm}^{-1}$. As indicated in section 5.2.2.1 the measured signal of the DLaTGS detector is sensitive to variations in temperature of the detector and the sphere. This error is estimated at 8% at $1000\,\mathrm{cm}^{-1}$ for the calibration measurement. This error is smaller in the lamp measurement because the spectral radiance of the lamp is higher. The error in the lamp measurement is estimated as 2%. This amounts to a total error of 10%. The peak of the background signal is measured at this wavenumber. For higher wavenumbers the measured background signal decreases. The measured signal in the calibration and lamp measurements reaches a maximum at approximately $2000\,\mathrm{cm}^{-1}$. The contribution of the error caused by a background correction thus rapidly decreases. At $1250\,\mathrm{cm}^{-1}$ the total error is reduced to about 5%. At $1500\,\mathrm{cm}^{-1}$ the error is expected to be around 2.5% and at $1750\,\mathrm{cm}^{-1}$ the contribution decreases to below 1.25%. From this point on a linear relation of the temperature stability error is assumed until $3000\,\mathrm{cm}^{-1}$ where it is no longer important.

Errors in the radiance of the calibration source are caused by small errors in the literature values of the platinum ribbon. The relative errors in the calculated spectral radiance of the platinum ribbon are caused by four factors. One of these factors is caused by an error in the predicted temperature profile of the ribbon. The other errors are caused by errors in the spectral emissivity. These errors are caused by the interpolation of the spectral emissivity, a different roughness of the platinum surface described in [38] and measurement errors of the spectral emissivity.

- The estimated error of the temperature of the ribbon is 5 K. The error of the radiance can be calculated by taking the derivative of the blackbody function with respect to temperature.

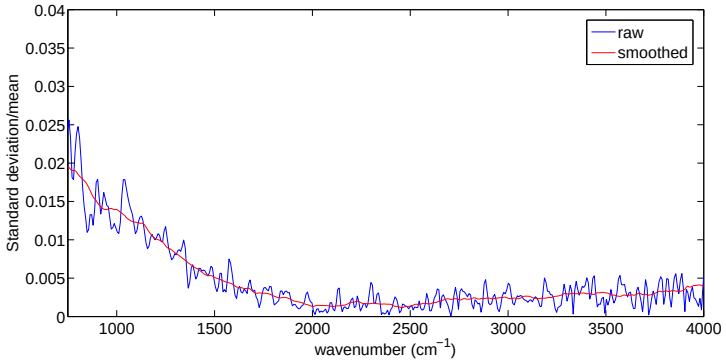

Figure 5.3.2: *The relative reproducibility error for the platinum ribbon signal measured with the DLaTGS detector and KBr beamsplitter. The relative error is below 2% for the calibrated range given by* $1000 - 2500\,cm^{-1}$.

The relative error can be written as

$$\frac{dI_{BB}}{I_{BB}} \approx \frac{100hc\tilde{\nu}}{k_B T}\frac{dT}{T}. \tag{5.18}$$

The temperature error is proportional to the wavenumber and increases from 0.5% at $1000\,\mathrm{cm}^{-1}$ to 5% at $13000\,\mathrm{cm}^{-1}$.

- The interpolation of the spectral emissivity values with a linear function is responsible for an error of 1% for the entire range.

- The roughness of the platinum ribbon from Rowling [38] was slightly different from the ribbon used for calibration. The literature set was measured with a root mean square (RMS) peak-to-peak variation of 25 µm while measurements of the calibration ribbon gave RMS peak-to-peak values of 40 µm. Rowling also measured platinum ribbons which were glass-shot blasted to increase the roughness. From these measurements it is concluded that the relative change is largest at $1000\,\mathrm{cm}^{-1}$ and decreases to a stable value at $4000\,\mathrm{cm}^{-1}$. The error is estimated to be 2% at $1000\,\mathrm{cm}^{-1}$ since the roughness is still comparable to the calibration ribbon. The error decreases linearly and reaches a constant value of 0.5% at $4000\,\mathrm{cm}^{-1}$.

- According to Rowling the temperature measurements required for the spectral emissivity calculation were accurate up to 1%. The spectral error can be calculated with equation 5.18. The error increases from approximately 0% at $1000\,\mathrm{cm}^{-1}$to 1% at $13000\,\mathrm{cm}^{-1}$.

The spectral radiance of the halogen lamp measured at Philips OCM calibration laboratories has a relative error of 4% for the entire visible range.

Reproducibility errors are differences in measured signal when the same source is measured with the same settings on a different time or date. The measured signal $S_{\tilde{\nu}}$ is an average of individual measurements. These individual measurements in turn are an average of multiple spectra. In general the individual measurements are made immediately after each other. Their standard deviation divided by their average is a measure of the relative reproducibility error. The relative reproducibility error is investigated for all four parts of the spectrum calibrated with different detectors, beamsplitters and calibration sources. This relative error can be smoothed by averaging this error over a small wavenumber interval. The relative reproducibility errors of these four parts for the calibration measurements are shown in figures 5.3.2-5.3.5.

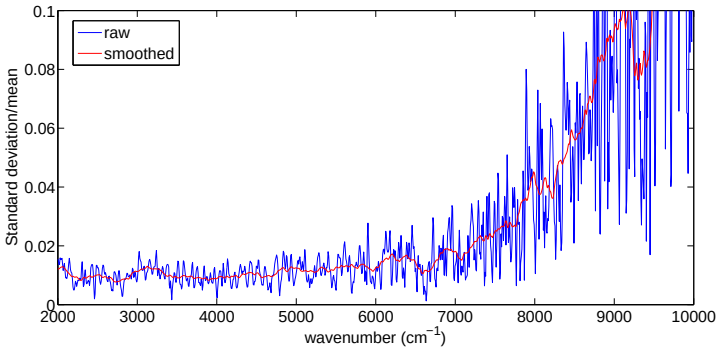

Figure 5.3.3: *The relative reproducibility error for the platinum ribbon signal measured with the MCT detector and CaF_2 beamsplitter. The relative error is increases from 1% at 2500 cm^{-1} to 2% at 7500 cm^{-1}. The error increases linearly to 6% at 8500 cm^{-1} because the radiance of the platinum ribbon is to weak to be measured with the MCT detector.*

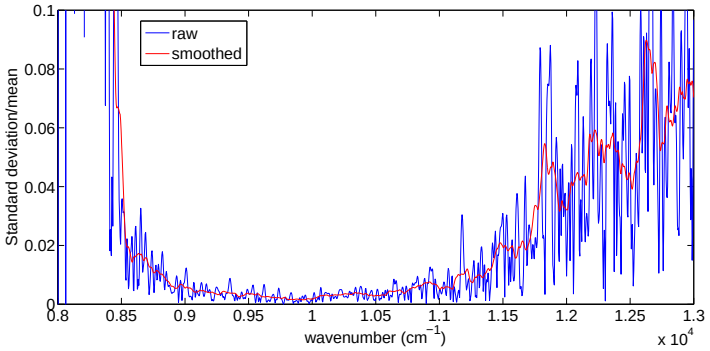

Figure 5.3.4: *The relative reproducibility error for the platinum ribbon signal measured with the Si detector and CaF_2 beamsplitter. The relative error is decreases from 6% at 8500 cm^{-1} to 1% at 8750 cm^{-1}. The increases linearly from 1% at 11000 cm^{-1} to 6.5% at 12821 cm^{-1} because the radiance of the platinum ribbon is to weak to be measured with the Si detector.*

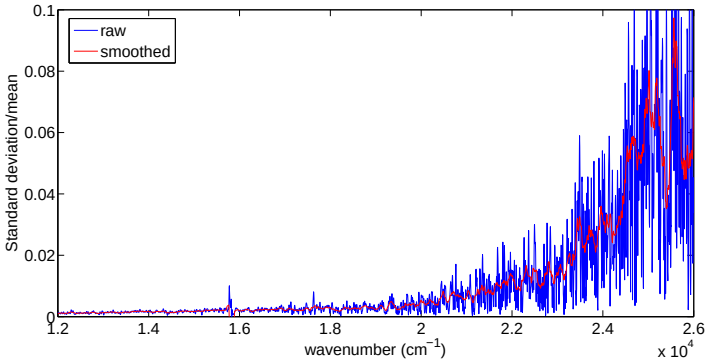

Figure 5.3.5: *The relative reproducibility error for the halogen lamp signal measured with the Si detector and CaF_2 beamsplitter. The relative error is approximately 0% at 19000cm^{-1} and increases to 2% at 24000cm^{-1}. The error then increases linearly to 7% at 26361cm^{-1} because the radiance of the halogen lamp is to weak to be measured with the Si detector and CaF_2 beamsplitter.*

The random noise of the measurements made with the DTGS and Si detector are approximately 0.5% for both the lamp and calibration measurements. For measurements made with the MCT detector the random noise is typically 1% of the total signal. It is assumed that this error disappears when the total spectrum is integrated.
Parts of the spectrum are calibrated with a detector and beamsplitter combination which are used at or beyond the limit of their intended range. For these spectral parts the errors will be higher. Above $7500\,\mathrm{cm^{-1}}$ the MCT detector is not able to measure the weak ribbon radiance accurately. The error is approximately 2% at this wavenumber. Due to a higher sensitivity the Si detector is able to measure this signal up to the visible part of the spectrum. However the Si detector can only measure accurately above $8750\,\mathrm{cm^{-1}}$ where the error is reduced to 1%. The additional error is estimated to be 6% at $8500\,\mathrm{cm^{-1}}$. A similar contribution is added between 11000 and $12821\,\mathrm{cm^{-1}}$ because the Si detector can not measure the radiance of the ribbon accurately above $11000\,\mathrm{cm^{-1}}$. The error of the ribbon measurement increases from 1% at $11000\,\mathrm{cm^{-1}}$ to 6.5% at $12821\,\mathrm{cm^{-1}}$. At $24000\,\mathrm{cm^{-1}}$ the signal to noise ratio of the measurements made with the Si detector is decreasing. The last part of the visible spectrum is expected to be measured with an error of 2% at $24000\,\mathrm{cm^{-1}}$ which increases to 7% at $26361\,\mathrm{cm^{-1}}$.

Not uniform integration errors are caused because radiation reaching certain areas of the sphere surface can not leave the integrating sphere with two reflections. The path from these areas towards the focus point of the detector on the baffle can not be reached. The radiation therefore always requires at least one additional reflection. This decreases the signal strength from the radiation radiated in these solid angles. The contribution from these areas to the total signal is decreased by the sphere reflectance. The main contribution of the radiance of the platinum ribbon is radiated normal to the surface of the longest part of the ribbon. The halogen lamp mainly radiates normal to the axis of the coil and the single salts lamps mainly radiate normal to the axis of the cylinder. The non uniform integration error is neglected in the analysis since both the calibration sources and the lamps are mounted in the sphere in a way that nearly all radiative output is facing these less sensitive parts of the sphere. Almost all radiation therefore requires at least three reflections. It is assumed that the contribution of the radiation emitted in the solid angles that can reach the detector in two reflections is negligible.

Errors in the conduction calculation are caused by absorption of radiation by the holder while the calculation only includes a conduction term. Emission of the holder can be neglected at temperatures between $300-350\,\mathrm{K}$. The total errors in the calculation are estimated to be 20%.

Chapter 6

Experimental results

In this chapter the experimental results for the four single salts lamps are presented. All lamp spectra are calibrated. For all spectra a short energy balance is made and an estimate of the line and continuum radiation is given. In this work continuum radiation is defined as the sum of thermal radiation and plasma continuum radiation. A qualitative estimate of the temperature of the plasma at the lamp axis is obtained by comparing the spectral power of several mercury lines. Switch off measurements were made to separate the thermal radiation from the plasma radiation. After that the conduction losses per unit length are estimated with a powerscan. A short introduction to these switch-off measurements is given first. After that the Jack-Koedam theory is briefly summarized.

Switch-off measurements are quick low resolution measurements made after switching off the lamp. The plasma radiation will disappear much faster than the thermal radiation of the discharge tube. At a certain moment all plasma radiation has disappeared and only thermal radiation is measured. The spectra containing only thermal radiation are extrapolated back to the time of switching off the lamp. The result is the thermal radiation emitted by a burning lamp. The ratio of the extrapolated curve to a reference measurement made when the lamp was still on is multiplied with the calibrated spectrum to obtain the calibrated thermal radiation. It is assumed that the radiation emitted in a wavenumber interval decays with an exponential function. For every interval a different time constant $\tau_{\tilde{\nu}}$ will be fitted with

$$I\left(\tilde{\nu},t\right) = I\left(\tilde{\nu},0\right) exp\left(\frac{-t}{\tau_{\tilde{\nu}}}\right). \tag{6.1}$$

Jack and Koedam [7] estimated the conduction losses in a lamp by measuring lamps at multiple input powers. They introduce a position in the lamp which indicates the boundary of the hot centre and the cooler outer mantle, r_0, where the cumulative dissipated power is approximately equal to the input power. From this point on only absorption will occur. The radiation losses at the wall can then be written as

$$P_{rad}\left(R\right) = \alpha\left(P_{dis} - P_{cond}\left(r_0\right)\right). \tag{6.2}$$

with α the transmission of the outer mantle. In this work only the plasma radiation measured in the visible and infrared will be included in the $P_{rad}\left(R\right)$ term. The thermal radiation from the discharge tube is subtracted from the infrared contribution. The ultraviolet radiation can not be measured and is therefore not included. The $P_{cond}\left(r_0\right)$ term is an estimate of the conduction losses of the hot centre to the outer mantle. The P_{dis} term can be written as

$$P_{dis} = \frac{P_{in} - P_{el}}{L_{el}}, \tag{6.3}$$

with P_{in} the input power, P_{el} the electrode losses and L_{el} the electrode separation. The electrode losses are estimated with 10% of the nominal input power.

	Energy(W)	Error(W)
IR (0.78-10 µm)	43.2	2.3
Visible (380-780 nm)	13.8	0.6
Far IR (>10 µm	0.7	0.1
Conduction	3.9	0.8
Total	62	4
Input	70.5	0.1

Table 6.1.1: *The energy balance of the pure mercury lamp. About 9 W of input power is unaccounted for. The discrepancy is most likely caused because the ultraviolet radiation is not measured. For mercury these ultraviolet contributions are significant.*

6.1 Hg

In this section the calibrated spectrum, the switch-off measurements and the powerscan are shown for the Hg lamp. This lamp will be used as a reference for the other single salt lamps since mercury is still the main ingredient in these lamps.

6.1.1 Calibrated spectrum

The calibrated spectrum for the Hg lamp is shown in figure 6.1.1. An output energy balance is given in table 6.1.1. Continuum radiation is defined as thermal radiation and plasma continuum radiation. The continuum radiation can be obtained by interpolating the line radiation. In certain cases the continuum interpolation exceeds the lamp radiation. In those cases the continuum radiation is set to the spectral power of the complete spectrum. The continuum radiation is shown in figure 7.1.2. The total amount of continuum radiation is 46 W. The continuum radiation can be subtracted from the total spectrum to obtain the line radiation. The total amount of line radiation is approximately 11 W. The energy in the mercury lines is shown in table 6.1.2. The contributions of the most important lines in this spectrum are in the order of $2-3$ W. These lines are the 404, 436 and the 546 nm lines. The energy balance can not account for all of the input energy. The ultraviolet could not be measured. This spectral part contains the energy which was unaccounted for. Most of the unaccounted energy is emitted via the 185 and 254 nm lines.

A similar energy balance was made by Jack and Koedam [7] for a 400 W mercury lamp. Their lamp has a height to diameter ratio of about 4.5 while the single salt lamp has a height to diameter ratio around 1. The conduction losses for the 400 W lamp are therefore larger than for the single salt lamp. Jack and Koedam measured 15 % of visible radiation and 67 % of infrared radiation. The visible output of the mercury reference lamp is roughly 20 % and the infrared output is approximately 62 %.

6.1.2 Thermal radiation

In this section the thermal radiation of the discharge tube is estimated with the switch-off procedure. The results of the switch-off measurements are shown in figure 6.1.2. For wavenumbers above 2000 cm^{-1} the calibrated spectrum is multiplied with the ratio of the extrapolated signal to the reference signal. Below this wavenumber it is assumed that all radiation is thermal radiation. The total amount of thermal radiation is estimated as (26 ± 2) W. This is 37 % of the input power. Jack and Koedam [7] measured 52 % of thermal radiation from their 400 W mercury lamp. These results are different because the 400 W lamp has relatively larger conduction losses because of the higher height to diameter ratio. The infrared discharge radiation is 24 % for the reference lamp and 15 % for the 400 W lamp. These differences are caused by the larger pressure in the reference lamp. As a result the amount of Bremsstrahlung radiation is much larger in the reference lamp. Most of the Bremsstrahlung radiation is radiated as infrared radiation.

Wavelength(nm)	Energy (W)
404	1.5
407	0.1
436	2.6
546	2.9
577	0.8
579	0.8
1014	0.6
1129	0.2
1359	0.1
1369	0.2
1395	0.1
1531	0.1
1692	0.1
1707	0.1

Table 6.1.2: *The energy of the most important atomic lines for the pure mercury lamp. The most important lines are the* 404, 436 *and* 546 *nm lines.*

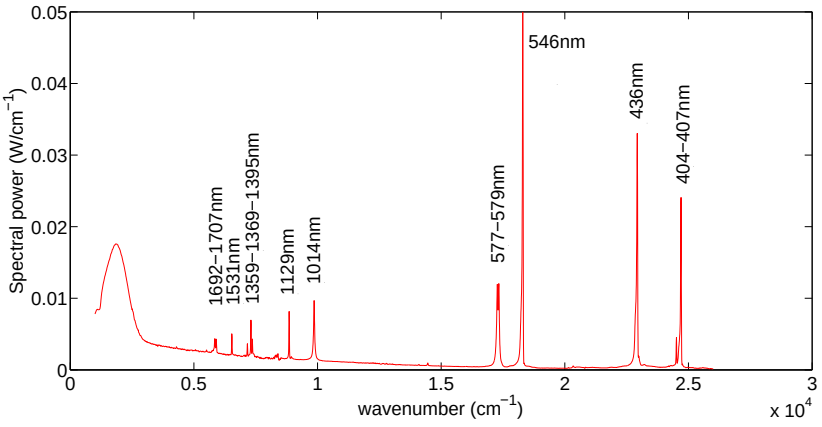

Figure 6.1.1: *The infrared and visible spectrum of the pure mercury lamp in the range* $1000 - 26381\ cm^{-1}$ *are shown. The wavelength of the mercury lines are shown in black.*

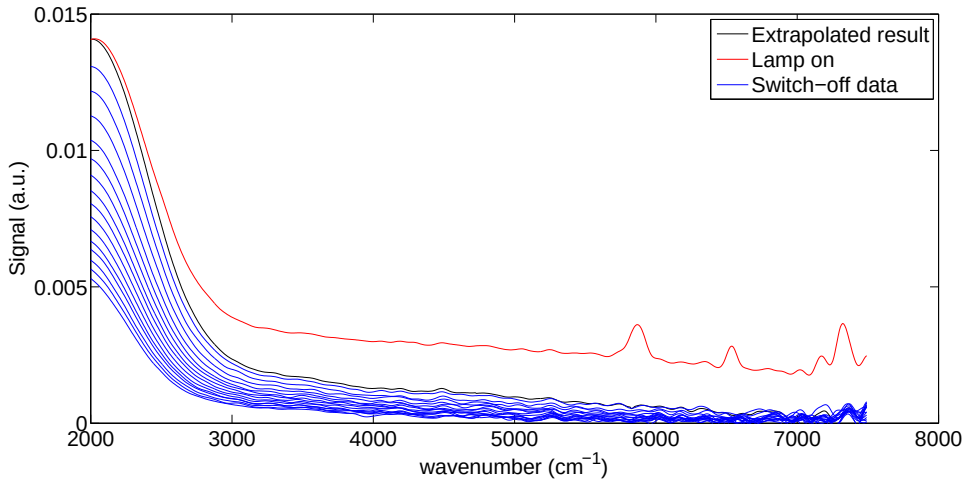

Figure 6.1.2: *The results of the switch-off measurements for the mercury lamp. Below* 2000 cm^{-1} *all radiation is assumed to be thermal radiation. Above this wavenumber the ratio of the extrapolated to the reference curve is multiplied with a calibrated spectrum. The total thermal radiation is* (26 ± 2) *W.*

6.1.3 Power scan

In this section an estimate is made for the conduction losses. The result for the power scan is shown in figure 6.1.3. The proportionality constant α is equal to 0.53. This constant would have a value closer to one if the ultraviolet could also be measured. The conduction losses from the hot centre to the colder outer mantle are estimated as (10 ± 2) W.

6.2 Hg+NaI

In this section the calibrated spectrum, the switch-off measurements and the powerscan are shown for the sodium iodide single salt lamp.

6.2.1 Calibrated spectrum

The calibrated spectrum for the sodium iodide lamp is shown in figure 6.2.1. For a comparison with the pure mercury lamp both spectra have been plotted in the same graph. This plot is shown in figure 6.2.2. The decreased radiation from the 546 and 436 nm mercury lines is a clear indication that the axis temperature of the single salt lamp is much lower than that of the mercury lamp. The differences in the height of the thermal radiation peak at 2000 cm^{-1} indicates that the wall temperature of the sodium lamp is lower than that of the mercury lamp. The plasma continuum radiation is similar for both lamps because the sodium pressure is negligible in comparison with the mercury pressure. The amount of radiated visible energy is increased significantly due to the sodium D-lines. The strong van der Waals broadening of the red wing provides excellent color rendering in that part of the spectrum. The color rendering of the blue part of the spectrum is barely affected by adding sodium.

An output energy balance is shown in table 6.2.1. The most important conclusion is that the energy balance can account for the total input power. The ultraviolet contribution can be neglected. Jack and Koedam [7] for example measured only 2 W of ultraviolet radiation from a 400 W lamp containing sodium and mercury. A fit was made to separate the continuum radiation from the line radiation. This fit is shown in figure 6.2.3. The total amount of continuum radiation is 42 W. The continuum radiation for the mercury lamp and the sodium iodide single salt lamp is

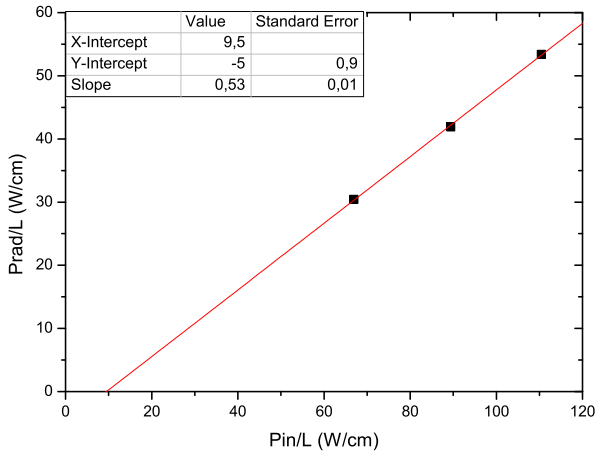

Figure 6.1.3: *The powerscan of the Hg lamp. The proportionality constant α is given by* 0.53 *and the conduction losses are* (10 ± 2) *W.*

similar. The higher thermal radiation for the mercury lamp explains the small difference between both lamps. The total line radiation is estimated with 26 W. An estimate of the contributions of the most important atomic transitions is shown in table 6.2.2. From these tables it can be concluded that the difference between the visible output of the single salt lamp and the mercury lamp is solely caused by the sodium D-lines. The small difference in infrared output is caused by the higher thermal radiation losses in the mercury lamp.

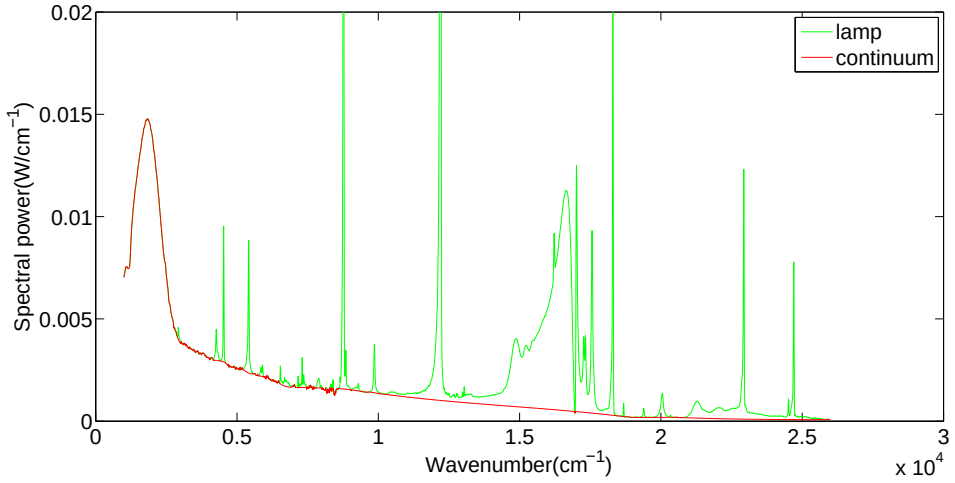

Figure 6.2.3: *The continuum radiation of the single salt lamp containing sodium iodide and mercury. The total amount of continuum radiation is* 42 *W. The total amount of line radiation is approximately* 26 *W.*

6.2.2 Thermal radiation

The thermal radiation of the discharge tube is estimated with the switch-off procedure. The results are shown in figure 6.2.4. For wavenumbers above 2000 cm^{-1} the thermal radiation is obtained

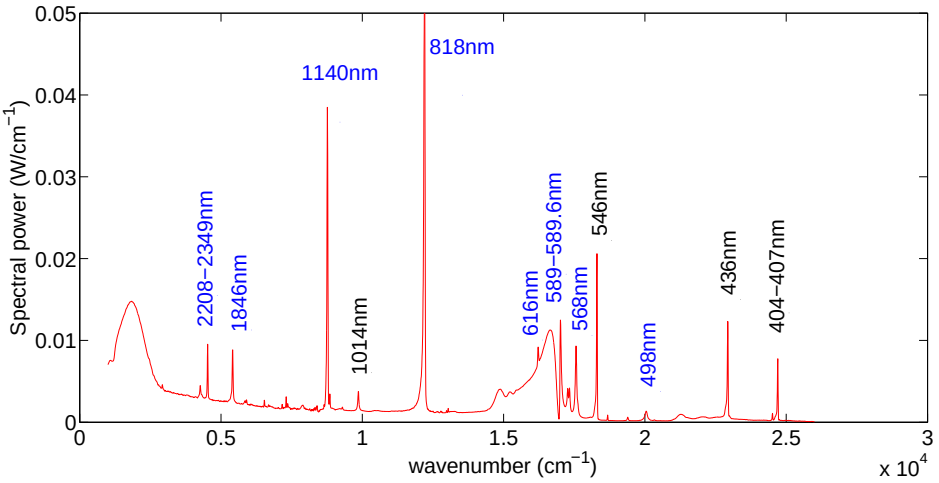

Figure 6.2.1: *The calibrated spectrum for the single salt lamp containing sodium iodide and mercury. Sodium lines are labeled in blue and mercury lines are labeled in black. The sodium* 589 *and* 589.6 *nm lines are an example of strong quasi static broadening.*

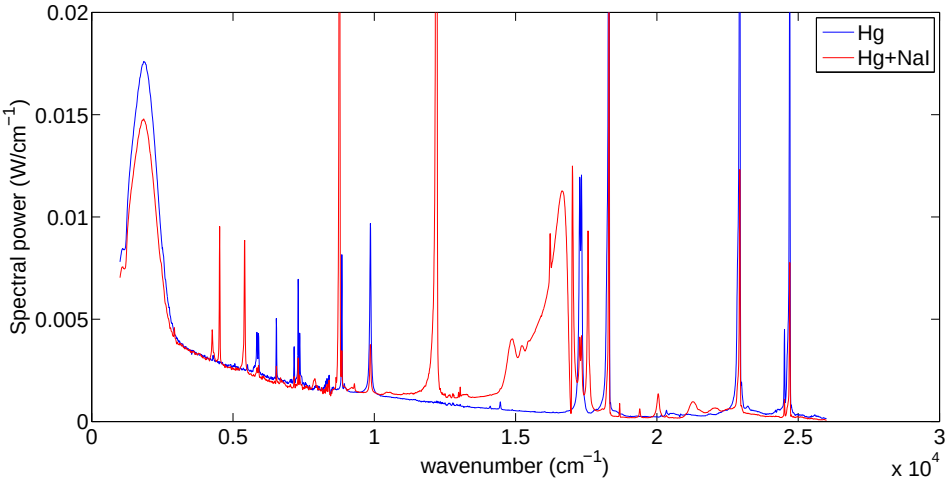

Figure 6.2.2: *The spectra for the single salt lamp containing sodium iodide and mercury and the pure mercury lamp. The amount of thermal radiation of the Hg lamp is higher than the sodium lamp; its wall temperature must be larger. The amount of plasma continuum radiation is similar for both lamps. The lamp containing sodium emits much more visible radiation than the mercury lamp because of the resonant sodium D-lines. The decreased emission from the* 546 *and* 436 *nm mercury lines indicates that the axis temperature decreased significantly.*

	Energy(W)	Error(W)
IR (0.78-10 µm)	45.3	2.7
Visible (380-780 nm)	22.7	0.9
Far IR (>10 µm)	0.7	0.1
Conduction	3.7	0.7
Total	73	5
Input	71.2	0.1

Table 6.2.1: *The energy balance for the single salt lamp containing sodium iodide and mercury. For such a lamp the ultraviolet contributions can be neglected since the axis temperature is much lower in comparison with a mercury lamp. The total energy is equal to the input power within the experimental error.*

Radiating particle	Wavelength(nm)	Energy(W)
Hg	404	0.4
Hg	436	0.9
Na	498	0.2
Hg	546	0.9
Na	568	0.8
Hg	577	0.2
Hg	579	0.3
Na	589	13.9
Na	616	0.1
Na	818	4.3
Hg	1014	0.2
Na	1140	1.7
Na	1846	0.4
Na	2208	0.2
Na	2349	0.1

Table 6.2.2: An estimate of the radiated energy per line. The most important lines are the sodium D-lines. Other strong lines are the 818 and 1140nm lines.

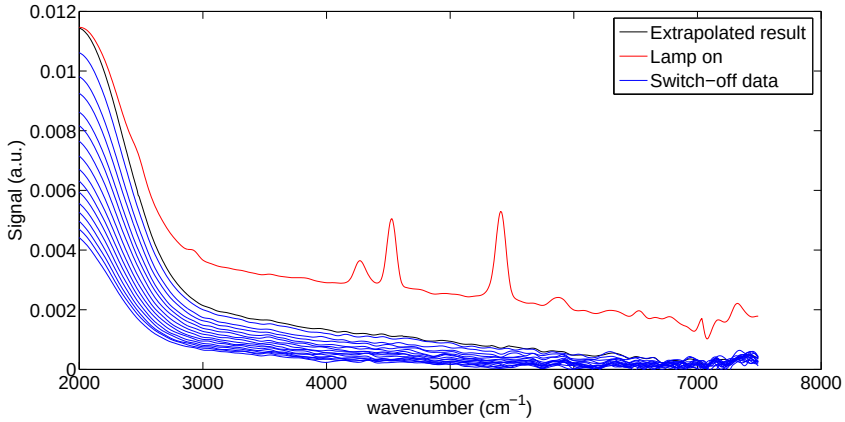

Figure 6.2.4: *The switch-off measurements for the single salt lamp containing sodium iodide and mercury. Below* 2000 cm^{-1} *all radiation is assumed to be thermal radiation. Above this wavenumber the ratio of the extrapolated to the reference curve is multiplied with a calibrated spectrum. The total thermal radiation is* (23 ± 2) *W.*

by multiplying the calibrated spectrum with the ratio of the extrapolated curve to the reference measurement. Below 2000 cm^{-1} all radiation is assumed to be thermal radiation. The total thermal radiation is (23 ± 2) W.

6.2.3 Power scan

In this section an estimate is made of the conduction losses. The results of the powerscan are shown in figure 6.2.5. The proportionality constant α is given by 0.84. The conduction losses from the hot centre to the colder outer mantle are estimated by (10 ± 2) W. The axis temperature of the sodium iodide lamp is lower in comparison to the mercury lamp. The collisional conduction is therefore decreased. This reduction is compensated by the chemical transport of energy via the sodium ionization reactions. Since α for the sodium iodide lamp is higher in comparison with the mercury lamp less radiation is absorbed in the outer mantle. The total heat flux to the wall therefore is lower than for the mercury lamp hence the wall temperature is lower as well.

6.3 Hg+TlI

In this section the calibrated spectrum, the switch-off measurements and the powerscan are shown for the thallium iodide single salt lamp.

6.3.1 Calibrated spectrum

The calibrated spectrum for the thallium iodide single salt lamp is shown in figure 6.3.1. A comparison is made with the mercury lamp by plotting both curves simultaneously. This plot is shown in figure 6.3.2. The only mercury line which is still visible in the thallium lamp is the 546 nm line. The axis temperature of the thallium lamp thus decreased considerably in comparison with the mercury lamp. The decrease in the peak at 2000 cm^{-1} shows that the wall temperature of the thallium lamp is lower in comparison with the mercury lamp. The spectrum of the thallium lamp contains much more continuum radiation. The radiation is most likely radiation from photo dissociation of TlI [46]. The dissociative recombination of the TlI ions with free electrons will result in highly excited Tl neutrals. The continuum seems to cover the spectral range from 3000 to 22000 cm^{-1}. The strong continuum radiation provides excellent color rendering in almost the

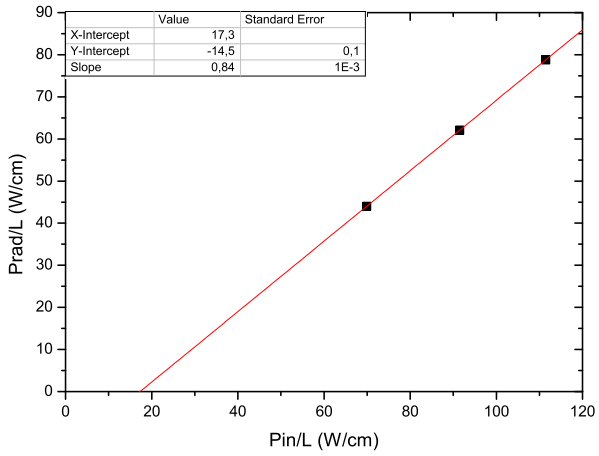

Figure 6.2.5: *The powerscan of the sodium iodide single salt lamp. The proportionality constant is given by* $\alpha = 0.84$. *The conduction losses are* (10 ± 2) *W.*

complete visible range. A drawback of such a strong and widespread continuum is a low luminous efficacy.

An output energy balance is shown in table 6.3.1. For this lamp the experimentally determined energy balance is also in agreement with the input power. A fit is made to separate the continuum radiation from the line radiation. This fit is shown in figure 6.3.3. The total amount of continuum radiation is estimated with 63 W. Based on this fit it is concluded that almost al of the radiation is continuum radiation. The amount of continuum radiation is large because the main contribution to the spectrum is from photo dissociation of TlI. The contribution from atomic lines is only 5 W. The photo dissociation radiation is included in the total continuum radiation. It is difficult to determine the difference between the photo dissociation radiation and the red wing of the atomic lines. This is especially difficult for the 535 nm thallium line radiation. This line is subject to strong van der Waals broadening in its red wing. An estimate of the contributions of the most important atomic lines is given in table 6.3.2. The contributions of the strongest lines are in the order of 1 W. These lines are the 535, 1151 and 1301 nm lines.

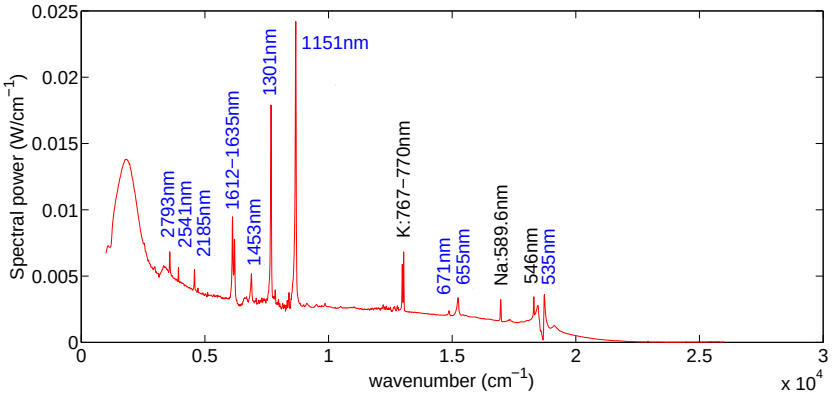

Figure 6.3.1: *The calibrated spectrum of the thallium iodide single salt lamp. The thallium lines are labeled in blue. The other lines which can be observed are potassium, sodium and mercury lines. The thallium spectrum contains a self reversed line at* 535 *nm.*

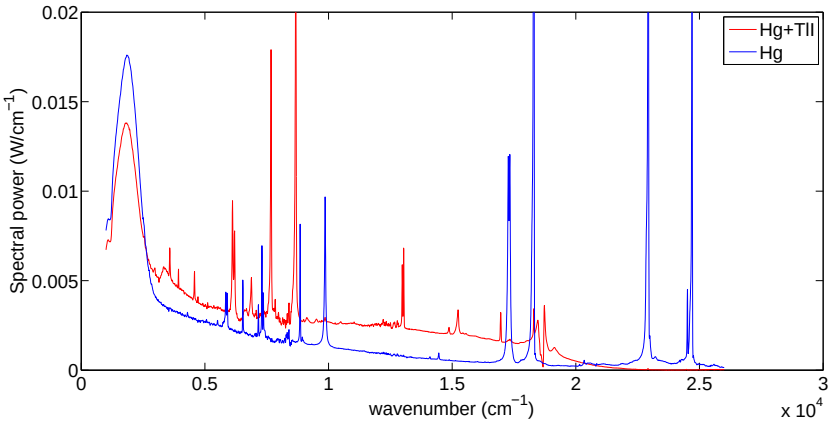

Figure 6.3.2: *The spectra of the mercury lamp and the thallium iodide single salt lamp in the same figure. Most of the mercury lines are no longer visible therefore the axis temperature of the single salt lamp is very low. The thermal radiation of the thallium lamp emitted by the discharge tube is lower in comparison with the mercury lamp. The wall temperature has thus decreased as well. The most important difference is the large amount of continuum radiation present in the thallium lamp spectrum. This radiation is most likely photo dissociation radiation from TlI.*

	Energy(W)	Error(W)
IR (0.78-10 µm)	53.9	3.0
Visible (380-780 nm)	13.7	0.6
Far IR (>10 µm)	0.7	0.1
Conduction	3.7	0.7
Total	72	4
Input	70.1	0.1

Table 6.3.1: *The energy balance for the thallium iodide single salt lamp. The ultraviolet contribution is negligible for this lamp since the axis temperature is very low. The total input power is equal to the input power within experimental error.*

Radiating particle	Wavelength(nm)	Energy(W)
Tl	535	1.0
Na	589	0.1
K	770	0.2
Tl	1151	1.4
Tl	1301	0.8
Tl	1443	0.1
Tl	1612	0.2
Tl	1635	0.3
Tl	2185	0.1
Tl	2793	0.1

Table 6.3.2: *The estimated contributions to the energy balance of the most important atomic lines. The atomic radiation is not very important in the thallium lamp. The biggest contributions are from the* 535, 1151 *and* 1301 *nm thallium lines. These contributions are in the order of* 1 *W.*

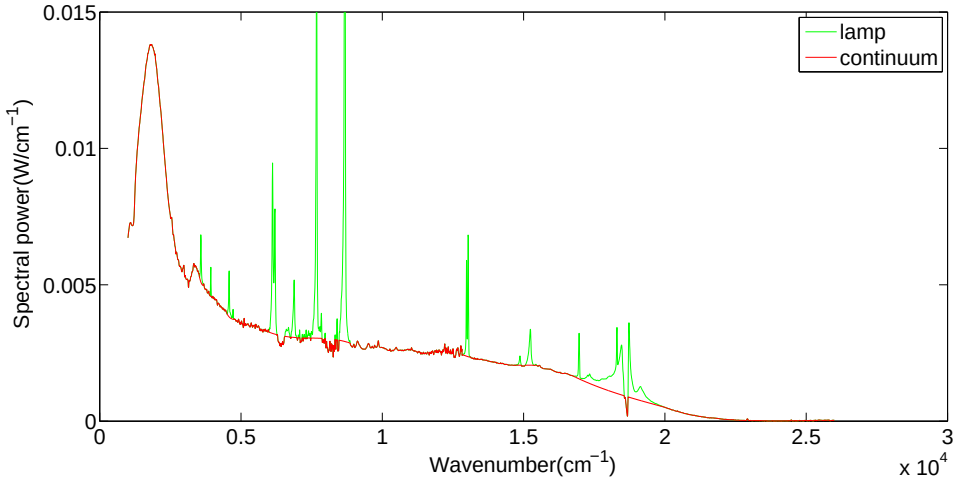

Figure 6.3.3: *The continuum radiation for the thallium iodide single salt lamp. Continuum radiation includes molecular radiation, thermal radiation and Bremsstrahlung. The total amount of continuum radiation is* 63 *W. The atomic radiation only contributes* 5 *W to the energy balance.*

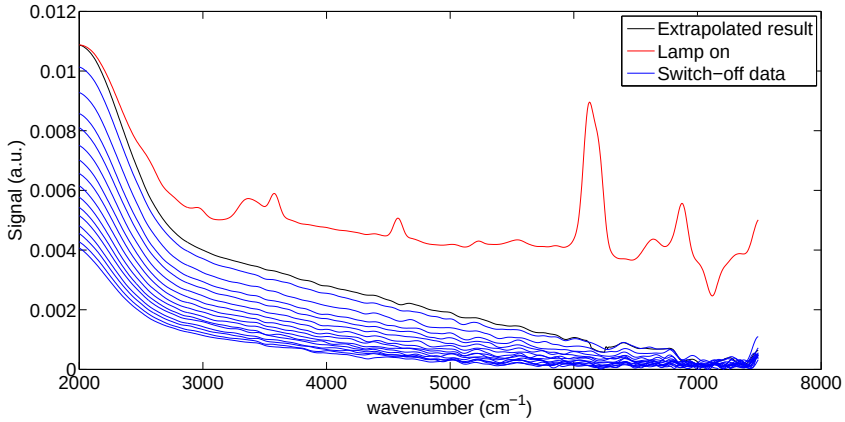

Figure 6.3.4: *The results of the switch-off measurements for the thallium iodide single salt lamp. Below* 2000 cm^{-1} *all radiation is assumed to be thermal radiation. Above this wavenumber the ratio of the extrapolated to the reference curve is multiplied with a calibrated spectrum. The total thermal radiation is* (26 ± 2) *W.*

6.3.2 Thermal radiation

In this section the thermal radiation of the discharge tube is estimated with the switch-off procedure. The results are shown in figure 6.3.3. For wavenumbers above 2000 cm^{-1} the thermal radiation is estimated by multiplying the calibrated spectrum with the ratio of the extrapolated curve to the reference measurement. For wavenumbers above 1000 cm^{-1} and below 2000 cm^{-1} it is assumed that all radiation is thermal radiation. The emitted thermal energy is (26 ± 2) W. It seems as if the energy above 2500 cm^{-1} is overestimated when compared to the mercury discharge. According to figure 6.3.2 the discharge tube of the mercury lamp radiates more thermal energy between 1000 and 2500 cm^{-1} but has a smaller contribution above 2500 cm^{-1}. A cooler discharge wall only emits more radiation in the near infrared if the emissivity of the wall increases. The emissivity of the wall can change due to wall blackening. This is a process where tungsten from the electrodes is deposited on the wall. The discharge tube of the thallium iodide lamp appeared to be slightly darker than the mercury discharge tube. Thus wall blackening possibly plays a role.

The infrared plasma radiation of the thallium iodide lamp is approximately 28 W. The infrared plasma radiation from the mercury and the sodium iodide lamp amounts to 17 and 22 W, respectively. The difference is caused by the strong photo dissociation continuum. This strong continuum in the infrared decreases the luminous efficacy.

6.3.3 Power scan

In this section an estimate of the conduction losses is made. The results of the powerscan are shown in figure 6.3.5. The proportionality constant α is given by 0.84. The resulting conduction losses from the hot arc to the colder mantle are (13 ± 2) W. The conduction losses in the thallium lamp are larger in comparison with mercury lamp because of additional energy transported via chemical reactions.

6.4 Hg+InI

In this section the calibrated spectrum, the switch-off measurements and the powerscan are shown for the indium iodide single salt lamp.

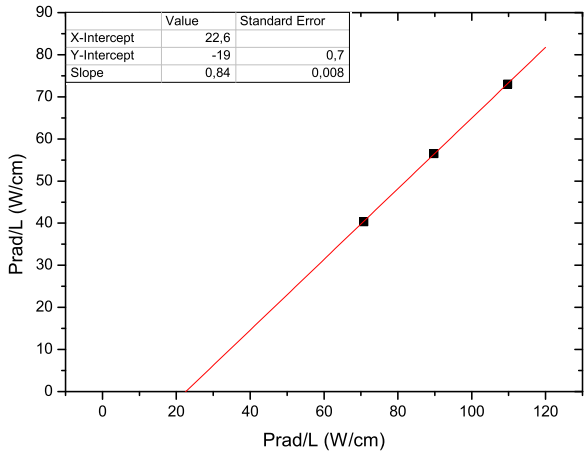

Figure 6.3.5: *The results of the powerscan of the thallium iodide single salt lamp. The proportionality constant is given by* $\alpha = 0.84$*. The conduction losses are* (13 ± 2) *W.*

6.4.1 Calibrated spectrum

The calibrated spectrum of the indium iodide single salt lamp is shown in figure 6.4.1. A comparison can be made with the mercury lamp by showing both spectra in the same figure. This plot is shown in figure 6.4.2. The indium spectrum is similar to the mercury spectrum. The spectral power of the mercury lines has decreased a little which implies that the axis temperature is slightly lower. The wall temperature of both discharges is similar since the spectral power at $2000\,\mathrm{cm^{-1}}$ is equal. At this wavenumber the emissivity of the discharge tube is close to one which means almost all emitted radiation is thermal radiation at this wavenumber. The largest difference between the discharges is the presence of a continuum between 2500 and $8000\,\mathrm{cm^{-1}}$. From the typical shape of this continuum is concluded that this difference is caused by wall blackening. The tungsten from the electrode is deposited on the discharge tube which alters the emissivity of the material. A comparison of the indium iodide discharge tube with the mercury discharge tube indeed shows that the wall is much darker.

A simple energy balance is shown in table 6.4.1. The energy that is accounted for is not equal to the input power. Since the mercury part of the indium iodide lamp is similar to the mercury lamp the ultraviolet radiation from the mercury lines will also be present in the indium iodide lamp. Besides the ultraviolet radiation from mercury there will be a small contribution from the indium 256, 271, 303 and 325 nm lines as well.

A fit is made to separate the continuum radiation from the line radiation. This fit is shown in figure 6.4.3. The total amount of continuum radiation is 53 W. The continuum radiation of the indium iodide lamp is higher in comparison with the mercury lamp due to wall blackening. The total line radiation amounts to $13\,W$. The contributions for the most important atomic lines are shown in table 6.4.2. The contributions of the strongest atomic lines are in the order of $1 - 2$ W. These lines are the 404, 436 and 546 nm lines.

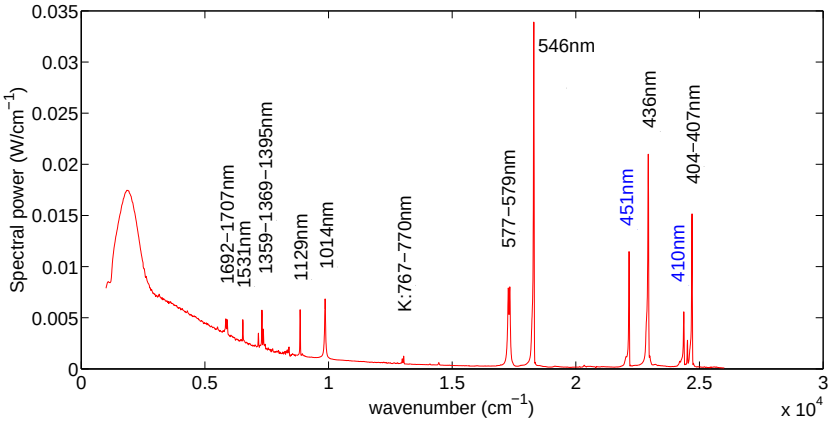

Figure 6.4.1: *The calibrated spectrum for the indium iodide single salt lamp. The indium lines are labeled in blue. The mercury and potassium lines are labeled in black. The indium lines only make a small contribution to the total spectrum.*

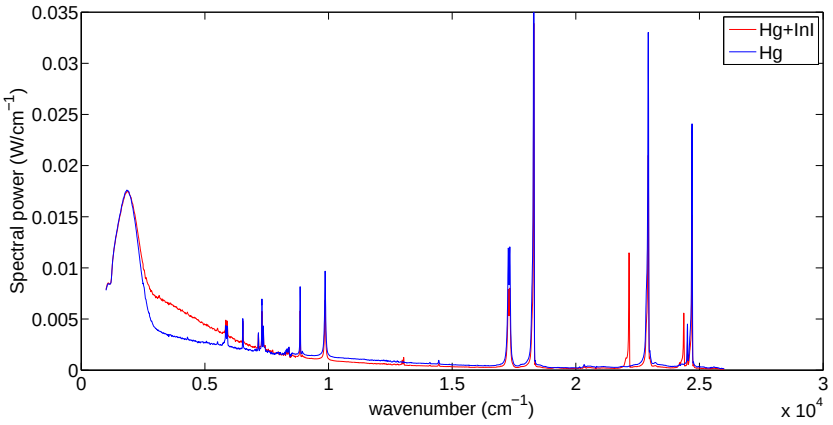

Figure 6.4.2: *The calibrated spectra for the mercury and the indium iodide single salt lamp. The spectral power of the mercury lines has decreased which means the axis temperature has dropped. The thermal radiation peak at* $2000\,\mathrm{cm}^{-1}$ *is similar which indicates the wall temperatures are approximately equal. The thermal radiation of the discharge tube in the indium iodide lamp is larger because of wall blackening. Tungsten from the electrodes has been deposited on the wall of the discharge tube which alters the emissivity of the wall.*

	Energy(W)	Error(W)
IR (0.78-10 µm)	50.5	2.5
Visible (380-780 nm)	9.5	0.4
Far IR (>10 µm)	0.7	0.1
Conduction	4.6	0.9
Total	65	4
Input	70.9	0.1

Table 6.4.1: *The energy balance of the indium iodide lamp. The total energy does not match with the input power. The ultraviolet contribution was not measured. This contribution can not be neglected for the indium iodide lamp.*

Radiating particle	Wavelength(nm)	Energy(W)
Hg	404	0.8
Hg	407	0.1
In	410	0.5
Hg	436	1.5
In	451	0.6
Hg	546	1.8
Hg	577	0.5
Hg	579	0.5
Hg	1014	0.4
Hg	1129	0.1
Hg	1359	0.1
Hg	1369	0.1
Hg	1692	0.1
Hg	1707	0.1

Table 6.4.2: *The contributions to the energy balance of the most important atomic lines. The* 404, 436 *and* 546 *nm lines are the most important lines in the spectrum. These contributions are in the order of* $1-2$ *W.*

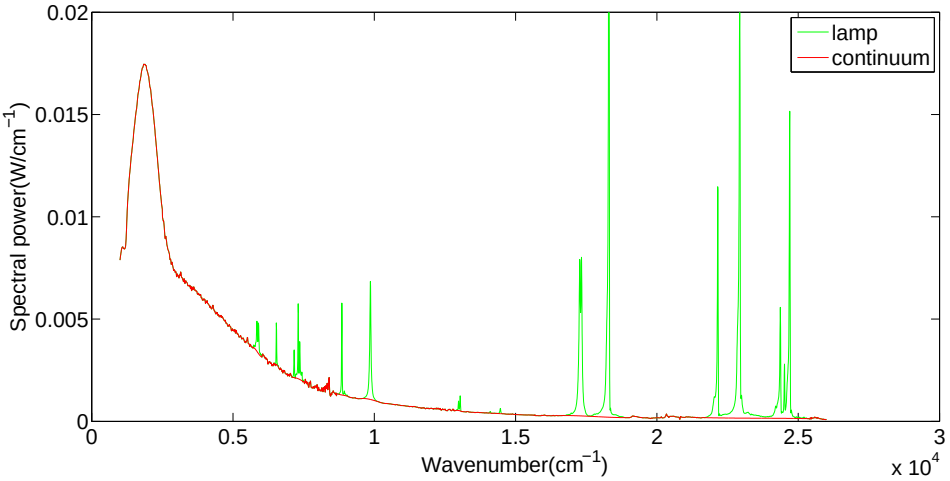

Figure 6.4.3: *The continuum radiation for the indium iodide single salt lamp. The total amount of continuum radiation is* 53 *W. The total amount of line radiation is* 13 *W.*

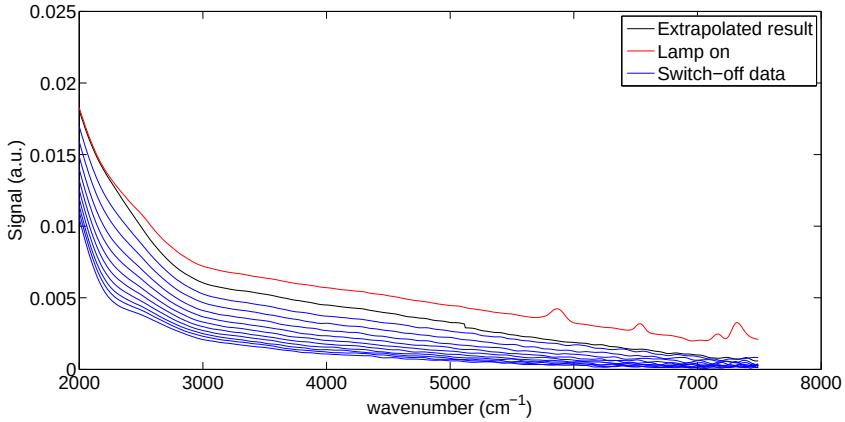

Figure 6.4.4: *The results of the switch-off measurements of the indium iodide lamp. Below* 2000 cm^{-1} *all radiation is assumed to be thermal radiation. Above this wavenumber the ratio of the extrapolated to the reference curve is multiplied with a calibrated spectrum. The total amount of thermal radiation is* (38 ± 4) *W.*

6.4.2 Thermal radiation

In this section the thermal radiation of the discharge tube is estimated with the switch-off procedure. The results are shown in figure 6.4.4. For wavenumbers above 2000 $\mathrm{cm}^{-1}$the energy is estimated by multiplying the calibrated spectrum at regular settings with the ratio of the extrapolated curve to the reference curve at switch-off settings. Below 2000 cm^{-1} al radiation is assumed to be thermal radiation. For this range the calibrated spectrum at regular settings is integrated. The total thermal energy is (38 ± 4) W. The large amount of thermal radiation is caused by severe wall blackening.

6.4.3 Power scan

In this section an estimate of the conduction losses is made. The results of the powerscan are shown in figure 6.4.5. The proportionality constant α is given by 0.42. The conduction losses from the hot centre to the outer mantle are given by (9 ± 2) W. The wall temperature has a comparable temperature as the discharge tube of the mercury lamp but radiates more thermal energy. The heat flux to the wall must therefore be larger. This heat flux to the wall is fed by strong absorption in the outer mantle.

6.5 Complete energy balance

In this section the results of the four single salt lamps are summarized in one table. These results are shown in table 6.5.1. All relevant formulas will be shown as well. The total input power P_{in} is divided among the electrodes P_{el} and the discharge P_{dis} as

$$P_{in} = P_{el} + P_{dis}. \tag{6.4}$$

The electrode losses are estimated with 10% of the input power. The power in the discharge is lost by radiation $P_{rad}(r_0)$ and by non-radiative processes $P_{non,rad}$ as

$$P_{dis} = P_{non,rad} + P_{rad}(r_0). \tag{6.5}$$

The non-radiative processes are estimated with the conduction losses at the boundary between the hot centre and colder outer mantle determined in the powerscan. The radiation losses in the

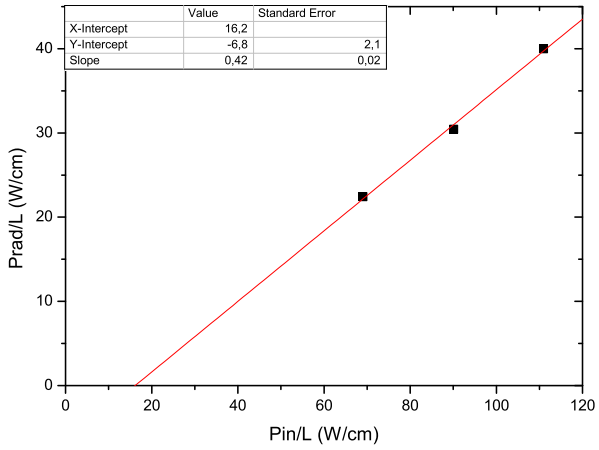

Figure 6.4.5: *The results of the powerscan of the indium iodide single salt lamp. The proportionality constant α is given by* 0.42 *and the conduction losses are given by* (9 ± 2) *W.*

discharge can be related to the measured radiation losses $P_{rad}(R)$ as

$$P_{rad}(R) = \alpha P_{rad}(r_0). \tag{6.6}$$

The amount of absorbed radiation P_{abs} can then be written as

$$P_{abs} = (1-\alpha) P_{rad}(r_0) = \frac{1-\alpha}{\alpha} P_{rad}(R). \tag{6.7}$$

The discharge radiation can be written as the sum of the spectral contributions

$$P_{rad}(R) = P_{dis,vis}(R) + P_{dis,UV}(R) + P_{dis,IR}(R). \tag{6.8}$$

An error is introduced since $P_{dis,UV}(R)$ is not measured.

The sum of the non-radiative losses, the electrode losses and the absorption of radiation should be dissipated as either thermal radiation P_{the}, or as conduction through the metallic wires $P_{cond,wires}$. To verify that this is indeed the case a parameter P_{Diff} is defined as

$$P_{Diff} = P_{non,rad} + P_{abs} + P_{el} - P_{the} - P_{cond,wires.} - P_{far,IR}. \tag{6.9}$$

In a correct energy balance this parameter is equal to zero. The thermal radiation is obtained from the powerscan. The thermal radiation in the far infrared $P_{far,IR}$ is not measured but is estimated by extrapolating the calibrated spectrum below 1000 cm^{-1}. The conduction through the metallic wires is estimated by calculating the heat flux through the holder based on the measured temperature difference between the top of the holder and the integrating sphere. The total energy which is accounted for in the experiment P_{tot} can be written as

$$P_{tot} = P_{dis,vis}(R) + P_{dis,IR}(R) + P_{the} + P_{far,IR} + P_{cond,wires}. \tag{6.10}$$

An analysis of table 6.5.1 shows that for all lamps both expressions for calculating $P_{rad}(r_0)$ provide similar results. The parameter P_{Diff} is not equal to zero within experimental error for every lamp. The mercury lamp has a value which is significantly above zero. This deviation is caused because the powerscan is not based on all discharge radiation. Since the ultraviolet contributions were not taken into account the powerscan can only provide an estimate of α and $P_{non,rad}$. The effective quantity plotted on the vertical axis of the powerscans is $P_{rad} - P_{uv}$. The

	Hg	Hg+NaI	Hg+TlI	Hg+InI
P_{in} (W)	70.5 ± 0.1	71.2 ± 0.1	70.1 ± 0.1	70.9 ± 0.1
P_{el} (W)	7.1	7.1	7.0	7.1
P_{dis} (W)	63.4	65.2	63.1	63.8
$P_{non,rad}$ (W)	9.5 ± 2	10.0 ± 2	13.0 ± 2	9.3 ± 2
$P_{rad}(r_0)_1$ (W)	53.9 ± 2	54.1 ± 2	50.1 ± 2	54.5 ± 2
$P_{rad}(r_0)_2$ (W)	58.4 ± 4	54.1 ± 6	50.0 ± 5.6	53.5 ± 6.9
α	0.53	0.84	0.83	0.42
P_{abs} (W)	25.5 ± 2	8.8 ± 2	8.1 ± 2	24.9 ± 2
$P_{dis,vis}$ (W)	13.8 ± 0.6	22.7 ± 0.9	13.7 ± 0.6	9.5 ± 0.4
$P_{dis,IR}$ (W)	17.0 ± 4	22.6 ± 5	28.2 ± 5	12.9 ± 6.5
P_{IR} (W)	43.2 ± 2.3	45.3 ± 2.7	53.9 ± 3.0	50.5 ± 2.5
P_{the} (W)	26.2 ± 2	22.7 ± 2	25.7 ± 2	37.6 ± 4
$P_{far,IR}$ (W)	0.7 ± 0.1	0.7 ± 0.1	0.7 ± 0.1	0.7 ± 0.1
$P_{cond,wires}$ (W)	3.9 ± 0.8	3.7 ± 0.7	3.7 ± 0.7	4.6 ± 0.9
P_{Diff} (W)	11.3 ± 6.9	-1.2 ± 5.7	-2.0 ± 6.8	5.2 ± 7.0
P_{tot} (W)	62 ± 4	73 ± 5	72 ± 4	65 ± 4

Table 6.5.1: *The energy balance for the four discharges. $P_{rad}(r_0)_1$ is calculated with equation 6.5 and $P_{rad}(r_0)_2$ is calculated with equation 6.6. Both ways of calculating $P_{rad}(r_0)$ provide the same result within experimental error. The P_{Diff} parameter is a measure of the internal consistency of the energy balance. For the mercury lamp this quantity is significantly larger than zero. This is related to not taking the ultraviolet into account in the powerscan. The transmittance calculated from the visible and the infrared radiation is thus not representative for the ultraviolet.*

result is that when the ultraviolet term can not be neglected it appears in the non-radiative and absorption losses. A similar problem occurs for the indium iodide lamp. Due to the lower axis temperature the ultraviolet contributions for this lamp are smaller. The estimate obtained from the powerscan is therefore more accurate for the indium iodide lamp.

To obtain better results for the mercury and the indium iodide lamp the powerscan has been recalculated with estimated ultraviolet contributions. The ultraviolet term is estimated by assuming that at each power, all unaccounted energy is ultraviolet radiation:

$$P_{UV}(R) = P_{in} - P_{tot}. \tag{6.11}$$

The new powerscan for the mercury lamp is shown in figure 6.5.1. The proportionality constant α is given by 0.67 and the conduction losses are estimated with (4 ± 2) W. The conduction losses for the mercury lamp are reduced considerably in comparison to the value from the powerscan without ultraviolet contributions. The calculated absorption decreases by a similar amount. These reductions improve the consistency of the energy balance.

The new powerscan for the indium iodide lamp is shown in figure 6.5.2. The proportionality constant α is given by 0.50 and the conduction losses are estimated with (7 ± 2) W. The energy balance of the indium iodide lamp is improved since both the absorption and the non-radiative losses are reduced with the new parameters. The parameter P_{Diff} therefore has a value closer to zero.

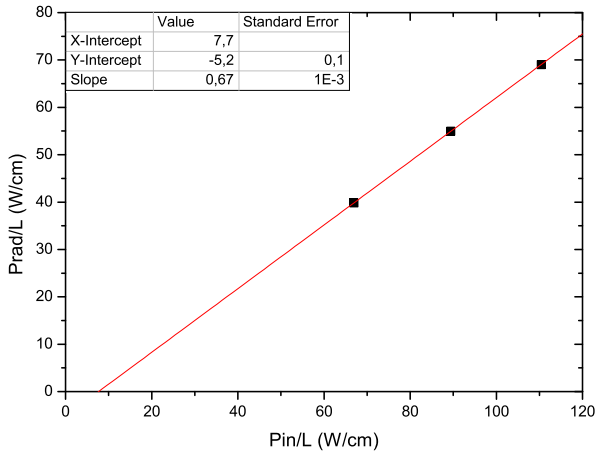

Figure 6.5.1: *The powerscan with ultraviolet contributions for the mercury lamp. The proportionality constant α is equal to* 0.67 *and the conduction losses are* (4 ± 2) *W.*

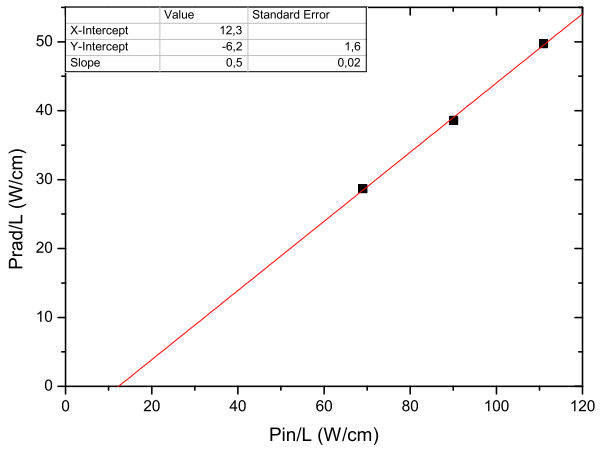

Figure 6.5.2: *The powerscan with ultraviolet contributions for the indium iodide lamp. The proportionality constant α is given by* 0.50 *and the conduction losses are estimated with* (7 ± 2) *W.*

The new energy balance for these lamps is more self consistent. It is shown in table 6.5.3. The differences between the old and the new energy balance for the mercury and indium iodide lamp are shown in table 6.5.2. For mercury the sum of the non-radiative losses and the amount of absorbed radiation decreases. For indium the non-radiative losses also decrease. The amount of absorbed radiation increases. For both lamps the result of including the ultraviolet term brings the P_{Diff} term closer to zero.

	Hg	Hg corrected	Hg+InI	Hg+InI corrected
$P_{non,rad}$ (W)	9.5 ± 2	4.4 ± 2	9.3 ± 2	7.1 ± 2
$P_{rad}(r_0)_1$ (W)	53.9 ± 2	59.0 ± 2	54.5 ± 2	56.7 ± 2
$P_{rad}(r_0)_2$ (W)	58.4 ± 4	59.2 ± 4	53.5 ± 5.6	55.8 ± 6.9
α	0.53	0.67	0.42	0.50
P_{abs} (W)	25.5 ± 2	19.4 ± 2	24.9 ± 2	28.2 ± 2
P_{Diff} (W)	11.3 ± 6.9	0.1 ± 6.9	-5.2 ± 6.8	-0.7 ± 7.0

Table 6.5.2: *The differences in the energy balance if the ultraviolet is included in the powerscan for the mercury and the indium iodide lamp. The most significant differences are the reduced absorption losses for both lamps.*

	Hg	Hg+InI	Hg+NaI	Hg+TlI
P_{in} (W)	70.5 ± 0.1	70.9 ± 0.1	71.2 ± 0.1	70.1 ± 0.1
P_{el} (W)	7.1	7.1	7.1	7.0
P_{dis} (W)	63.4	63.8	65.2	63.1
$P_{non,rad}$ (W)	4.4 ± 2	7.1 ± 2	10.0 ± 2	13.0 ± 2
$P_{rad}(r_0)_1$ (W)	59.0 ± 2	56.7 ± 2	54.1 ± 2	50.1 ± 2
$P_{rad}(r_0)_2$ (W)	59.2 ± 4	55.8 ± 6.9	54.1 ± 6	50.0 ± 5.6
α	0.67	0.50	0.84	0.83
P_{abs} (W)	19.4 ± 2	28.2 ± 2	8.8 ± 2	8.1 ± 2
$P_{dis,UV}$ (W)	9.0 ± 4	5.6 ± 4	-	-
$P_{dis,vis}$ (W)	13.8 ± 0.6	9.5 ± 0.4	22.7 ± 0.9	13.7 ± 0.6
$P_{dis,IR}$ (W)	17.0 ± 4	12.9 ± 6.5	22.6 ± 5	28.2 ± 5
P_{IR} (W)	43.2 ± 2.3	50.5 ± 2.5	45.3 ± 2.7	53.9 ± 3.0
P_{the} (W)	26.2 ± 2	37.6 ± 4	22.7 ± 2	25.7 ± 2
$P_{far,IR}$ (W)	0.7 ± 0.1	0.7 ± 0.1	0.7 ± 0.1	0.7 ± 0.1
$P_{cond,wires}$ (W)	3.9 ± 0.8	4.6 ± 0.9	3.7 ± 0.7	3.7 ± 0.7
P_{Diff} (W)	0.1 ± 6.9	-0.7 ± 7.0	-1.2 ± 5.7	-2.0 ± 6.8
P_{tot} (W)	62 ± 4	65 ± 4	73 ± 5	72 ± 4

Table 6.5.3: *The corrected energy balance for the mercury and the indium iodide lamp. The difference term P_{Diff} is now equal to zero within experimental error indicating that the energy balance is internally consistent.*

The non-radiative losses are caused by thermal conduction and reactive conduction. The reactive conduction in the hot centre is mainly caused by ionization reactions. Sodium has the lowest ionization potential, 5.14 eV, and therefore is expected to have the largest reactive contribution. Indium, 5.79 eV, has a lower ionization potential than thallium, 6.11 eV. The reactive contribution from thallium however is much stronger because the amount of thallium in the discharge is much higher than the amount of sodium and indium.

The absorption in the outer mantle is very high for the indium iodide and the mercury lamp. This contribution is large because a large portion of the emitted ultraviolet is absorbed in the outer mantle. The absorption in the indium iodide lamp is larger than in the mercury lamp because the indium lamp suffered from wall blackening. The wall blackening reduces the transmission of the discharge vessel. This disturbs the results of the powerscan. The absorption in the sodium lamp is low because sodium has no strong ultraviolet radiation. Most of its absorbed radiation will be from the sodium D-lines. The absorption in the thallium lamp is caused by thallium ultraviolet absorption and absorption of the 535 nm line. Thallium is able to radiate 378 nm radiation from the same excited state that is responsible for the 535 nm line. The low temperature in the thallium lamp means that most of the ultraviolet radiation is absorbed.

The predicted amount of absorbed radiation and non-radiatively transported energy obtained

	P_{ed}(W)	$= 0.10 \cdot P_{in}$	P_{ed}(W)	= constant
	P_{abs}(W)	$P_{non,rad}$(W)	P_{abs}(W)	$P_{non,rad}$(W)
Hg	13.0	10.6	19.4	4.4
Hg+NaI	1.0	17.5	8.8	9.9
Hg+InI	20.6	14.0	28.2	7.1
Hg+TlI	4.2	16.9	8.1	13.0

Table 6.5.4: *The results of the powerscan for two conditions: Electrode losses which are proportional to the input power and constant electrode losses. When electrode losses which are used which are dependent on the input power the absorbed radiation decreases and the non-radiative losses increase.*

from Jack Koedam theory is dependent on the assumptions made for the electrode losses. Therefore a comparison is made between two cases. In the first case the electrode losses are set to 10 % of the input power. In the second case the electrode losses are set to a constant value which is independent of the input power. As shown in table 6.5.4 this assumption does not influence the sum of the absorbed and non-radiatively transported energy but how the energy is distributed among these two terms. By assuming electrode losses which are dependent on the input power the estimated non-radiatively transported energy is significantly increased and the predicted amount of absorbed radiation is considerably decreased. The electrode losses are a weak function of the input power. The predictions made with constant electrode losses are therefore believed to be most accurate. More research on the electrode losses is required to make more accurate predictions.

For an implementation in a real lamp the dosage of the indium iodide and the thallium iodide should be adjusted since both lamps do not emit significantly more visible radiation than the pure mercury lamp. For thallium iodide this means the dosage should be reduced to decrease the strong photo dissociation continuum in the infrared. The indium dosage should be increased to obtain more radiation from the 451 nm line. At a higher buffer pressure the broadening of this line can produce better color rendering in this spectral range.

Chapter 7

Comparison

In this chapter a comparison is made between the simulations and the experiments for the four single salt lamps. For each lamp the energy balance and the spectra are compared. It is important to note that the mercury simulation was calibrated for the visible and the infrared radiation. The ultraviolet radiation dominates the mercury radiation and has a significant impact on the energy balance. The sodium iodide simulation was only calibrated for the self reversal width of the sodium D-lines. The thallium iodide and indium iodide simulations are not calibrated at all.

7.1 Hg

The simulated and measured integrated spectra for the pure mercury 70 W lamp are shown in figure 7.1.1. The broadening constants were tuned to make sure that the energy in the visible mercury transitions of the Hg 250 W lamp matched with the measured energy in these lines. The available spectrum of the 250 W lamp was made at a low resolution. As a consequence the exact shape of the mercury lines could not be captured for the calibration of the model. The resemblance of the simulated mercury lines with the measured lines at a completely different pressure is still good. The resonance broadening constant of the 404, 436 and 546 nm lines appears to be slightly underestimated at this pressure. The van der Waals broadening constant for all of these lines is strongly underestimated. The 577 and 579 nm lines are not self reversed which means that the energy difference between the measured and simulated lines is a measure of the accuracy of the predicted temperature profile and estimated pressure. This agreement is quite good since the measured energy is 1.6 W and the simulated energy is 1.63 W. The luminous efficacy of the simulation is 48 lumens/W. In the measurement a luminous efficacy of 56 lumens/W is obtained. The difference is related to the underestimated pressure broadening of the 404, 436 and 546 nm lines.

The energy balance for the simulated and measured mercury lamp is shown in table 7.1.1. The predicted 23 W ultraviolet radiation differs significantly from the estimated 9 W from the measurement. These differences are caused by the very strong broadening of the resonant mercury lines in the model. In reality these lines will not be as broad as in the simulation. In the future it is interesting to determine the exact shape of these lines from ultraviolet measurements. Better broadening constants can than be determined to improve the mercury simulation.

The predicted 10.5 W radiated visible energy is lower in comparison with the measured 13.8 W of energy because the pressure broadening of the visible lines was underestimated. The predicted 15.4 W infrared radiation is in agreement with the measurement which resulted in 17±4 W. Most of this radiation is emitted as Bremsstrahlung. The only included infrared transition is the 1014 nm line which contains only 0.8 W. Measurements indicate that the energy of the remaining mercury lines is in the order of the energy in the 1014 nm line. Not including the other infrared lines causes the infrared radiation to be underestimated by approximately one Watt.

The conduction losses are underestimated by approximately 9 W. The cumulative energy trans-

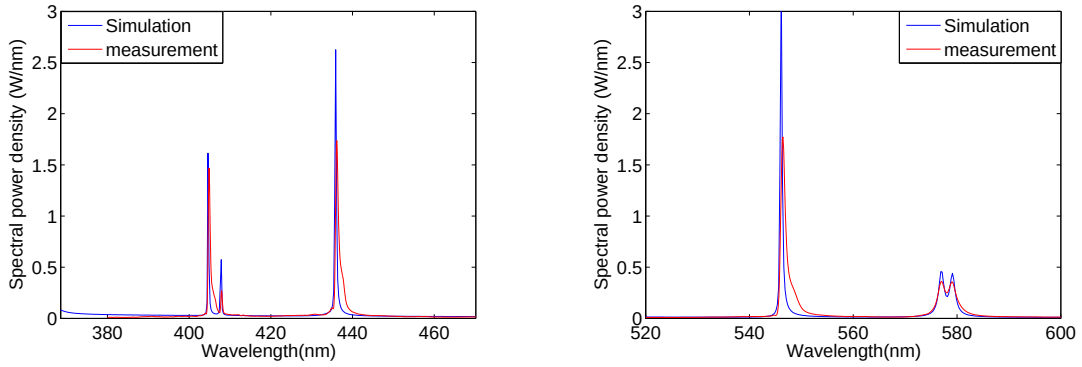

Figure 7.1.1: *a) The measured and simulated 404 and 436 nm lines. Both simulated lines have a smaller FWHM than the measured lines. The van der Waals broadening of these lines is also underestimated. b) The measured and simulated 546, 577 and 579 nm lines. The FWHM of all lines is slightly underestimated. The van der Waals broadening of the 546 nm line is strongly underestimated.*

ported directly as thermal conduction is correct within experimental error. The absorption of radiation however is strongly underestimated. Decreasing the broadening constants of the resonant mercury lines will increase the amount of radiation which is emitted close to the line centre. This will increase the optical depth and thus the absorption of radiation. The additional energy absorbed in the centre will flatten the temperature profile. This will decrease the thermal conduction losses at r_0. A better understanding of the electrode losses as a function of input power will also have an impact on the results from the powerscan.

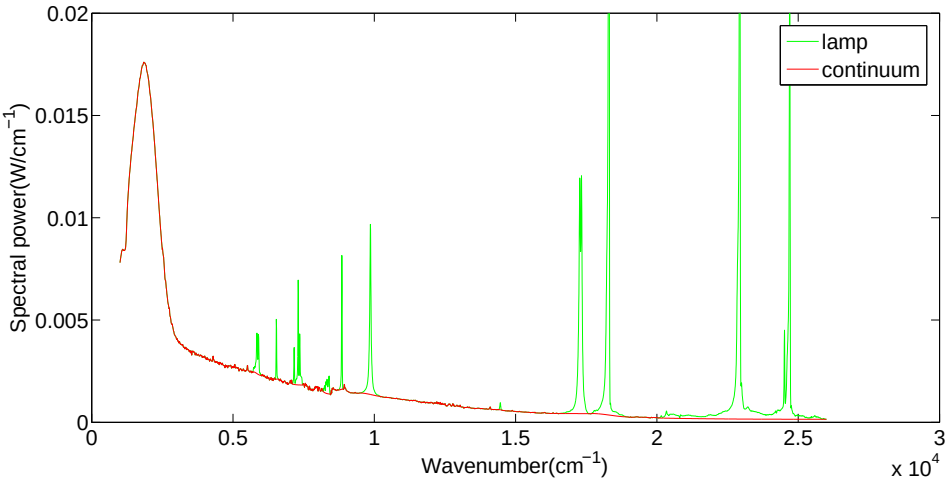

Figure 7.1.2: *The continuum radiation for the pure mercury lamp. The energy in the continuum is estimated with* 46 *W. The remaining* 11 *W is line radiation.*

	simulation (W)	measurement (W)
P_{UV}	22.8	9±4
P_{vis}	10.5	13.8±0.6
P_{IR}	15.4	17±4
$P_{non,rad}$ (r_0)	6.3	4.4±2
P_{abs}	6.6	19.4±2
P_{cond}(R)	14.4	23.8±4

Table 7.1.1: *The measured and simulated energy balances for the mercury 70 W lamp. The discrepancies between the simulation and the measurement mainly occur in the ultraviolet and the total conduction losses.*

7.2 Hg+NaI

The simulated and measured integrated spectra for the sodium iodide 70 W lamp are shown in figure 7.2.1. The broadening constants for the sodium D-lines were adjusted to match with the self reversal width of a not perfectly calibrated 70 W SON lamp. More accurate constants can be obtained with a correct calibrated spectrum. An analysis of the sodium D-lines shows that the simulated left wing is much broader than the measured left wing. The product of the resonance broadening constant and the sodium density is thus overestimated. The right wing shows several peaks between 640 and 700 nm. These peaks are satellite peaks. They occur when the interaction potential curves of the excited and ground state have the same derivative with respect to the distance to the perturbing particle. These peaks can be included by considering the energy levels of the Na+Hg quasi molecule [45]. Such a calculation is considered out of the scope of this work. A further analysis of the spectrum shows that the radiation of the 577 and 579 nm lines of mercury is not visible in the simulated spectrum. This is related to the high sodium pressure which significantly reduces the temperature profile and thus the radiation from the mercury lines. The radiation from the 818 and 819 nm lines shows that the resonance and the van der Waals broadening constants are underestimated for the second most important sodium lines. The measured luminous efficacy is 90 lumens/W. The simulated efficacy is 122 lumens/W. The largest contribution of the overestimated efficacy is caused by the overestimated left wing of the sodium D-lines.

The energy balance for the simulated and the measured sodium iodide lamp is shown in table 7.2.1. The predictions of the radiated energy are close to the measured values. The overestimated 2 W of visible radiation is caused by the sodium D-lines. The energy in the simulation of the sodium D-lines amounts to 22.7 W which is almost the entire visible contribution. The measured 13.9 W of radiation from these lines is significantly lower. The difference can be reduced by improving the calibration of the SON 70 W lamp. The predicted infrared energy is a few Watt above the measured energy. The infrared sodium lines are all underestimated in comparison with the measured lines. The infrared Bremsstrahlung is therefore overestimated.

The conduction losses are significantly underestimated. This could be expected since this was also the case for the SON lamps. The axis temperature is currently too low because the sodium density is overestimated. Decreasing the sodium density will increase the axis temperature. As a result the non-radiative losses and the absorption will increase. An increase in the simulated non radiative losses can be obtained by including the reactive conductivity in the model for the sodium iodide system. The resulting increase in conduction losses will be small because the mercury pressure is high. The diffusion coefficients will thus be small. This limits the transport of chemical energy.

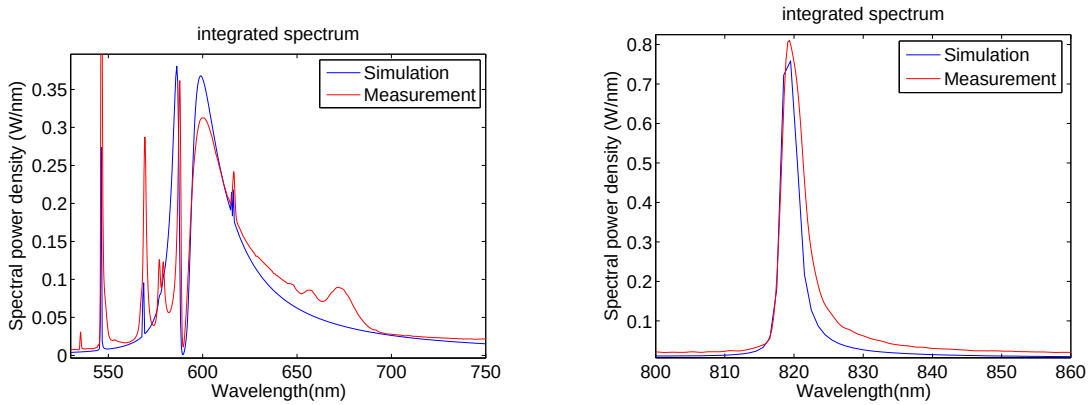

(a) **(b)**

Figure 7.2.1: *a) The measured and simulated sodium D-lines. The broadening of the left wing of the sodium D-lines indicates that the sodium pressure is too high in the simulation. The right wing is not in agreement with the experiment since the quasistatic van der Waals broadening can not account for satellite peaks. b) The measured and simulated 818 and 819 nm lines are shown. Both the resonance and van der Waals broadening parameters are underestimated in this simulation.*

	simulation (W)	measurement (W)
P_{UV}	2.2	-
P_{vis}	24.7	22.7±0.9
P_{IR}	26.6	22.6±5
$P_{non,rad}$ (r_0)	4.2	10.0±2
P_{abs}	5.0	8.8±2
P_{cond}(R)	9.6	18.8±4

Table 7.2.1: *The simulated and measured energy balances for the sodium iodide 70 W lamp. The discrepancies are mainly caused by the conduction losses.*

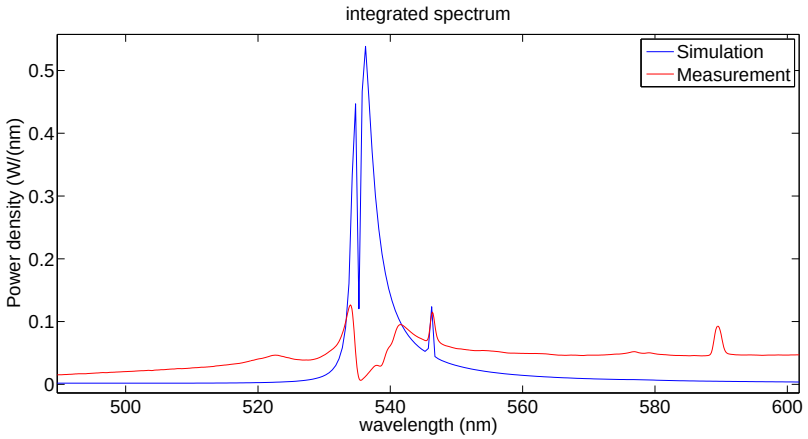

Figure 7.3.1: *The simulated 535 nm line. A parabolic temperature profile is used with an axis temperature of 4600 K and a coldspot temperature of 900 K. When the photo dissociation continuum is included as well the optical depth and thus the self reversal width of the 535 nm thallium line will increase.*

7.3 Hg+TlI

The simulated and measured spectra for the thallium iodide discharge are not in agreement because the strong photo dissociation continuum radiation is not included in the model. A comparison of the predicted and measured energy balance is therefore not meaningfull. Instead the simulated 535 nm line is matched with the measured line by using a parabolic temperature profile, normal dosages and theoretical broadening constants to obtain an estimate of the axis temperature. The coldspot required to obtain a reasonable spectrum is 900 K. This value is very low which is an indication that the error in the dosage may be very large. The spectrum is shown in figure 7.3.1. Fitting the thallium line is difficult since there is a large uncertainty in the thallium and mercury densities and in the temperature profile. The 546 nm mercury line is used to estimate the axis temperature. The mercury pressure was estimated to be 15 bar. An error of the mercury pressure thus results in an error of the axis temperature. At an axis temperature of 4600 K the thallium density is 16 kPa. When the photo dissociation continuum is also included the optical depth of the line centre of the thallium line will increase further. As a consequence the self reversal width will increase. In the line centre it is unknown what radiation is emitted as line radiation and what radiation is emitted as continuum radiation. As a result a more accurate estimate of the temperature profile can not be made.

7.4 Hg+InI

The simulated and measured spectra for the indium iodide 70 W lamp are shown in figure 7.4.1. The obtain a better agreement with the experiment the indium dosage was reduced considerably in comparison to the specifications. Most likely only a small amount of the specified indium dosage was put in the lamp. Since the energy in the mercury lines is overestimated the axis temperature should be lower. The axis temperature can be reduced by increasing the indium dosage. However the energy in the indium lines is also overestimated which is an indication that the indium density is still too high. Including the reactive conductivity in the simulation will reduce the axis temperature. At a mercury pressure of 30 bar this contribution will be small. Measuring a lamp with an unsaturated amount of indium iodide will avoid the problems encountered with the coldspot. When the dosage is known accurately the indium pressure can be calculated similarly to the mercury pressure.

The simulated and measured energy balances are shown in table 7.4.1. The ultraviolet losses

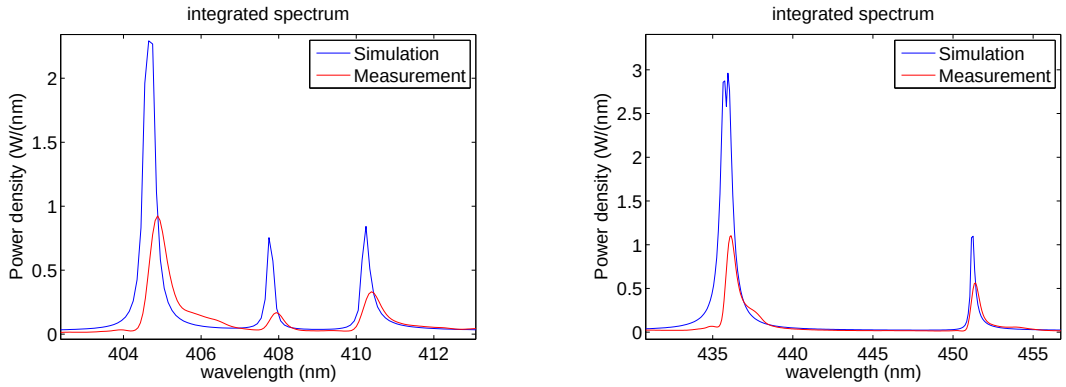

(a) (b)

Figure 7.4.1: *a) The 410 nm indium line. The radiative output of the mercury 404 and 407 nm lines and the indium 410 nm line are overestimated. b) The 451 nm indium line. The radiative output of the indium 451 nm line and the mercury 436 nm line are overestimated.*

	simulation (W)	measurement (W)
P_{UV}	20.3	5.6±4
P_{vis}	14.7	9.5±0.4
P_{IR}	13.7	13.9±6.5
$P_{non,rad}$ (r_0)	5.8	7.1±2
P_{abs}	6.7	28.2±2
P_{cond}(R)	14.3	35.3±4

Table 7.4.1: *The measured and simulated energy balances for the indium iodide 70 W lamp. The largest discrepancies are the conduction losses and the ultraviolet losses.*

are overestimated by approximately 15 W. This is related to the overestimated axis temperature and the uncertainty in the broadening constants of the resonant mercury lines. The high axis temperature is also the reason why the visible radiation is overestimated. The conduction losses at the wall are strongly underestimated. The conduction losses at r_0 are equal within experimental error. The conduction losses at r_0 in the simulation will be increased when the reactive conductivity is included. This increase will be small since the chemical transport is limited at high mercury pressures. The amount of absorbed radiation determined from the measurements is overestimated due to wall blackening. Another reason for these differences are the incorrect broadening constants of the resonant mercury lines in the simulation. More accurate estimates of the non-radiative losses and the absorbed radiation can be made when the exact electrode losses are known.

7.5 Conclusion

A comparison between the simulated and experimentally determined spectra and energy balances is made. Due to the strong photo dissociation continuum of the thallium iodide which is not included in the model a comparison for this lamp is not possible.

The predicted spectrum of the pure mercury lamp shows underestimated van der Waals broadening of the visible lines. The energy emitted as visible radiation is therefore slightly underestimated. The simulations also show strong broadening of the red wing of the resonant lines. As a consequence the energy emitted as ultraviolet radiation is overestimated. The ultraviolet energy is overestimated by roughly the same amount as the absorption of radiation is underestimated. Decreasing the broadening constants of the resonant mercury lines reduces the ultraviolet output

and will increase the amount of radiation which is absorbed in the outer mantle. The temperature will increase when more radiation is absorbed and thus also the visible output will be closer to the measured output.

The sodium iodide simulation shows good agreement between the predicted and measured infrared and visible radiation. A more detailed analysis of the spectrum shows that the predicted energy in the lines differs from the measured energy. This difference is largest for the sodium D-lines were 13.9 W was measured and 22.7 W was predicted. The predicted self reversal maxima are not in agreement with the measured self reversal maxima. From their positions can be concluded that the amount of sodium is overestimated and that the amount of mercury is underestimated. This is related to the unknown coldspot temperature. Another important factor are the not calibrated broadening constants for the sodium lines. The agreement of the predicted and measured energy in the sodium D-lines already differed for the sodium calibration lamp. Improving this calibration will also improve the sodium iodide simulation. The underestimated absorption in the outer mantle is related to the calibration of the broadening constants. The underestimated non radiative losses can be increased by including the reactive conductivity.

The indium iodide simulation is similar to the pure mercury simulation due to the low indium iodide content in the lamp. The simulated energy balance is therefore roughly equal to the simulated energy balance of the mercury lamp. In the simulation more visible radiation is obtained for the indium iodide lamp. This difference is not caused by the indium lines but by the more efficient mercury lines. Due to the slighly lower temperature the mercury density is higher which means the mercury lines are broader in the indium lamp. As a consequence the optical depth decreases and the visible efficiency increases. This is not observed in the measurement. The measured radiated energy in the indium lamp is lower than for the mercury lamp. This is caused by the strong wall blackening of the indium iodide lamp. It is impossible to determine what amount of radiation is absorbed in the outer mantle and what amount is absorbed on the wall.

Chapter 8

Conclusion

In this work the energy balance of HID lamps was studied both experimentally and theoretically. Part of the experimental work was the calibration of an integrating sphere setup. By using switch-off measurements and powerscans a more detailed energy balance could be determined. The theoretical work involved the construction of a lamp model which is capable of calculating the radiatively transported energy through the plasma. This lamp model has been made. In the future this lamp model will be calibrated more elaborately.

8.1 Experimental work

An integrating sphere setup was calibrated from 380 nm till 10 μm. This setup is operated in vacuum conditions to minimize heat losses and oxidation from the discharge vessel. Absorption of radiation is also decreased. The infrared part of the spectrum was calibrated with a platinum ribbon. The spectral power of this ribbon was calculated theoretically from a one dimensional model. The resistivity, thermal conductivity, effective emissivity and the spectral emissivity of platinum as a function of temperature were obtained from literature. The visible part of the spectrum was calibrated with a halogen lamp. The halogen lamp was calibrated at Philips OCM laboratories.

The accuracy of the infrared calibration depends on the temperature stability of the setup and the detectors. A temperature regulation system was added to the integrating sphere to make sure that its temperature could be kept constant within ± 0.1 K. The Fourier transform spectrometer was surrounded with a box made of insulation material. The air inside this box is kept at a constant temperature by a heating system to improve the temperature stability of the spectrometer.

A measurement scheme was developed for lamp calibrations. By using this scheme an energy balance can be determined based on measurements of the entire visible and infrared up to 10 μm with an accuracy of roughly 5 %. Apart from a constant error which is present over the entire spectral range there are four spectral parts which are currently measured at a lower accuracy. The most important part is the spectral interval where a background correction is required for thermal radiation of the integrating sphere. The temperature stability of the integrating sphere and the DLaTGS detector determine the errors in this spectral interval. The errors in the remaining three intervals are caused by a lower signal to noise ratio of the detector used in that particular spectral interval. The overlap of the useful measurement range which can be covered by the available three detectors and two beamsplitters is not perfect. However these three spectral intervals are relatively small which limits the contribution to the total measurement error.

The thermal radiation was separated from the discharge radiation by using switch-off measurements. The switch-off measurements were not calibrated. As a consequence the ratio of the switch-off measurements to a reference measurement was applied to a calibrated spectrum to obtain the thermal radiation. This extra step may result in small additional errors.

To obtain more insight in the energy flows inside the burner, the Jack Koedam theory was

applied. The Jack Koedam plots provide an estimate of the energy which is absorbed in the outer mantle and the conduction losses at the position where the radiation losses reach a maximum. A drawback of this method is that the energy dissipated in the electrodes should be known. A different assumption for these losses thus changes the predicted internal energy flows.

8.2 Lamp modeling

A model for an infinitely long lamp was made. Local thermodynamic equilibrium was assumed. The mercury pressure is much larger than the pressure of the other species for the investigated lamps. The thermal and electrical conductivities of mercury were therefore used to describe the dissipation and the transport of energy. The transport of chemical energy is currently available for systems without iodine species. The transport of radiative energy is calculated with a method called raytracing.

The models give a good qualitative description of a lamp which is dominated by atomic radiation. In the future a more quantitative description will be possible when a more elaborate comparison can be made with a complete spectrum. Most lamp models suffer from the uncertainty in the broadening constants of the resonant mercury lines. The ultraviolet part of the spectrum of the mercury lamp intented for calibrating the mercury model could not be measured. Therefore the broadening constants had to be estimated. The broadening constants of these resonant lines were chosen to obtain the correct energy in an optically thin visible transition. For a given pressure the energy in thin lines is only dependent on the temperature. The shape of the resonant lines was adjusted since they have a strong influence on the temperature profile. The shape of the 254 nm line was also matched with a shape described in literature for the same lamp. As a consequence the predictions of the radiative output of these resonant lines provides accurate results for mercury pressures close to the pressure of the calibration lamp. Predictions of the visible energy of the mercury 250 W calibration lamp at input powers ranging from 190 W to 310 W were in agreement with the experiment. The predicted radiative output of the resonant lines is overestimated at mercury pressures which are significantly above the pressure of the calibration lamp.

The sodium iodide model was calibrated with a SON 70 W lamp which is a high pressure sodium lamp. The broadening constants of the sodium D-lines were calibrated to obtain the same self reversal width as in the experiment. For the SON 400 W lamp the self reversal width was correctly predicted with the same broadening constants. Considering that the sodium and mercury pressures are difficult to estimate in the sodium iodide lamp the predictions of the self reversal width for this lamp were in reasonable agreement. For the indium iodide and the thallium iodide lamp models no calibration lamp is available. Calibrating these models with the spectra of the single salt lamps is difficult because the coldspot temperature and the exact salt dosage is unknown. As a consequence the density profiles can not be calculated accurately. Since the pressure broadening mechanisms are dependent on these densities an accurate broadening constant can not be determined.

The predicted and measured energy in the visible and infrared part of the spectrum are in reasonable agreement. The predictions and the estimated ultraviolet energy showed larger deviations. These deviations are related to the lack of knowledge of the shape of the resonant mercury lines. The conduction losses also showed larger deviations. This can partly be explained by the underestimated absorption of radiation due to the uncertainty in the resonant mercury lines. The thermal conductivity is currently also slightly underestimated by not including the reactive conductivity for the single salt lamps. Adding the reactive conductivity for the single salt lamps will have a small impact on the predicted thermal conductivity since the transport of chemical energy is limited due to the high mercury pressure.

8.3 Outlook and recommendations

In the future the temperature stability of the DLaTGS detector will be improved by adding a cooling system for this detector. The detector will also be mounted in a separate measurement slot for the FTIR. Currently only two of these measurement slots are available for the three detectors. Obtaining a third slot with a temperature stability system will increase the number of measurements which can be made.

Currently calibrated measurements can be made from 380 nm till 10 μm. In the future part of the ultraviolet will also be calibrated. Being able to measure the ultraviolet will improve the results for the mercury model since the resonant lines can be calibrated. The measurement range of the new detector also coincides with one of the three spectral intervals which currently suffer from a reduced signal to noise ratio.

The infrared part of the spectrum is calibrated with a calculated spectral power of a platinum ribbon. The spectral power depends on literature values of the resistivity, thermal conductivity and emissivity. Especially the spectral and effective emissivity are dependent on local conditions like surface roughness and can therefore deviate from literature values.

The thermal radiation is currently calculated by multiplying a calibrated spectrum with the ratio of the switch-off measurements to a reference measurement made with the lamp still on. By directly calibrating the setup with the settings used for the switch-off measurements the errors which are introduced with the additional conversion are removed.

The results of the Jack Koedam analysis are dependent on the assumptions of the electrode losses. These assumptions change the predicted distribution of energy between the absorbed radiation in the outer mantle and the conduction losses from the centre to the outer mantle. A theoretical calculation of the electrode losses will be possible with the electrode model Eldes.

The lamp models should be extended with a calculation of molecular radiation. This extension requires accurate interaction potential curves of the molecular energy states as a function of the internuclear distance. The transition probabilities for these states should also be available. Including the reactive conductivity for the systems containing metal halides is another improvement.

Making an accurate estimate of the temperature and density profiles in the lamps is difficult. A good calibration of the broadening constants depends on the accuracy of these profiles. Therefore an experimental setup which is capable of determining these profiles is required.

Acknowledgements

This thesis completes the graduation project of the Master of Applied Physics at the TU/e. This is the first project for a physicist that comes with more freedom to choose an own research path. When I was looking for a project I wanted to have a good mix of experimental and modeling work. I soon realized that this project offered me this opportunity. My project was supervised by Arij. I think you did this in the best possible way. I really appreciate how you immediately made me a part of this project by including my input in important decisions. I also liked that you always encouraged me to search for an explanation when we encountered an unknown phenomenon. I would also like to thank my other supervisors, Sander and Marco, for the encouraging atmosphere and their useful advice. Most important of all: I had a great time working with the three of you!

Besides my direct supervisors I also received help from many others. From the EPG group these are Gerrit and Jan for providing additional advice and Huib, Ab and Loek for help on the setup. From Philips I would like to thank Jos and Maxime for the interesting discussions and useful advice which lead to new insights. Finally I would like to thank all members of the EPG group for providing a great atmosphere to work in.

Appendix A

Experimental work

In this chapter additional results obtained in experiments are shown. This result is a plot of the powerscans for all lamps in the same figure.

A.1 Powerscans: All lamps

The UV corrected powerscans for all lamps are shown in figure A.1.1. For high input powers per unit length the lamps with the highest transmission of the outer mantle provide the largest amount of visible radiation. At low input powers the relative contribution of the conduction losses is increasing. For very low input powers the assumption that the conduction losses are independent of the input power is no longer valid. All powerscans assume that the electrode losses are 10 % of the nominal input power.

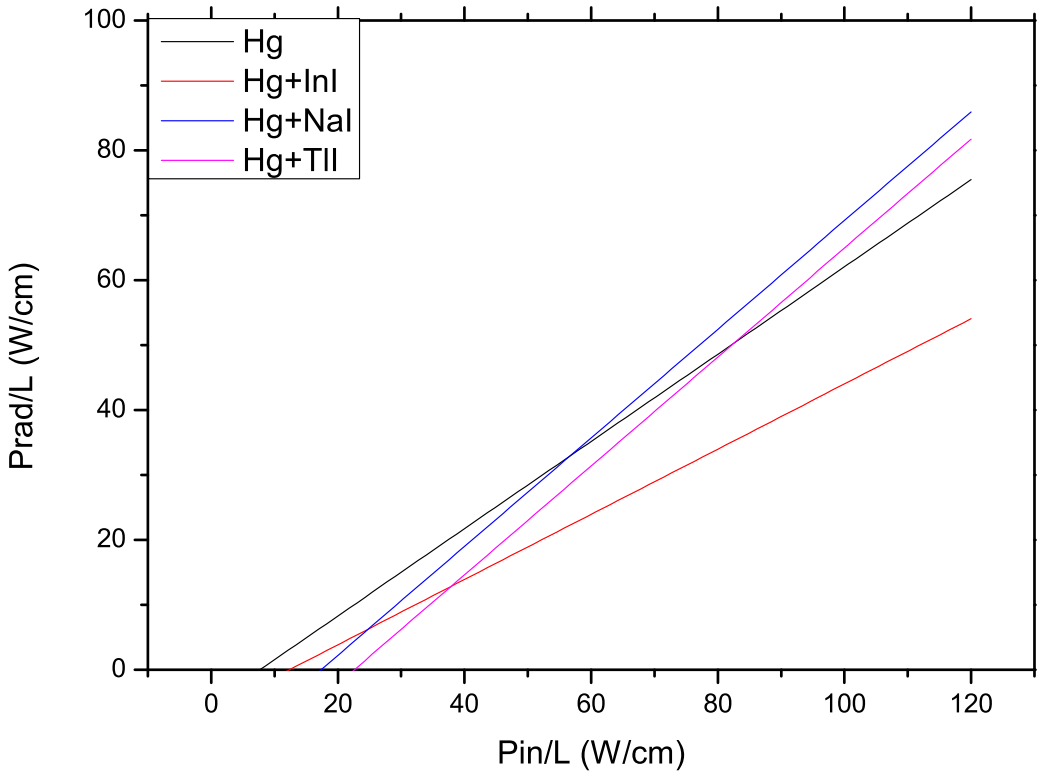

Figure A.1.1: *The results of the powerscans for all single salt lamps. The results show the conduction losses per unit length on the Pin/L-intercept. The slope of the curves indicates the transmission of the outer mantle.*

Bibliography

[1] M.Gendre, Two centuries of electric light source innovations. Available online: http://www.einlightred.tue.nl/lightsources/history/light_history.pdf

[2] Wharmby D O, Energy balance of high-pressure sodium discharges under controlled vapour conditions. 1984, J. Phys. D: Appl. Phys. 17 p 367-78.

[3] Gough A, Sansonetti C, Curry J, and Lawler J, 2006, Program on Technology Innovation: Advanced Light Source Research: ALITE-II: Losses in High Intensity Discharge Light Sources 1012994. (Palo Alto, CA: EPRI, Somerset, NJ: Philips Lighting Company, Niskayuna, NY: General Electric Company, Beverly, MA: Osram Sylvania)

[4] Smith D J, Bonvallet G A and Lawler J E, Infrared losses from a Na/Sc metal-halide high intensity discharge arc lamp. 2003, J. Phys. D: Appl. Phys. 36 p 1519–28

[5] A.J. Rijke, S. Nijdam, M. Haverlag, J.F.J. Janssen, J.J.A.M. van der Mullen and G.M.W. Kroesen, A calibrated integrating sphere setup to determine the infrared spectral radiant flux of high intensity discharge lamps. 2011, J. Phys. D: Appl. Phys. 44 224007

[6] Elenbaas W., The High Pressure Mercury Vapour Dis charge, North-Holland Publishing Co., Amsterdam, 1951,

[7] Jack A. G. and Koedam M, Energy balances for some high gas pressure discharge lamps. 1974, J. Illum. Eng. Soc. 3

[8] M.L. Beks, Modelling Additive Transport in Metal Halide Lamps. PhD thesis, 2008

[9] H.W.P van der Heijden, Modelling of Radiative Transfer in Light Sources. PhD thesis, 2003

[10] A. Sobota, Breakdown processes in HID lamps: Exploration of various key aspects, PhD thesis, 2011

[11] J.J. de Groot, J.A.J.M van Vliet, The high pressure sodium lamp,1986,ISBN 90 201 1902 8

[12] C.W. Johnston, H.W.P. van der Heijden, G.M. Janssen, J. van Dijk and J.J.A.M. van derMullen, A self-consistent LTE model of a microwave-driven, high-pressure sulfur lamp, J. Phys. D: Appl. Phys. 35 (2002) 342–351

[13] W.L. Nighan, Electron Energy Distributions and Collision Rates in Electrically Excited N_2, CO, and CO_2

[14] J.N. Butler and R.S. Brokaw, Thermal Conductivity of Gas Mixtures in Chemical Equilibrium, J. Chem. Phys. 26, 1636 (1957)

[15] R.S. Brokaw, Thermal Conductivity of Gas Mixtures in Chemical Equilibrium. II, J. Chem. Phys. 32, 1005 (1960)

[16] C.W. Johnston, Transport and equilibrium in molecular plasmas: the sulfur lamp, Phd thesis 2003

[17] D.R. Bates, Advances in atomic and molecular physics, volume 5, Academic Press Inc, 1969

[18] J.-H. Tortai, N. Bonifaci, A. Denat and C. Trassy, Diagnostic of the self-healing of metallized polypropylene film by modeling of the broadening emission lines of aluminum emitted by plasma discharge, J. Appl. Phys. 97, 053304, 2005

[19] I. I. Sobelman, Über die Theorie der Linienbreite von Atomen, Fortschritte der Physik volume 5, 175 - 210, 1957

[20] M. Born, Line broadening measurements and determination of the contribution of radiation diffusion to thermal conductivity in a high-pressure zinc discharge, 1999 J. Phys. D: Appl. Phys. 32 2492

[21] Chien Yu-Min, On the shifts of self-reversed maxima of the sodium resonance radiation, J. Appl. Phys. 51(6), 1980

[22] H.P. Stormberg, Line broadening and radiative transport in high-pressure mercury discharges with NaI and TlI as additives, J. Appl. Phys. 51 (4), 1980

[23] E. Fischer, Axial segregation of additives in mercury–metalhalide arcs, J. Appl. Phys. 47, 2954 (1976)

[24] M. Haverlag, internal communications

[25] C.O. Laux, T.G. Spence, C.H. Kruger and R.N. Zare, Optical diagnostics of atmospheric pressure air plasmas, Plasma Sources Sci. Technol. 12 (2003) 125–138

[26] H.R. Griem, Plasma Spectroscopy, McGraw-Hill Book company, 1964

[27] The Plasimo team (part of the EPG group at TU/e), Computational plasma physics, version 2009/2010

[28] R.A. Svehla, Estimated viscosities and thermal conductivities of gases at high temperatures, NASA TR R-132

[29] P. Rini, D. vd Abeele and G. Dégrez, Closed form for the equations of chemically reacting flows under local thermodynamic equilibrium, PHYSICAL REVIEW E 72, 011204 2005

[30] S.H. Patil, Thomas–Fermi model electron density with correct boundary conditions: applications to atoms and ions, Atomic Data and Nuclear Data Tables 71, 41–68 (1999)

[31] Buckman, S. J., Elford, M. T.: Momentum transfer cross sections. Itikawa, Y. (ed.). SpringerMaterials - The Landolt-Börnstein Database DOI: 10.1007/10547143_3

[32] M. Mitchner and C. H. Kruger, Partially Ionized Gases. (New York: Wiley & Sons), 1973.

[33] Labsphere producer of commercial integrating spheres, A guide to integrating sphere theory and applications, http://www.labsphere.com/technical/technical-guides.aspx

[34] R.S. Bergman and Y. Ohno, The art and science of lamp photometry, Procedings of the 9th International Symposium on the Science and Technology of Light Sources p 165-79, 2001

[35] Y.S. Touloukian and D.P. DeWitt , 1970, 'Thermophysical properties of matter part 7: Thermal radiative properties : metallic elements and alloys', New York: S.l. IFI/Plenum.

[36] Y.S. Touloukian, R.W. Powell and C.Y. Ho, 1970, 'Thermophysical properties of matter part 1: thermal conductivity: metallic elements and alloys' New York: S.l. IFI/Plenum.

[37] G.W.C. Kaye, T.H. Laby, 1995, 'Tables of physical and chemical constants', 16th edition, Harlow: Longman.

[38] R.E. Rolling, A.I. Funai, and J.R. Grammer, 1964, Investigation of the effect of surface condition on the radiant properties of metals. TR No. AFML-TR-64-363. Air Force Systems Command, Wright-Patterson Air Force Base, Ohio.

[39] National institute of standards and technology (NIST) Atomic spectral database, http://physics.nist.gov/PhysRefData/ASD/lines_form.html

[40] P. L. Smith, C. Heise, J. R. Esmond, R. L. Kurucz, Atomic spectral line database, university of Hannover, http://www.pmp.uni-hannover.de/cgi-bin/ssi/test/kurucz/sekur.html

[41] J. E. Lawler, Bremsstrahlung radiation from electron–atom collisions in high pressure mercury lamps, J. Phys. D: Appl. Phys. 37 (2004) 1532–1536

[42] M. Haverlag, Plasma chemistry of fluorocarbon RF discharges used for dry etching, PhD thesis, 1991

[43] H.P. Stormberg and R. Schäfer, Time dependent behavior of high pressure mercury discharges, J. Appl. Physics 54 (8) 1983.

[44] G. Hartel, H. Schöpp, H. Hess, and L. Hitzschke, Radiation from an alternating current high-pressure mercury discharge: A comparison between experiments and model calculations, J. Appl. Phys. 85, 7076 (1999)

[45] J.P. Woerdman, J. Schlejen, J. Korving, M.C. van Hemert, J.J. de Groot and R.P.M. van Hall, Analysis of satellite and undulation structure in the spectrum of Na+Hg continuum emission, J. Phys. B: At. Mol. Phys. 18 (1985) 4205-4221.

[46] S. D. Herrera, L. A. Schlie, and G. Black, Infrared (0.9–1.65 μm) emission from thallium iodide photoexcited with ultraviolet excimer laser radiation, J. Chem. Phys. 96, 1840 (1992)